Schriftenreihe des Energie-Forschungszentrums Niedersachsen

efzn
Energie-Forschungszentrum
Niedersachsen

TU Clausthal

Numerical Investigations of Reactive Transport Processes during the Storage of Hydrogen in the Porous Subsurface

Sebastian Hogeweg

Promotion an der Technischen Universität Clausthal

Band 82

Cuvillier Verlag Göttingen

TU Clausthal

Numerical Investigations of Reactive Transport Processes during the Storage of Hydrogen in the Porous Subsurface

Doctoral Thesis
- Dissertation -

to be awarded the degree
Doctor of Engineering (Dr.-Ing.)

submitted by
Sebastian Hogeweg
from Neuss, Germany

approved by the Faculty of Energy and Economic Sciences,
Clausthal University of Technology

Date of oral examination

25.03.2024

Bibliografische Information der Deutschen Nationalbibliothek
Die Deutsche Nationalbibliothek verzeichnet diese Publikation in der Deutschen Nationalbibliografie; detaillierte bibliografische Daten sind im Internet über http://dnb.dnb.de abrufbar.
1. Aufl. - Göttingen: Cuvillier, 2024
Zugl.: (TU) Clausthal, Univ., Diss., 2024

Dean: Prof. Dr. mont. Leonhard Ganzer	**Supervising tutor:** Prof. Dr. mont. Leonhard Ganzer
Chairperson of the Board of Examiners: Prof. Dr. Oliver Langefeld	**Reviewer:** apl. Prof. Dr. rer. nat. Bernd Flemisch

Nonnenstieg 8, 37075 Göttingen
Telefon: 0551-54724-0
Telefax: 0551-54724-21
www.cuvillier.de

Diese Veröffentlichung wurde aus Mitteln des Publikationsfonds Niedersachsen-OPEN, gefördert aus zukunft.niedersachsen, unterstützt.

1. Auflage, 2024
Gedruckt auf umweltfreundlichem, säurefreiem Papier aus nachhaltiger Forstwirtschaft.

doi 10.21268/20240603-0
ISBN 978-3-68952-001-4
ISBN eBook OA 978-3-68952-043-4

Abstract

With the increasing fluctuations in energy demand and supply, the motivation for energy storage systems is growing significantly. Hydrogen is considered a promising candidate to be generated with excess electrical energy, stored, and used as a versatile energy carrier and resource on demand. In particular, the large-scale storage of hydrogen in the subsurface, known as Underground Hydrogen Storage (UHS), could contribute to balance seasonal fluctuations in analogy to the current storage of natural gas. However, it is expected that hydrogen's unique properties will lead to changes in the fluid displacement processes inside geological formations, potentially impacting storage efficiency. Moreover, the mixing with the initial gas caused by molecular diffusion and mechanical dispersion is assumed to be essential and can lead to a temporary loss of hydrogen. Permanent hydrogen losses and contamination of the stored gas could be caused by chemical reactions induced by interactions with the rock matrix and the presence of hydrogenotrophic microorganisms adapted to the reservoir conditions.

To assess the potential risks, an existing mathematical model for the two-phase multi-component bio-reactive transport process during UHS was extended by a geochemical reaction model and implemented into the open-source simulator DuMu^{x}. Afterwards, the model was calibrated by recent laboratory observations regarding molecular diffusion, microbiology, and geochemistry. The calibration encompassed the development of correlations and models with the subsequent reproduction of the laboratory observations. In the final step, the calibrated model was employed on a field-scale reservoir model to predict a large-scale UHS scenario. Here, the stored hydrogen was partially converted by the reactions and the mixing with the cushion gas negatively impacted the hydrogen recovery.

The developed model in DuMu^{x} was extended to include the process of mechanical dispersion promoting the gas-gas mixing during operation. This implementation required the CVFE discretization scheme to model this process properly, and consequently, a workflow for modifying simulation meshes and a new well model were developed. The implementation was subsequently applied to predict the outcome of an ongoing field test in Germany concerning gas-gas mixing. The results showed that the mechanical dispersion promotes the mixing, resulting in a reduced hydrogen recovery.

Originating from UHS, the concept of an Underground Bio Methanation reactor was investigated, where methanogenic microorganisms are selectively utilized to convert stored hydrogen and carbon dioxide into methane and water at reservoir conditions. Numerical simulations were performed to assess the potential of a freshwater injection in high-saline formations to stimulate the metabolism of the organisms even at unfavorable living conditions. For this purpose, the microbial growth was coupled to the salt concentration. The results showed that it enables growth and consumption; however, the complete conversion was not observed.

Kurzfassung

Die zunehmenden Schwankungen der Nachfrage und der Bereitstellung von Energie, führt zu einer steigenden Motivation für die Schaffung von Energiespeichersystemen. Wasserstoff zählt als möglicher Kandidat, welcher mit überschüssiger elektrischer Energie erzeugt, anschließend gespeichert und bei Bedarf als Energieträger oder Ressource genutzt werden kann. Die Speicherung größerer Kapazitäten im Untergrund, die sogenannte Untergrundwasserstoffspeicherung, kann, ähnlich zu Erdgas, saisonale Schwankungen ausgleichen. Durch die besonderen Eigenschaften von Wasserstoff wird allerdings der Verdrängungsprozess im Speicher beeinflusst, was zu einer Reduktion der Effizienz führen kann. Zusätzlich führt das Vermischen mit dem Kissengas zu einem temporären Verlust an Wasserstoff. Permanente Verluste sind durch mögliche chemische Reaktionen, welche durch Interaktionen mit dem Gestein oder durch hydrogenotrophe Mikroorganismen hervorgerufen werden, bedingt.

Um das potenzielle Risiko zu beurteilen, wurde ein existierendes mathematisches Modell für einen zweiphasigen, multikomponenten, bioreaktiven Transportprozess um die geochemische Komponente erweitert und anschließend in den Open-Source-Simulator DuMu$^\text{x}$ implementiert. Die Implementierung wurde anschließend auf Basis von Laboruntersuchungen im Hinblick auf molekulare Diffusion, Mikrobiologie und Geochemie kalibriert. Die Kalibrierung umfasste die Entwicklung neuer Korrelationen und Modelle mit anschließender Reproduzierung der Experimente. Das kalibrierte Modell wurde für erste Simulationsstudien auf der Feldskala genutzt, um den Einfluss auf den Betrieb eines Wasserstoffuntergrundspeichers hervorzusagen. In den Simulationen konnte eine Verringerung der Speichereffizienz durch die Reaktionen und das Mischen des gespeicherten Gases mit dem initialen Gas beobachtet werden.

Das entwickelte Modell in DuMu$^\text{x}$ wurde um den Prozess der mechanischen Dispersion, welche das Mischverhalten begünstigt, erweitert. Die Implementierung setzte das CVFE Diskretisierungsschema voraus, um diesen Prozess nachzubilden. Zusätzlich wurde ein Arbeitsablauf zur Umwandlung von Simulationsnetzen und ein zugehöriges Bohrungsmodell entwickelt. Mithilfe des entwickelten Simulationsmodells wurde ein laufender Feldtest der Untergrundwasserstoffspeicherung in Deutschland im Hinblick auf das Mischverhalten des gespeicherten und initialen Gases untersucht. Die Ergbenisse der Simulationen zeigten, dass die mechanische Dispersion das Mischverhalten begünstigt und dabei die Rückförderung reduziert.

In einem weiteren Schritt wurde als Sonderfall der Untergrundwasserstoffspeicherung das Konzept der untertägigen Methanisierung untersucht, bei welchem methanogene Mikroorganismen gezielt genutzt werden, um Wasserstoff und Kohlenstoffdioxid in Methan und Wasser umzuwandeln. Numerische Simulationen wurden durchgeführt, um das Potenzial einer Süßwasserinjektion in hochsalinaren Formationen zur Stimulation des mikrobiellen Stoffwechsels, selbst bei unzureichenden Bedingungen, zu beurteilen. Hierfür wurde das mikrobielle Wachstum an die Salzkomponente gekoppelt. Die Ergebnisse zeigten, dass das Wachstum und auch die Umwandlung ermöglicht wurden, jedoch blieb die gänzliche Umsetzung des gespeicherten Gases aus.

Preface

This dissertation is the result of various research projects that were carried out as part of my work at the Institute of Subsurface Energy Systems in the reservoir engineering department under the guidance of Prof. Dr. mont. Leonhard Ganzer. My sincere thanks go to all colleagues, students, and family members who have supported and accompanied me during my research journey. In particular, I would like to thank:

- Prof. Dr. mont. Leonhard Ganzer for the opportunity to do scientific work and the continuous support throughout my academic career.
- apl. Prof. Dr. rer. nat. Bernd Flemisch for his valuable insights as a reviewer of this work and for the instructive stays in Stuttgart.
- Dr. Ing. Birger Hagemann for his outstanding support and the close and enriching collaboration over the last few years.
- my former colleagues and close friends, Gion Strobel and Maximilian Wirth, for the mostly stimulating discussions and shared experiences.
- my parents and my brother for their continued support throughout my studies.
- Kerstin for her generous understanding, patience, and support throughout the entire journey.

Contents

List of Figures

List of Tables

Chapter 1

Introduction

Within the last decade, an increasing shift from fossil fuels to renewable energy sources is evident with respect to the global climate movement. In Germany, the share of renewable energy sources of the electrical energy supply in 2021 was 43.9 %, where wind power delivered the main contribution of renewable (∼50 %), followed by photovoltaic (∼24 %), and biomass (∼17 %) [4]. Typically, the supply from renewable energy sources such as wind and solar is subject to fluctuations seasonally but also daily. A similar behavior is also observable for the energy demand, although the oscillation often differs significantly, leading to an increasing importance of energy buffers in a sustainable energy system for the future. Here, converting excess electrical energy into other energy carriers such as hydrogen, methane, and ammonia, which can be subsequently consumed when demanded, is regarded as a suitable solution (cf. Figure 1.1). This concept is called Power-to-X, whereby the X relates to the form of energy or usage (e.g. power-to-heat, power-to-gas, and power-to-liquid). Recently, hydrogen has been a promising candidate within the field of power-to-gas due to its versatile usage as an energy carrier and resource for various industries.

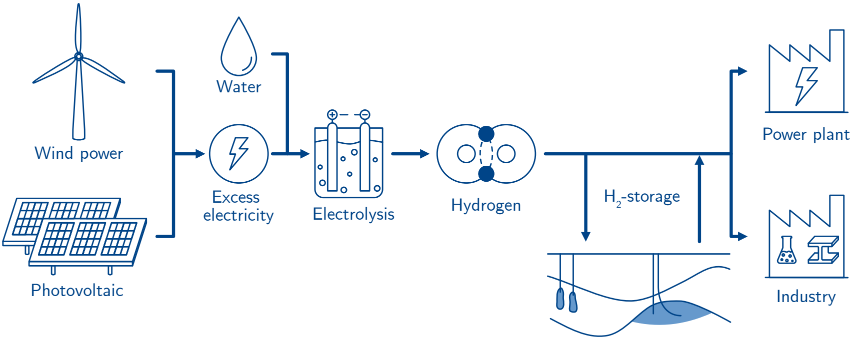

Figure 1.1: Workflow of the power-to-gas concept with hydrogen as energy carrier

Using hydrogen as a renewable energy carrier and simultaneously as a valuable resource for industries such as steel and chemicals will increase the overall demand in the following centuries. In 2019, Hebling et al. [59] prognosticated a hydrogen demand within a range of 250 TWh to 800 TWh for Germany by 2050 (800 TWh to 2250 TWh for Europe). Recent predictions are higher with an overall hydrogen demand of up to 1000 TWh for Germany and more than 4000 TWh for the entire EU by 2050 [51] (cf. Figure 1.2).

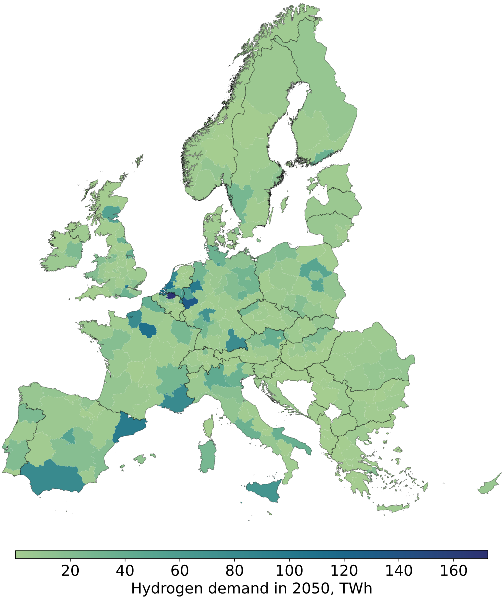

Figure 1.2: Overview of hydrogen demand by year 2050 [51]

Contemporary studies expect a storage capacity of 20 % to 30 % of the annual hydrogen demand [52]. The highest potential for renewable energy production and the use for hydrogen generation is located offshore (wind power) and in the southern part of Europe to the African region, which leads to large transport distances between producer and consumer [51]. Projects such as the European Hydrogen Backbone [154] are investigating the establishment of a European-wide reliable hydrogen pipeline grid and transportation system.

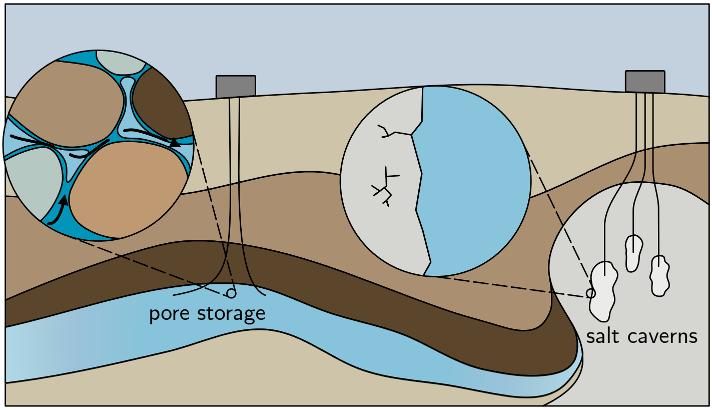

Figure 1.3: Overview of storage types - Stored fluid indicated with 🟦

Nevertheless, the fluctuations in demand and supply of energy and the geopolitical dependency lead to a more dominant role of energy storage in the future. Nowadays, energy storage in larger quantities is mainly performed by injecting natural gas and other hydrocarbon fuels into the subsurface, from which they can be withdrawn later. Generally, two types of underground gas storages (UGS) (cf. Figure 1.3) are used:

- Storage of gases and liquids in caverns, typically leached in salt formations such as salt diapers: Salt formations are crystalline rock entities usually with ideal sealing capacities. Typically, this type of storage allows high deliverability and hence is suitable for the short-term balance, allowing several storage cycles per year [85]. Due to their comparatively low capacities (geometrical size: 30 000 Sm^3 to 500 000 Sm^3) [144], caverns are often arranged in clusters. However, this type of storage is only feasible in regions with salt formations (e.g. Northern Germany), and therefore, their potential is limited.

- The cyclic injection and withdrawal of gases in porous and permeable rock formations, mainly depleted gas/oil fields: The storage formation composes a structural trap, where the cap rock prevents the migration of fluids to higher formations due to its extremely low permeability in combination with the capillary threshold pressure [78]. Typically, larger capacities can be observed, allowing seasonal storage, and due to the

> higher availability of suitable porous formations [85], the importance of this type of storage is significant with an increasing demand for storage capacities globally. However, the porous medium only allows lower injection and withdrawal rates per well than caverns and hence has only a limited contribution to short-term storage [144].

Overall, the coexistence of both storage types is favorable and behaves symbiotically to store energy and balance the changes in demand and production on a daily but also seasonal basis. In this study, the storage of fluids in porous rock formations is in focus due to its increasing importance regarding the growing hydrogen infrastructure. An overview of the history and current research on the storage of gases containing hydrogen in the subsurface is presented in the following. The concept of Underground Bio Methanation, derived from UHS, is also introduced.

1.1. Underground Hydrogen Storage

The storage of energy in the subsurface has more than 100 years of history. A first attempt to store natural gas in a depleted gas field was successfully carried out in Ontario, Canada, in 1915 [39]. The significance of subsurface energy storage increased over time, ensuring a consistent energy supply during low-production and high-demand periods. First storages for pure hydrogen were established in caverns to store hydrogen for petrochemical industry applications [87]. Initial experiences with storing hydrogen in porous formations were gained during the storage of hydrogen-rich town gas in Ketzin (Germany), Beynes (France), and Lobodice (Czech Republic) in the period between the 1950s and 1980s [100, 133]. With the growing interest in a carbon-free energy economy over the last century, the idea of storing green hydrogen in the subsurface gained traction, leading to research projects in both fundamental research and pilot phases.

In the 2010s, national research projects were initiated to improve the fundamental knowledge of UHS. Addressing the efficiency of the storage process, the research project *H2STORE* (2012 to 2015) [43] investigated the transport process in porous media and potential contamination due to microbial activity in numerical simulations. In the follow-up project *HyInteger* (2016 to 2019) [44], the attention was mainly placed on barrier elements, such as weakening wellbore components like cement and steel, and potential impacts on the formation by geochemical reactions. After performing laboratory experiments with wellbore materials at reservoir conditions, the risk of the hydrogen-induced integrity issues was concluded to be insignificant.

Aside from nationally funded research projects, also international projects were initiated to assess the technical feasibility of a large scale UHS strategy. Two relevant activities are the EU projects *HyStorIES* (2021 to 2023) [48] and *HyUSPRe* (2021 to 2024) [104]. Within these projects, various laboratory experiments (microbiology, geochemistry, geomechanics, and gas-gas mixing behavior) were conducted to tune field scale simulation models. Subsequently, these simulation models were used to identify potential risks and define guidelines for the operation. In addition to the technical assessments, economic studies and challenges regarding the general public acceptance were conducted.

Besides theoretical and laboratory investigations, first field tests were conducted to assess the feasibility of UHS. In 2013, RAG Austria AG initiated the research project *Underground Sun Storage* [126] addressing the storage of a hydrogen blend (up to 10 % of hydrogen) in a depleted gas field in Austria. The project began with fundamental investigations to assess potential impacts on storage integrity, with no direct issues observed. Subsequently, the planning, permission, installation, and operation of the UHS test followed. By the end of the pilot phase in 2017, a total amount of $1.22 \cdot 10^6\,\mathrm{Sm}^3$ of the hydrogen-natural gas blend was injected into the formation, with 18 % remaining stored after withdrawal. Notably, there were no hydrogen-related abnormalities during the operation [126]. The activity was continued within the project of *Underground Sun Conversion* (2017 to 2021) [124], and since 2023, the operation of UHS with pure hydrogen in a separate location is investigated within the follow-up project *Underground Sun Storage 2030* [125].

Almost parallel to the activities in Austria, the Argentinian company *Hychico* S.A. initiated a project focusing on the generation of renewable hydrogen followed by the injection into a depleted gas field in 2013 in cooperation with the French research organization BRGM [117]. However, the final outcomes of the project are still unpublished.

In the middle of 2023, the German company Uniper SE started the injection of a natural gas blend with hydrogen concentrations between 5 % to 25 % into a sandstone formation in Bavaria, Germany, within the project of *HySTORAGE* [141]. In three phases, the impact of gas-gas mixing with the initial gas and potential losses due to microbial activity will be assessed. The project is planned to be finished by 2025.

1.2. Underground Bio Methanation

During the storage of hydrogen-containing town gas, changes in fluid composition were observed. The observations were a decreasing hydrogen and carbon dioxide content with a simultaneous increase in the methane content. Later on, this shift was accounted to methanogenic microorganisms. This effect is unfavorable during UHS as a high purity of stored hydrogen is aimed. However, in the concept of Underground Bio Methanation/Underground Methanation Reactor (UMR), these methanogenic microorganisms are used to metabolize hydrogen and carbon dioxide in a 4:1 ratio to produce methane and water, which can remain in the storage and be withdrawn on demand [110]. Figure 1.4 shows a schematic overview of the concept with a doublet well setup where the conversion occurs during the flow from the injector to the producer well. The benefits of this idea are that the existing infrastructure

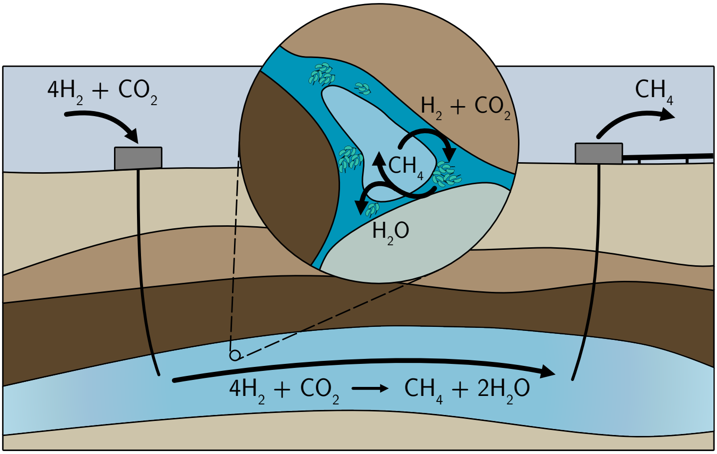

Figure 1.4: Schematic overview of the concept of an Underground Bio Methanation Reactor (UMR)

for natural gas can be utilized and that methane has a higher energy density than hydrogen, making this concept capable of higher energy storage capacity than a pure UHS.

Technology concepts are often classified by their technology readiness level (TRL) [35], categorizing the maturity of their progress. The TRL of UMR can be classified as TRL3, where the general concept is formulated and experimental proof has been provided. The experimental proof was achieved through a combination of laboratory experiments and conclusions from field tests. Research projects such as *BioUGS* [77] mainly focused on the growth kinetics of the microbial species in batch reactors (bulk) to estimate the resulting efficiency. The research activity *CliMb* (2019 to 2022) focused not only on the pure growth kinetics but also on the impact of the porous media and influences on the transport process. Overall, it proved the significance of the species present in the formation and the required environmental conditions to enable the potential of UMR on larger scales. With the initial intention of preceding investigations for a pilot phase, the project *UMAS* (2020 to 2022) [101] investigated the techno-economic assessment of a UMR in a former UGS in Germany. However, growth experiments indicated a complete inhibition of microbial growth due to the high salinity of the brine, which prevented the field case study [101]. In direct comparison, the previously mentioned UHS projects *Hychico* and *Underground Sun Conversion* were used to investigate the potential application as UMR where in both cases microbial activity led to the striven for conversion to methane [117, 124]. Within the activities of *Underground Sun Conversion*, a natural gas-hydrogen-carbon dioxide blend was injected (up to 20 % H_2) in the stoichiometric ratio (H_2:CO_2 4:1) to promote the microbial activity. Although a conversion could be observed, it fell short of expectations [124].

1.3. Motivation and objectives

The need for large-scale energy storage systems with an increasing share of renewable sources is evident. Storing hydrogen in the porous subsurface could contribute to this energy system significantly. However, the introduction of hydrogen can cause various phenomena. Numerical reservoir simulation is a powerful tool to model and predict the transport processes in porous rocks. In recent years, various simulations for UHS have been conducted. Regarding the field scale, most simulations focused on pure transport affected by different thermodynamic properties and hysteresis of relative permeability curves [15, 92], which have been observed in the laboratory. Additionally, simulation studies have been applied to evaluate operational designs, such as different types of cushion gas and well configurations [25, 33, 57]. However, these studies have often neglected hydrogen reactions, which are significant for particular storages. In 2018, Hagemann [54] developed a mathematical model with subsequent numerical implementation in the open-source simulator DuMu^x to predict the reactive transport process during hydrogen storage in the porous subsurface. This study's focus was modeling potential biochemical reactions caused by microorganisms being present in the pores of the rock. Regarding implementations in commercial simulators, simplified growth models were incorporated in some simulators [79, 157]. Focusing on the implementation of Hagemann [54], the work was primarily based on literature observations and lacked calibration with actual laboratory investigations. Other reactions, such as geochemical reactions, which could impact UHS efficiency, were not considered, and the analysis of gas-gas mixing between injected and initial gases was performed, but it relied on simplified thermodynamic properties (e.g. ideal gas law).

To address these limitations and enhance the existing implementation in DuMu^x, the following objectives were defined:

- Extending the existing simulation model by geochemical reactions (pyrite-to-pyrrhotite reduction) to predict the impact on UHS and introduce more applicable correlations regarding thermodynamic properties for the expected high pressure and temperature conditions.

- Calibrating the developed bio- and geochemical simulation model by matching laboratory observations regarding microbial growth parameters, geochemical reaction kinetics, and the gas-gas mixing by molecular diffusion to the model for subsequent field-scale application.

- Extending the modeling approach of mechanical dispersion to predict the gas-gas mixing more reliably in DuMu^x with subsequent prediction for a pilot UHS project.

- Testing the applicability of the developed implementation in DuMu^x to model freshwater injection to enable UMR in high-saline aquifers.

Achieving these objectives culminates in an improved numerical implementation, which allows for better certainty in predicting the processes during UHS. The model is accessible for public use on an open-source basis and is available to increase the efficiency of UHS through optimized operation.

1.4. Outline of the thesis

This thesis comprises six chapters and is structured as follows:

Chapter 2 depicts the fundamentals of relevant physicochemical processes related to the storage of hydrogen-containing gases within the subsurface based on a literature review. Particular focus is placed on hydrodynamics, biochemical, and geochemical reactions potentially influencing the efficiency of the storage process. Furthermore, this chapter provides the fundamentals of modeling two-phase multi-component transport in porous media, including the generalized mathematical model and its realization numerically.

In Chapter 3 an existing mathematical model for bio-reactive transport during UHS is extended by geochemical reactions (pyrite-to-pyrrhotite reduction) and consecutively implemented in the open-source simulator DuMu$^{\text{x}}$. Significant attention is placed on the calibration of the gas-gas mixing caused by molecular diffusion bio- and chemical reactions by recent laboratory experiments. The experiments are reproduced on a laboratory scale within simulations to achieve this calibration. In the final step, the developed and calibrated model is applied to a previously developed benchmark scenario for UHS to assess the risk on a larger scale.

Chapter 4 comprises the extension of the bio-reactive transport model concerning the gas-gas mixing caused by mechanical dispersion. Focusing on field scale simulations with conventional reservoir simulation grids, among other things, modifications in spatial discretizations and well modeling are required. The developed model is subsequently used to predict an ongoing pilot operation of UHS in Germany.

Within Chapter 5, the bio-reactive transport model is applied to predict the stimulation of microbial growth aiming for UMR. To counteract the inhibiting impact of high salinity brine on microbial growth, freshwater is injected, enabling the targeted growth of methanogenic archaea. To simulate this study, the microbial growth kinetics are extended by the influencing parameter of salt. Afterwards, a sensitivity study of microbial growth parameters and freshwater volume is performed.

Chapter 6 contains an overview of relevant conclusions from the results obtained in the previous chapters.

Chapter 2

Fundamentals and state of the art

Fluid flow in the subsurface during gas storage is a complex process. Due to the intricate geological system of the rock, the competitive flow of the injected gas and the water is affected by many factors. When introducing gases that have never been present in the formation, the composition of the gas mixture becomes significant. Chemical reactions may occur due to interactions with the minerals in the rock or with microorganisms adapted to the harsh conditions in the subsurface, which are particularly expected in UHS. This chapter covers the fundamentals of compositional multiphase flow in the subsurface. Focus is placed on effects that become relevant during the storage of hydrogen with respect to hydrodynamics, microbiology, and geochemistry, as found in recent literature. Furthermore, the fundamentals of modeling these processes within numerical simulation to replicate observed phenomena are elucidated.

2.1. Relevant processes during the storage of hydrogen in the subsurface

When storing gases in the subsurface, porous and permeable formations, including proper seals on all sides, are required. Suitable candidates are depleted gas fields where the pores are saturated with water and residual gas, but initially, fully water-saturated formations (aquifers) may also be appropriate [78]. The advantages of depleted gas fields compared to aquifers are that they typically have an already existing gas cushion that maintains the necessary pressure to ensure deliverability and safe operation [145]. This gas bubble has to be established for aquifer storage, and the initial pressure needs to be exceeded, coming with safety risks regarding the integrity [145]. Consequently, depleted gas fields are more favorable for gas storage than aquifers, and they are also preferred for UHS in general [24, 143, 153].

2.1.1. Hydrodynamics

Focusing on the transport process within the storage formation, the domain can be viewed at different scales, as depicted in Figure 2.1. The scales range from the microscale (e.g. adsorption of specific species at pore surfaces) over the pore scale, where the structure of several pores is examined, to the continuum scale (also known as the Darcy scale) [61]. The latter requires a challenging upscaling process, where the parameters of porosity and permeability are introduced [10]. Porosity represents the ratio of pore space to bulk volume, while permeability reflects flow conductivity (ease of flow). Upscaling allows for modeling larger structures, which can be challenging to parameterize properly. In theory, upscaling is based on representative elementary volumes, but at the field scale, parameters are typically obtained through investigations such as well logging and history matching in particular. Therefore, information is only investigated at specific points, and the majority of the parameters are obtained based on correlations and interpolation.

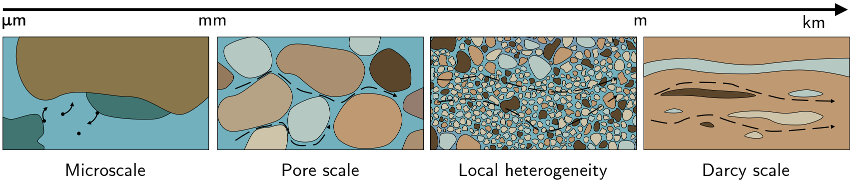

Figure 2.1: Scales of porous media (adapted from Kobus and de Haar [81])

2.1.1.1. Gas-water displacement

Depending on the storage history, the pores of the storage formation are filled with two immiscible phases (gas and water), separated by a clear interface. At the pore scale, the spatial distribution of saturation depends on fluid-matrix and fluid-fluid interactions, such as wettability, adsorption, and interfacial tension. Typically, in the presence of gas, water acts as the wetting phase (water-wet) and encases the rock surface [61]. This phenomenon leads to the side effect that smaller pores become saturated with water, while gas typically occupies larger pores. Furthermore, the interfacial tension between the wetting and non-wetting phases results in pressure differences between both phases, often referred to as capillary pressure or simply capillarity [61].

These fluid-fluid and fluid-matrix interactions have an impact on the distribution of gas and water in the pores, as well as on transport processes. To address the impact of these phenomena at the continuum scale, relative permeability curves and capillary pressure models are introduced [61]. In general, relative permeability indicates how easily one fluid flows in the presence of another. At low saturations, the wetting phase remains immobile and only the non-wetting phase can flow. Beyond a critical saturation (residual/connate saturation), the wetting phase starts to flow, and both phases become mobile until they reach the residual saturation of the non-wetting phase. At these saturations, the non-wetting phase behaves immobile. Models for macroscale fluid-fluid interactions typically describe both the behavior of relative permeabilities and capillary pressure (e.g. Van Genuchten [152] and Brooks and Corey [18]).

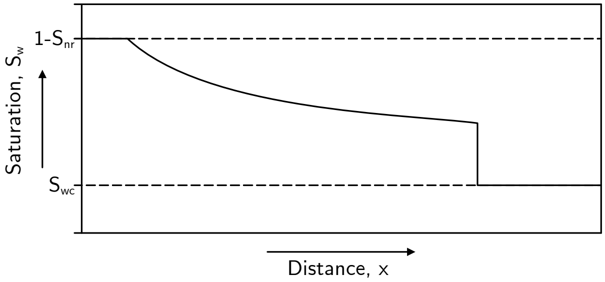

Figure 2.2: Displacement of the non-wetting phase by the wetting phase for a one-dimensional system but also valid vice-versa

Figure 2.2 illustrates the immiscible displacement for a one-dimensional system, which was initially mathematically described by Buckley and Leverett [20]. When one phase is injected into a two-phase saturated region, a front propagates through the porous medium. This displacement represents an advective flux, with the direction and strength controlled by the pressure gradient. Although the model of Buckley and Leverett [20] was developed for incompressible fluids, it is also valid for compressible fluids, assuming that the pressure difference is comparatively small, leading to neglectable compressibility. The front height generally depends on the ratio of phase mobilities (ratio of relative permeability to dynamic viscosity). After the front, the saturation gradually approaches the residual saturation of the displaced fluid.

However, the displacement process becomes more intricate in a more complex and multi-dimensional system. The impact of viscosity differences between the phases becomes more significant and variations in density can lead to phenomena that reduce the efficiency of the displacement process, potentially resulting in encapsulated gas bubbles [60]. Two critical phenomena are gravity segregation and viscous fingering (see Figure 2.3) [113]. Gravity segregation describes the effect where the combination of gravity and different densities of the phases leads to spatial separation. The lighter phase tends to move upwards, while the denser fluid accumulates in the lower zones. This effect is also known as density override/underride, where a significant volume of the formation is bypassed due to this separation. Originating from heterogeneities at the pore scale, fingers appearing at the front of the main flow direction can lead to an unstable displacement, which is known as viscous fingering or Saffman-Taylor instability [128]. As the flow resistance lowers, the fluid tends to follow these fingers and the effect propagates. However, viscous fingering is observed only when a less viscous fluid displaces a higher viscous one and the mobilities vary significantly.

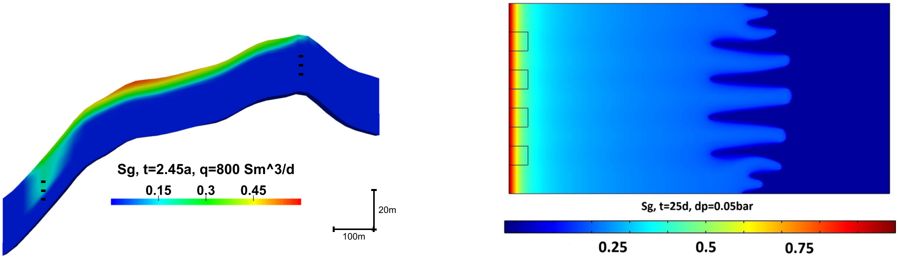

(A) Gravity segregation due to significant density differences

(B) Saffman-Taylor instability due to strong viscosity differences

Figure 2.3: Impact of the physical properties of density and viscosity on the displacement process in porous formations [36]

The occurrence and strength of these phenomena during the storage of gases in the subsurface depend on the initial conditions. In the case of aquifer storage, the initial water must be displaced by either the cushion gas or hydrogen, which poses a higher risk for phenomena such as gravity segregation and viscous fingering. Nevertheless, these phenomena can also occur during storage in depleted gas fields. Moreover, both are expected during subsurface gas storage, often occurring simultaneously. However, gravitational forces tend to dominate during slow injection rates, while viscous fingering is more likely at higher rates [113].

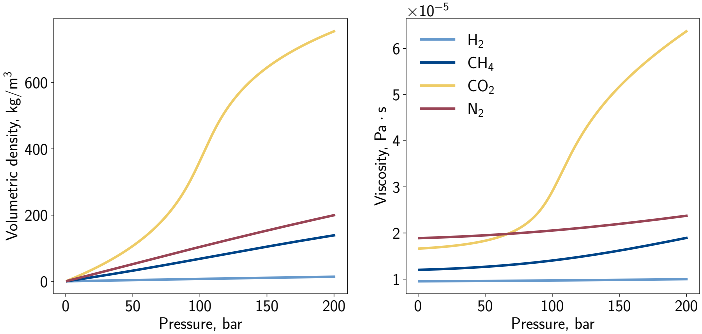

Figure 2.4: Volumetric density and viscosity of relevant gases at 50 °C, calculated using Peng-Robinson EoS [116] and viscosity model according to Stiel and Thodos [134]

When focusing on UHS, the unique properties of hydrogen promote the effects of unstable displacement. Figure 2.4 illustrates the thermodynamic properties of density and dynamic viscosity for relevant storage fluids, highlighting the differences between the main component of natural gas, methane, and hydrogen. Both the density and viscosity of methane are significantly higher than those of hydrogen (e.g. $\mu_{\mathrm{CH_4}}/\mu_{\mathrm{H_2}} \approx 1.5$, $\rho_{\mathrm{CH_4}}/\rho_{\mathrm{H_2}} \approx 9.4$ at $T = 50\,^\circ\mathrm{C}$ and $p = 100\,\mathrm{bar}$). In comparison to the liquid phase, the tendency for gravity segregation and viscous fingering is expected to be higher for hydrogen than for methane representing the dominant gas component of natural gas with concentrations higher than 90 % [36, 54, 113]. To mitigate the impact of unstable displacements on storage efficiency, well placement and injection rates must be chosen with particular care [113].

2.1.1.2. Gas-gas mixing

During the transformation from an existing natural gas storage or depleted gas field to UHS, the mixing of the injected gas and the initial gas cushion becomes relevant. Unlike gas-water displacement, the displacement of one gas by another gas is considered a miscible process, where the displacement front is not sharp but instead smeared out due to mixing [9]. Figure 2.5 illustrates the distribution of miscible displacement, analogous to the displacement described by Buckley and Leverett [20] (cf. Figure 2.2).

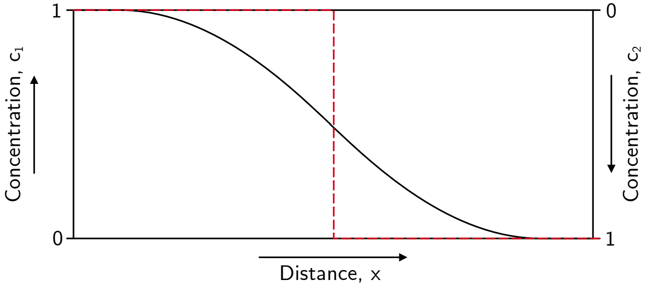

Figure 2.5: Miscible displacement of one species by another one. The red dashed line indicates piston-like displacement without mechanical dispersion and molecular diffusion; the solid black line represents the true concentration distribution

Besides the advective flow, the mixing of species is primarily caused by two effects: molecular diffusion and mechanical dispersion. Molecular diffusion can be defined as the flux resulting from the tendency to balance concentration differences due to the Brownian motion of molecules [19, 37] (cf. Figure 2.6). Generally, this process is assumed to be slower than the advective flux, but the higher the concentration gradient, the faster the diffusive flux and mixing behavior [37]. In porous media, gas-gas diffusion can only occur within the pores, which decelerates the process compared to open flow due to the

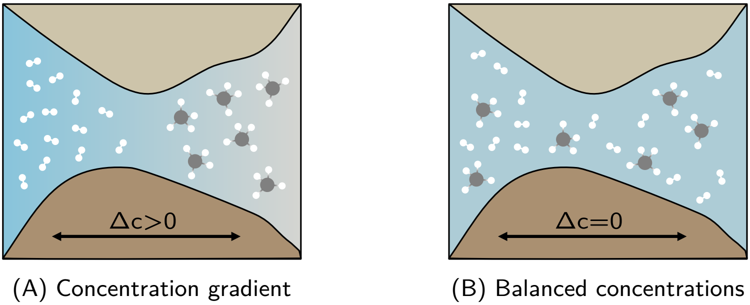

(A) Concentration gradient

(B) Balanced concentrations

Figure 2.6: Process of molecular diffusion inside a pore

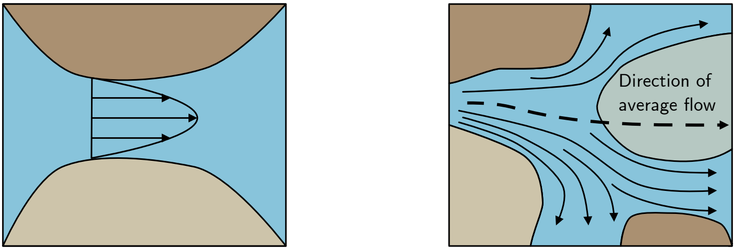

(A) Varying velocity profile in the pore throat

(B) Diverging velocity field from main flow direction

Figure 2.7: Mixing of a component caused by mechanical dispersion (adapted from Bear [9])

reduced space available for exchange [9]. Parameters like porosity, saturation, and tortuosity influence the modeling of effective diffusion coefficients. Due to its small molecule size, hydrogen possesses high diffusivity coefficients, which are expected to be larger for hydrogen compared to other species [3]. Since the highest gradients are present during the initial injection of hydrogen, this process is expected to reduce with later cycles and is most sensitive during idle periods due to the reduction in velocity [36]. Unlike molecular diffusion, mechanical dispersion originates from the complexity of a porous medium, resulting in different lengths of flow paths and varying flow velocities at the microscopic level [9]. This process encompasses various phenomena occurring at the pore scale (cf. Figure 2.7) and is exclusively on the continuum scale. It includes effects like reduced flow velocities at the surface boundaries and deviations in the flow direction within pores from the mean flow direction. Typically, the strength of the dispersive flux depends on the phase's flow velocity [130] combined with microscale heterogeneity. However, macroscale heterogeneities can also increase dispersivity. Consequently, mixing is accelerated in the presence of strong inhomogeneities and high flow velocities [9].

Hence, the miscible displacement combines the advective (pressure-driven) flux with a dispersive/diffusive flux component that depends on the concentration gradient. In the context of storage operations, this signifies that the previously mentioned problems, such as gravity override and viscous fingering, are also promoted in the case of gas-gas displacement due to variations in thermodynamic properties of the gases (cf. Figure 2.3) [54, 113]. Analogous to gas-water displacement, these phenomena can be mitigated by properly

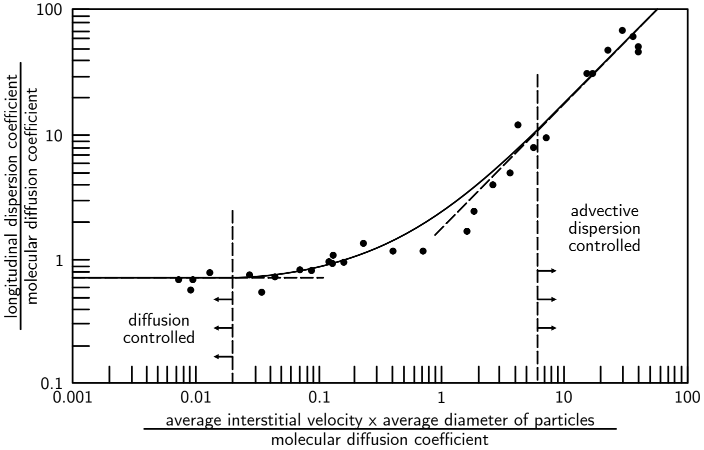

Figure 2.8: Diffusive and dispersive mixing regimes in porous media (adapted from Perkins and Johnston [118])

selecting operational rates and well placement [113]. A similar situation can be observed in gas-gas mixing, as depicted in Figure 2.8. While the effect of molecular diffusion never disappears as long as a concentration gradient persists, it becomes the dominant flow process at low flow velocities [118]. In contrast, with higher flow velocities, mechanical dispersion governs the gas-gas mixing [118]. Applying this knowledge to UHS operations, the temporary loss into the cushion gas due to molecular diffusion is most noticeable during the shut-in/idle phases of operation, while the contribution of the dispersive flux increases with high operational rates.

2.1.2. Microbiology

It is generally accepted that the surface offers ideal conditions for organisms to survive, which is why one might assume that the subsurface represents the complete opposite. However, even under these harsh conditions of high temperatures, pressures, and salinities, organisms have evolved and adapted to thrive in such environments, enabling them to reproduce and preserve their species [50, 90]. These organisms are typically invisible to the unaided eye and exist as single-celled entities. They are often referred to as bacteria and archaea that are classified as prokaryotes, in contrast to eukaryotes, which include multicellular organisms such as animals, plants, and fungi [29]. Prokaryotes exist in various sizes and morphological shapes, such as spherical, cylindrical, and spiral. Observed diameter sizes range from <0.2 µm to 700 µm, whereby the majority posses a diameter between 0.5 µm to 4 µm and a length below 15 µm [93, 127]. Even at these small sizes, single-cell organisms contain all the necessary components to maintain metabolism and reproduce. In principle, prokaryotes are composed of the following: 1) cell wall, 2) cytoplasmic/cell membrane, 3) cytoplasm, 4) nucleoid, and 5) ribosomes (cf. Figure 2.9) [93].

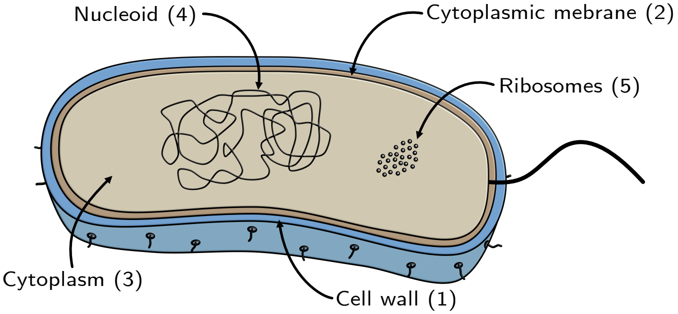

Figure 2.9: Schematic overview of important components of a prokaryotic cell

As the outer layer, the cell wall provides protection against osmotic pressure caused by dissolved molecules and protects against environmental impacts. Prokaryotes are classified into archaea and bacteria based on the composition of their cell walls. While bacteria have cell walls composed of peptidoglycan (murein), archaea have cell walls composed of protein, polysaccharide, or pseudomurein [29]. As the second layer, the cytoplasmic membrane is a highly selective permeable barrier that separates the surrounding environment from the inner part of the microorganism's cell. It enables interactions with the surrounding environment, such as substrate absorption for energy supply, nutrient uptake, and waste discharge. The inner part of the cell is filled with the so-called cytoplasm, which is composed of water and essential components required for the function of the cell. Additionally, the ribosomes and the DNA in the form of chromosomes are embedded in the gel-like substance [112]. Ribosomes are composed of ribosomal RNA (rRNA) and protein, and they play a crucial role in protein synthesis for the organism [112].

The core of the prokaryotic cell is the nuclear region, which contains the DNA in the form of chromosomes holding the genetic code for heredity. The chromosomes are often referred to as the blueprint of the organism since they contain instructions for growth, development, survival, and reproduction. While eukaryotic cells have their chromosomes located within an additional layer of membrane (nucleus), the chromosomes of prokaryotic cells are loosely situated in the cytoplasm [112]. In addition to these main components, prokaryotic cells possess minor components such as inclusions and plasmids [112]. Some bacterial cells have filamentous (fimbriae/pilli) appendages, enabling them to interact with the environment (e.g. attachment to surfaces). Larger appendages are called flagella, allowing the cell to move within liquid phases with the principle of a propeller [112].

The microorganisms require energy and nutrients to maintain their metabolism to grow and reproduce, ensuring the species' continued existence. The microorganism's metabolism is often associated with biosynthesis. Generally, the energy can be supplied by either chemical (chemothrophs) or light (phototrophs). Most of the procaryotes use the oxidation of inorganic chemicals (e.g. hydrogen (H_2) and ferrous iron (Fe^{2+})) to harvest energy. Besides the energy, the organism requires a carbon source for metabolism. There are two options: autotrophs directly use carbon dioxide (CO_2) as their carbon source, while heterotrophs obtain carbon from other sources and depend on other organisms [93]. While elements such as hydrogen, carbon, and nitrogen count as macronutrients, the majority of the elements are only required in small amounts (micronutrients/trace elements) [93]. Typically, a cell composes approximately 99 % of macronutrients (H, C, O, N, P, and S), while micronutrients are required for the production of functional components such as enzymes and vitamins [93].

2.1.2.1. Microbial growth and modeling approach

A sufficient amount of nutrients/substrates and energy allows microorganisms to reproduce themselves. For procaryotes, reproduction is achieved by the process of cell division (cf. Figure 2.10), which leads to an increased number of cells, stated as microbial growth [93]. Before the cell division occurs, the cell typically elongates to double the initial size with a contemporaneous duplication of the chromosomes and relevant components (e.g. ribosomes). Afterwards, the so-called septum is formed by in-warding growth of the outer

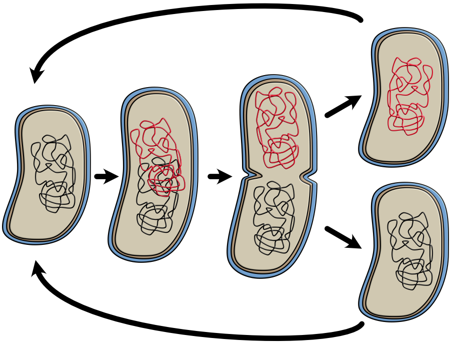

Figure 2.10: Schematic representation of cell division (binary fission)

layers of the cell, leading to a continuous separation of the cells until the full division is completed [29]. This division into two equivalent daughter cells from one mother cell is called binary fission and is conducted by most prokaryotes. For some microorganisms, the original cell is preserved while a completely new cell is formed separately (budding division) [93]. The timing of one cell division strongly depends on the species, nutrient supply, and environmental factors, but typically, it ranges from a couple of minutes up to days or months [29]. Environmental impact factors are temperature, salinity, and pH in particular. Typically, microorganisms have a viable window to survive, including an optimum at which the growth is at its maximum.

Today, laboratory experiments are commonly employed to quantify the growth rates of microbial populations and study their growth conditions. One prevalent experimental approach is the use of batch experiments (see Figure 2.11),

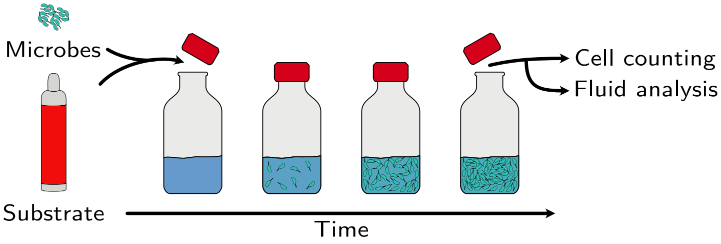

Figure 2.11: Schematic experimental procedure of a static batch experiment

in which a culture of microorganisms is exposed to a substrate under controlled conditions, including factors like pH, temperature, and pressure. Before introducing the substrate, the initial quantity of microorganisms is assessed, and the growth of the population is subsequently monitored. To measure the cell number within the reactor, two common methods are used: 1) extracting a fluid sample and counting the number of cells (plate counting), and 2) assessing turbidity, which quantifies the cloudiness of the fluid through light scattering (turbidimetric/optic density measurement) [93].

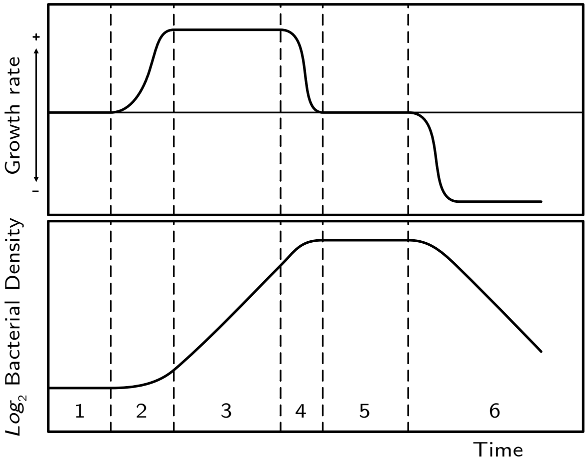

Figure 2.12: Different phases of microbial growth according to Monod [102] (redrawn) - 1. lag phase; 2. acceleration phase; 3. exponential phase; 4. retardation phase; 5. stationary phase; 6. phase of decline

In general, the quantification of microorganisms is expressed in biomass per volume [g/m^3] or, alternatively, in cells per volume [1/m^3], which is referred to as microbial density (n). In this study, the latter dimension is used. In the simplest case, the batch experiment involves a one-time supply of nutrients. In the 1940s, Monod [102] observed during these types of experiments that the growth of a culture can be described with six phases (cf. Figure 2.12):

1. *Lag phase*: The microorganisms need time to adapt to the new environmental conditions. During this phase, there is no significant change in the number of cells, but the cells grow and maintain their metabolism [112]. The duration of the lag phase can vary, lasting from a few hours

to several days until an increase in the culture size becomes noticeable [155].

$$\frac{\mathrm{d}n}{\mathrm{d}t} = 0 \tag{2.1}$$

2. *Acceleration phase*: After adapting to the environment, cells start to divide, and the growth rate of the population increases [102].

$$0 < \frac{\mathrm{d}n}{\mathrm{d}t} < \psi_{\mathrm{max}}^{\mathrm{growth}} n \tag{2.2}$$

3. *Exponential phase*: During the exponential phase, the culture achieves its maximum growth rate ($\psi_{\mathrm{max}}^{\mathrm{growth}}$), and cell division accelerates exponentially. This is considered the healthiest phase with maximal metabolism [93].

$$\frac{\mathrm{d}n}{\mathrm{d}t} = \psi_{\mathrm{max}}^{\mathrm{growth}} n \tag{2.3}$$

4. *Retardation phase*: With increasing substrate depletion and accumulation of waste products, the growth rate starts to decrease. Nevertheless, the culture size continues to increase [102].

$$0 < \frac{\mathrm{d}n}{\mathrm{d}t} < \psi_{\mathrm{max}}^{\mathrm{growth}} n \tag{2.4}$$

5. *Stationary phase*: Growth of the culture halts with a zero net growth rate due to substrate limitations. Organisms enter a starvation/survival mode, and the number of growing cells reaches an equilibrium with dying cells. Metabolism continues, but at a significantly reduced rate [29].

$$\frac{\mathrm{d}n}{\mathrm{d}t} = 0 \tag{2.5}$$

6. *Decay/decline phase*: The absence of substrate and the accumulation of waste products result in an increased decay rate, leading to a negative growth rate and a decrease in the population size. This phase is perceivable with an extended observation period [29].

$$\frac{\mathrm{d}n}{\mathrm{d}t} < 0 \tag{2.6}$$

Phases 2 to 4 are often summarized under the term log phase due to the typical logarithmic plotting of growth. It is worth noting that specific phases, such as the lag phase, may be absent or not observable under certain circumstances. However, it is generally expected that the observed growth in batch experiments is significantly higher than in-situ conditions because of artificially ideal growth conditions provided in the laboratory [93].

When it comes to understanding and predicting microbial growth, mathematical models are employed to describe the size of observed cultures. Typically, these models assume that growth is governed by the availability of substrates (substrate-limiting). However, in some cases, substrate availability may not be the limiting factor, and other factors may hinder growth, such as space limitations or absent micronutrients/trace elements.

One of the most popular substrate-limited models is the Monod model [102], which is expressed as follows:

$$\psi^{\text{growth}} = \psi^{\text{growth}}_{\text{max}} \left(\frac{c^S}{\alpha + c^S} \right) \tag{2.7}$$

where ψ^{growth} is the growth rate in 1/s, $\psi^{\text{growth}}_{\text{max}}$ is the maximum growth rate in 1/s, c^S is the molar concentration of the substrate S, and α is the half-velocity constant. The dimensions of c^S and α are selected identically (e.g. mol/mol).

To limit the growth and replicate the decay phase, the growth model is often extended by a decay term so that the change in the culture's population yields:

$$\frac{\mathrm{d}n}{\mathrm{d}t} = \psi^{\text{growth}} n - \psi^{\text{decay}} n \tag{2.8}$$

where ψ^{decay} is the decay rate in 1/s.

During the development of a growth model for UHS application, Hagemann [54] suggested two models for the decay term:

- Constant decay rate:

$$\psi^{\text{decay}} = b \tag{2.9}$$

- Increasing (linear) decay rate:

$$\psi^{\text{decay}} = bn \tag{2.10}$$

where b is the decay coefficient.

Figure 2.13 depicts the comparison of relevant growth models (Monod [102], Moser [103], and Panfilov [110]) for an arbitrary batch experiment. It is necessary to mention that it was not possible to replicate the lag and stationary phase for the selected models. Instead of the lag phase, the Monod and Moser models start directly in the exponential phase, while for the model of Panfilov, an acceleration phase can be observed [54].

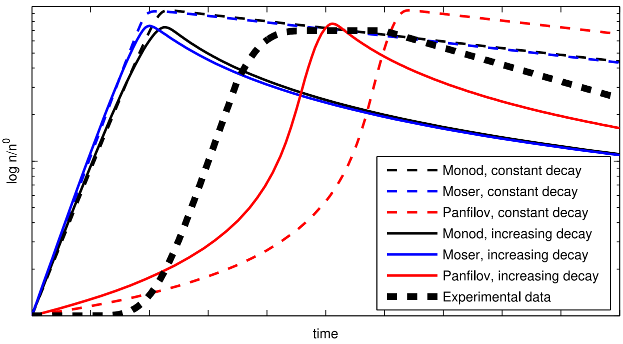

Figure 2.13: Comparison of relevant growth models reproducing an arbitrary batch experiment [54]

Besides these, there are more models available describing the growth, partially allowing to model these regions. However, they lack simplicity due to more tuning/influencing parameters and a direct dependency on time (t) [94].

2.1.2.2. Microbial activity during UHS

The first indicators of the presence of microorganisms in the subsurface arose in the early 1930s, when microbial growth was observed in subsurface rock samples [90]. However, the observations were often severely questioned and explained by contamination during the sample extraction. In the late 1980s, research on microbiology in the underground received new attention, and the first guidelines for sampling were published [50]. With respect to hydrogenotrophic microorganisms, first experiences were obtained during the storage of hydrogen-containing town gas in Lobodice, Czech Republic. During the storage operation, a loss of 10 % to 20 % of the working gas with simultaneous changes in the fluid compositions was observed (cf. Figure 2.14) [133]. A substantial decrease of hydrogen ($\Delta c^{\mathrm{H_2}} = -17\,\%$) and increase of methane ($\Delta c^{\mathrm{CH_4}} = 19\,\%$) led to the hypothesis of the presence of methanogenic microorganisms consuming the stored hydrogen for their metabolism [133]. Later on, isotopic analyses proved that biogenic methane was generated by microorganisms.

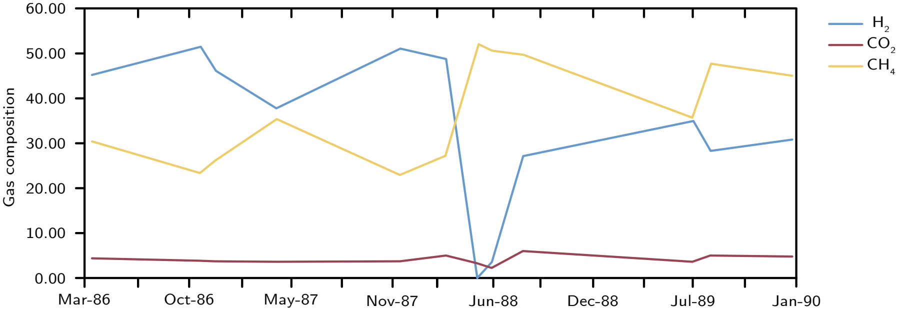

Figure 2.14: Changes in fluid composition during the storage of town gas in Lobodice in the late 1980s (adapted from Buzek et al. [22])

Since the increasing interest in large-scale UHS in the 2010s, more attention has been spent on understanding and characterizing hydrogenotrophic microorganisms. The main reason is the potential risk of changes in fluid composition and contamination of the stored fluid that may even generate harmful components such as hydrogen sulfide [60, 147]. Furthermore, the accumulation of microbes on the grain surfaces may lead to an alteration of petrophysical properties and, thereby, deliverability and storage capability.

With a focus on changes in fluid composition, the most prominent hydrogenotrophic microorganisms are the following [147]:

- *Methanogenic archaea* utilize hydrogen as an electron donor and carbon dioxide as the carbon source for metabolism. Simultaneously, they produce methane and molecular water. This reaction is also known as methanation:

$$4H_2 + CO_2 \longrightarrow CH_4 + 2H_2O \tag{2.11}$$

During the storage of hydrogen in the subsurface, this reaction is unfavorable. However, with respect to the concept of UMR, these archaea are selectively utilized to increase the stored energy capacity [137].

- *Sulfate-reducing bacteria* are consuming hydrogen and sulfate with the generation of hydrogen sulfide [8].

  $$5H_2 + SO_4^{2-} \longrightarrow H_2S + 4H_2O \tag{2.12}$$

  Besides the loss in hydrogen content and purity, hydrogen sulfide is a toxic and corrosive gas leading to additional safety aspects and processing steps [30, 34, 147].

- *Homoacetogenic bacteria/archaea* use, similar to the methanogens, hydrogen as electron donor and carbon dioxide as carbon source, but discharge acetic acid and molecular water:

  $$4H_2 + 2CO_2 \longrightarrow CH_3COOH + 2H_2O \tag{2.13}$$

  The product acetic acid can induce a change in the pH value of the reservoir water and promote further reactions due to disturbance of equilibrium [89].

In addition to the prominent species, there are other hydrogenotrophic microorganisms, such as iron-(III)-reducing organisms or those following slightly different reaction pathways. The simultaneous presence of species leads to competitive behavior. For instance, Siegert et al. [132] observed that in the presence of methanogenic archaea and sulfate-reducing bacteria, sulfate reduction outcompetes methanation when sulfate concentrations in the aqueous phase exceed 50 mM. Below this threshold, the metabolism of methanogenic archaea is accelerated compared to sulfate-reducing bacteria [132]. Furthermore, due to the lower Gibbs energy (ΔG) and a relatively high hydrogen threshold compared to other reactions, it is expected that homoacetogenic bacteria are outcompeted by other microorganisms and may dominate only in the absence of other species [2, 147]. Nevertheless, the presence of these species strongly depends on the geological formation and may even be affected by contamination during the development and operation of the storage [147].

Most of the published microbial growth data was obtained under ideal conditions in incubation and batch experiments and may vary from the conditions inside natural porous media. In the gas-water saturated rocks, the interfacial area between the phases is larger than in the experiments, which could yield a faster supply of substrates in the aqueous phase, in reality [142]. Nevertheless, the growth observed in batch experiments is likely to be too optimistic, and in-situ, the population's dynamic is limited by factors such as micronutrients and space [135]. Therefore, a reliable transfer from laboratory to in-situ growth parameters is still an active area of research.

As mentioned earlier, microbial growth requires appropriate growth conditions. Characterizing the growth conditions has generated big interest leading to much research within the last years. The impact of temperature, salinity, and pH on the viability of the species is commonly investigated. A first database containing optimum and critical growth parameters was published by Strobel et al. [139] and Thaysen et al. [147]. Histograms of optimum growth conditions for different species are depicted in Figure 2.15. Generally said, most microorganisms prefer temperatures of approximately 30 °C to 40 °C, low salinities ($< 50\,\mathrm{g/l}$), and neutral pH values. Nevertheless, some species also possess a viable window in harsher conditions. This leads to the implication that biochemical reactions are more expected in shallow formations having mild conditions ($T < 55\,^{\circ}\mathrm{C}$, $S_{\mathrm{NaCl}} < 100\,\mathrm{g/l}$) and formations containing high water saturations (e.g. aquifer) [148].

Besides the changes in the fluid composition, microbial activity can also impact the flow behavior within the pores. The organisms are living in the aqueous phase and can be in suspension (planktonic) or attached to the surface (biofilm) [112]. While planktonic individuals are subject to the general transport process in porous media, the biofilm is assumed to be immobile. On a geological scale, the nomenclature of attached and detached bacteria is often used because, due to the narrow pore space (same order of magnitude as size the size of bacteria), a fully developed biofilm can not be created [31]. However, bacteria can plug pore throats and thereby reduce the effective permeability, which is often stated as bio-plugging/clogging and can have a significant impact on the operation. For the operation of UHS in formations with significant amounts of mobile water like aquifer storages, the risk of

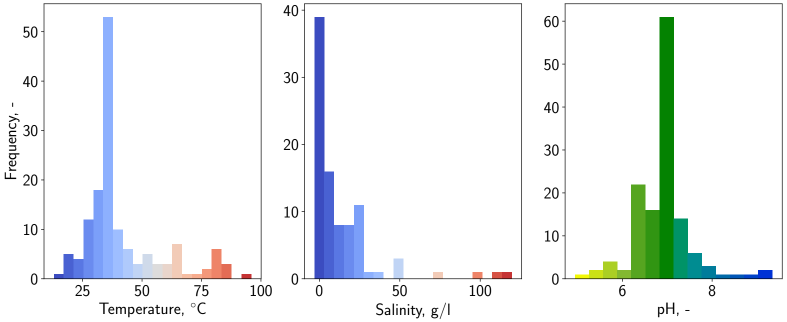

(A) Methanogenic archaea - $\Delta T_v = 26\,^\circ C$; $\Delta S_v = 69\,g/l$; $\Delta pH_v = 2.3$

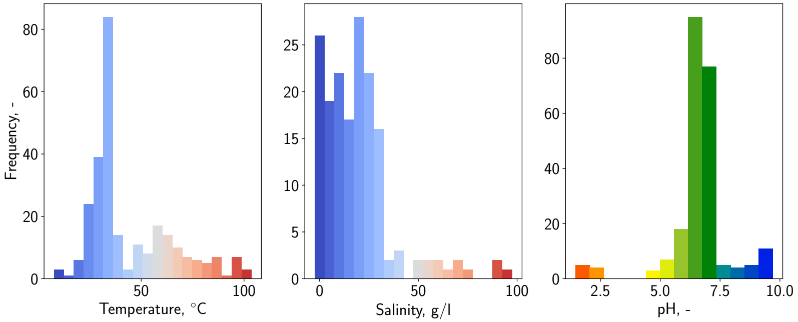

(B) Sulfate reducing bacteria - $\Delta T_v = 24\,^\circ C$; $\Delta S_v = 80\,g/l$; $\Delta pH_v = 2.5$

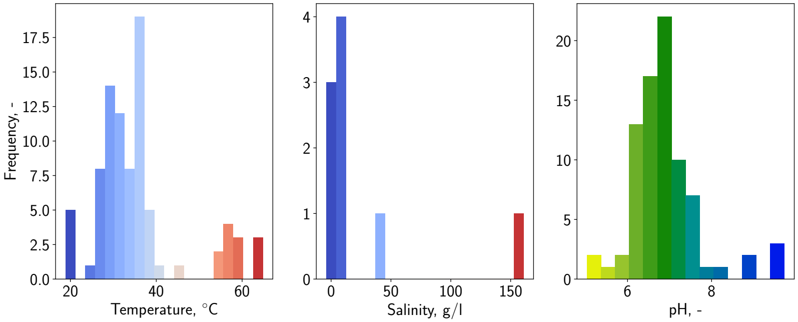

(C) Homoactogenic bacteria - $\Delta T_v = 27\,^\circ C$; $\Delta S_v = 43\,g/l$; $\Delta pH_v = 2.2$

Figure 2.15: Histograms of optimum growth conditions of different types of microorganisms including the average viable window Δ_v (data from [139, 146])

pore-clogging is expected to be higher. Contrary, the likelihood of significant impacts on the petrophysics in depleted gas fields is limited and most likely restricted to the gas water contact/transition zone.

2.1.3. Geochemical reactions

Typically, natural gas fields are several tens of millions of years old, allowing the complete system to reach thermodynamic and chemical equilibrium. However, these equilibria are disrupted by the injection of new chemical components such as hydrogen. Among other things, these new chemical components may induce reactions with the rock minerals [60]. These types of reactions, where dissolved components in the fluids interact with the minerals of the rock, are referred to as geochemical reactions [12]. Geochemical reactions often follow a path of mineral dissolution, where one or more minerals dissolve in the liquid phase and react, followed by either remaining dissolved or precipitating out of solution [13]. While dissolution typically enhances petrophysical properties, precipitation can lead to pore clogging or even cause geomechanical issues. Furthermore, the reaction products can contaminate the stored fluids, making them unfavorable.

2.1.3.1. Modeling of geochemical reactions

The utilization of geochemical models to reproduce and predict the behavior of a system has played an increasingly significant role over the past 60 years [13]. With the advancement in computing power, it has become possible to model complex systems involving various components in the solid phase (e.g. minerals) and the fluid phase. The ultimate goal in the field of geochemical modeling is to develop models that closely replicate reality while maintaining a practical balance [13].

To build a suitable model, the mechanism of a reaction has to be understood. In order to introduce the geochemical modeling approach, a hypothetical reaction is assumed, which takes place according to the following stoichiometry:

$$\alpha A + \beta B \rightleftharpoons \delta D + \varepsilon E \tag{2.14}$$

where A, B, D, and E are the species and α, β, δ, and ε are the stoichiometric coefficients.

In general, the reaction can take place in both directions and it will tend towards the chemical equilibrium (lowest free Gibb's energy) [13]. As can be seen in Figure 2.16, the equilibrium point is located between both single states and implies that in equilibrium all species are present [123].

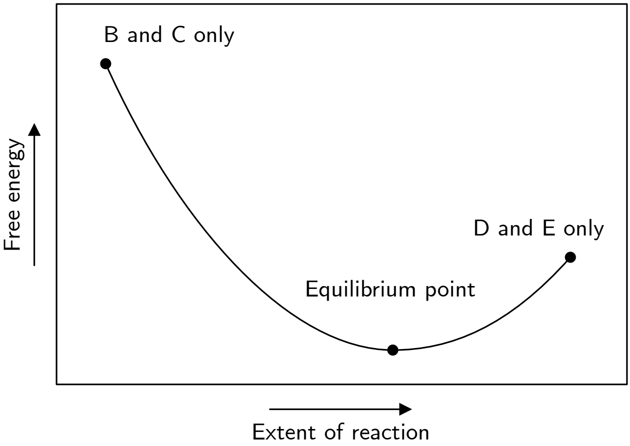

Figure 2.16: Chemical equilibrium and its tendency towards the lowest free energy (adapted from Bethke [13])

The level of equilibrium at an arbitrary point in time is often expressed by the reaction quotient Q_m:

$$Q_m = \left(\frac{a_D^{\delta} a_E^{\varepsilon}}{a_A^{\alpha} a_B^{\beta}} \right)_t \tag{2.15}$$

where a_S is the activity of species S.

For equilibrium, the reaction quotient is equal to the equilibrium constant (mass action coefficient) K_m:

$$K_m = \frac{\tilde{a}_D^{\delta} \tilde{a}_E^{\varepsilon}}{\tilde{a}_A^{\alpha} \tilde{a}_B^{\beta}} \tag{2.16}$$

where $\tilde{a}_S$ corresponds to the activity of the species S at equilibrium.

Two approaches are commonly used in geochemical modeling: 1) equilibrium-based models and 2) kinetic/rate models. The first model assumes that the geochemical equilibrium ($Q_m = K_m$) is achieved at every point in time. The second model type considers the presence of chemical non-equilibrium, which is progressively approaching the equilibrium state. A typical description for a kinetic model was developed by Lasaga et al. [84]:

$$r_k = -\frac{\mathrm{d}n_k}{\mathrm{d}t} = A_s k \left(1 - \frac{Q_m}{K_m}\right)^{\theta} \tag{2.17}$$

where r_k is the rate in mol/s, A_s is the specific reactive surface area of the mineral in m^2, k is the rate constant in $\mathrm{mol}/(\mathrm{m}^2 \cdot \mathrm{s})$, and θ is a tuning parameter (often assumed to be unity). Typically, the rate constant depends on temperature (exponential impact) and activation energy. The model allows the reaction to proceed forward ($Q_m/K_m < 1$) and backward ($Q_m/K_m > 1$), whereby the equilibrium is achieved for $Q = K$.

The model selection depends on the reaction itself, where the time scale is the most important selection criterion. Here, the reaction can be classified into three groups: 1) the reaction occurs slowly in comparison to the time of interest so that the reaction can be neglected (modeling not required); 2) The reaction rates are so fast that the system equalizes (equilibrium modeling); and 3) all remaining reactions (kinetic modeling) [13]. Besides this general formulation, a rate/kinetic relationship owns a high degree of freedom describing reaction behavior [13].

2.1.3.2. Geochemistry during UHS

The increasing interest in UHS over the last years has promoted investigations of potential geochemical interactions involving stored hydrogen. A lot of attention is focused on potential hydrogen losses, contamination, influences on petrophysical properties, and reduction of rock strength, which impact the overall safety of the operation.

The most prominent reaction is the pyrite-to-pyrrhotite reduction, where hydrogen sulfide is produced, coming with corrosive and harmful characteristics. Pyrite ($\mathrm{FeS_2}$) can be frequently found in low concentrations up to a few percent in many sandstones [119], and the reaction may become relevant for many storage formations. In general, the reaction of dissolved pyrite with consecutive precipitation of pyrrhotite (FeS) has the following stoichiometric equation [56]:

$$FeS_2 + (1-x)H_2 \rightleftharpoons FeS_{1+x} + (1-x)H_2S \quad (0 < x < 0.125) \tag{2.18}$$

The hydrogen sulfide generation may impact, on the one hand, the reproduction of harmful gas, which requires additional processing steps, leading to significant cost increases in operation. On the other hand, the integrity of the well may be endangered due to its corrosive effect on wellbore materials. First concerns of this reaction occurring during UHS arose when storing town gas (mixture of ≈ 60 % H_2, 20 % CO_2 and CO, and 20 % CH_4) in Beyne, France [17]. However, the observed hydrogen sulfide concentration of 20 mg/Sm^3 did not necessarily conclude the presence of the reaction and could also be explained by sulfate-reducing bacteria [17]. Later on, the reaction was investigated experimentally in Truche et al. [150] focusing on nuclear waste disposals. During the exposure of pure pyrite, an abundant amount of the pyrite was reduced to pyrrhotite (cf. Figure 2.17) with the simultaneous generation of hydrogen sulfide within two weeks. However, the investigated

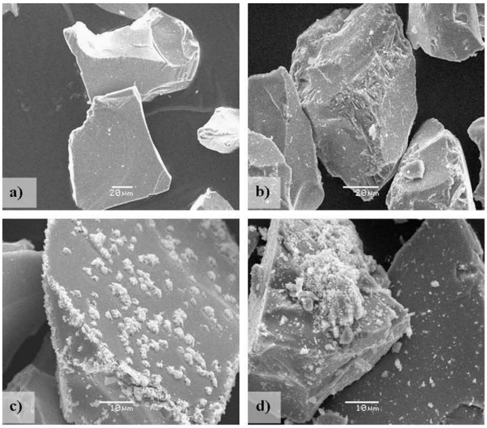

Figure 2.17: Scanning electron microscope (SEM) images of pyrite-to-pyrrhotite reduction observed in Truche et al. [150] - a) pure pyrite sample (40 µm to 80 µm sized); partially reacted pyrite after 300 hrs: b) 90 °C, p_{H_2} = 8 bar; c) 150 °C, p_{H_2} = 8 bar; d) 150 °C, p_{H_2} = 15 bar

experimental conditions of temperature ranges 90 °C to 180 °C and pressures from 80 bar to 140 bar (10 % H_2), respectively [150]. In particular, the investigated temperatures exceed typical UGS conditions [66]. Gaucher et al. [46] observed an inhibiting effect of carbonates on the generation of hydrogen sulfide. In a consecutive study, Truche et al. [151] observed reactions even at lower temperatures and higher rates at alkaline conditions, concluding that acidic reservoirs could be better UHS candidates.

Apart from the pyrite-to-pyrrhotite reduction, the oxidation of hydrogen by hematite (Fe_2O_3) has been observed in laboratory experiments [107]. Sandstone samples containing hematite were exposed for over one month at a pressure of 120 bar and a temperature of 120 °C. Although hydrogen oxidation was not significant, remarkable changes in the mineral composition could be observed [107]. Besides the reduction/oxidation of iron-bearing minerals, further reactions were implied. Simulation studies of geochemical reactions with PHREEQC [26] indicated that K-feldspar, kaolinite, and dolomite could precipitate, while quartz, illite, and calcite could dissolve [62]. Bo et al. [14] performed a similar simulation study and strengthened the assumption of calcite dissolution related to the introduction of hydrogen. The simulated calcite dissolution was also observed experimentally during the exposure of rock samples to a hydrogen atmosphere in autoclave experiments [122]. Focusing on the sealing capacity of the storage, beneficial effects of hydrogen have been stated. Within the simulation study of Hemme and van Berk [62], albitization of clay-rich rocks has been observed, typically yielding a reduction of porosity and thereby improving the sealing capacity.

Nevertheless, there are also experimental studies where no reactions were observed [6, 58], so that the presence of geochemical reactions caused by the injection of hydrogen in the subsurface is still controversial [60].

2.2. Numerical modeling of reactive transport processes in porous media

Mathematical models describing natural phenomena can be solved analytically only under substantial restrictions concerning initial and boundary conditions. However, in reality, the applications are more complex, and analytical approaches reach their limits. Nowadays, numerical methods are commonly used to model more complex systems. To solve these systems, an environment (simulator) has to be developed that manages numerical techniques such as discretization in space and time. This section explains the general mathematical model for transport in a two-phase multi-component system in porous media. Additionally, an introduction to its realization in numerical methods is presented, and subsequently, the open-source simulator DuMu^x used in the present study is briefly introduced.

2.2.1. Transport equation of two-phase multi-component flow in porous media

Many transport processes, such as heat or fluid flux, are typically modeled using the so-called advection-diffusion equation (Eq. 2.19). This continuity equation generally combines the pressure-driven advection and the species gradient-governed diffusion equations. Furthermore, the continuity equation holds an additional term for considering sources and sinks within the system.

$$\underbrace{\frac{\partial c}{\partial t}}_{\text{storage term}} = \underbrace{\nabla \cdot (D \nabla c)}_{\text{diffusive/dispersive term}} - \underbrace{\nabla \cdot (\mathbf{v} c)}_{\text{advective term}} + \underbrace{R}_{\text{source term}} \tag{2.19}$$

where c is the species, D is the diffusion coefficient, $\mathbf{v}$ is the velocity field, and R is the source term.

To adapt this formulation for two-phase multi-component flow in porous media on a continuum scale, some modifications are required. Firstly, the volume of the storage term is reduced to the pore volume. Next, the chemical species are present in all phases, introducing the sum over phases with respect to all terms (cf. Eq. 2.20).

$$\underbrace{\frac{\partial \phi \sum\limits_{\alpha=g,w} \varrho_\alpha c_\alpha^\kappa S_\alpha}{\partial t}}_{\text{storage term}} + \underbrace{\nabla \cdot \sum_{\alpha=g,w} \left(\varrho_\alpha c_\alpha^\kappa u_\alpha + J_\alpha^\kappa \right)}_{\text{advection/diffusion term}} = \underbrace{q^\kappa}_{\text{source term}} \tag{2.20}$$

where ϕ is the porosity, ϱ denotes the molar density in mol/m^3, c is the molar concentration, S is the saturation of the phase, u is the Darcy velocity of the phase in m/s, J is the dispersion/diffusion term in mol/(m$^2 \cdot$ s), and q is the source term in mol/(m$^3 \cdot$ s). The subscript α indicates the phases water (w) or gas (g), and the superscript κ represents the fluid components.

Concerning the advection term, the mathematical model considers the macroscopic flow on a continuum scale within the validity of Darcy's Law:

$$u_\alpha = -\frac{K k_{r\alpha}}{\mu_\alpha} \nabla \left(p_\alpha - \rho_\alpha g \right), \quad \alpha = g, w \tag{2.21}$$

where u_α is the Darcy flow velocity in m/s, K is the absolute permeability in m^2, k_r is the relative permeability, μ is the dynamic viscosity in Pa $\cdot$ s, p is the phase pressure in Pa, ρ is the phase density in kg/m^3, and g denotes the gravitational acceleration in m/s^2.

In addition to the pressure gradient-driven advective flow, molecular diffusion and mechanical dispersion, influenced by the concentration gradient, are relevant flow processes that are accounted for in the diffusive/dispersive term:

$$J_\alpha^\kappa = -\varrho_\alpha \left(D_{\text{diff},\alpha}^\kappa + D_{\text{disp},\alpha}^\kappa \right) \nabla c_\alpha^\kappa, \quad \alpha = g, w \tag{2.22}$$

where $D_{\text{diff},\alpha}^\kappa$ is the effective diffusion coefficient in m^2/s and $D_{\text{disp},\alpha}^\kappa$ is the dispersion coefficient in m^2/s.

In the bulk, the molecular diffusion is often modeled by Fick's first law [37]. In porous media, the reduced volume due to available pore space and phase saturations and the complexity of pore structure has to be considered as well:

$$D_{\text{diff},\alpha}^\kappa = D_{\text{pm},\alpha}^\kappa = \phi \tau S_\alpha D_\alpha^\kappa \tag{2.23}$$

where τ is the tortuosity factor (value between zero and one) and D_α^κ is the bulk diffusion coefficient corresponding to the diffusion factor of Fick's law.

The impact of mechanical dispersion is as the molecular diffusion depending on the concentration gradient, but beyond this, also influenced by the velocity field [9, 130]:

$$D_{\text{disp},\alpha}^\kappa = \phi S_\alpha \left(\frac{v_\alpha v_\alpha^T}{\|v_\alpha\|} \left(a_L - a_T \right) + \|v_\alpha\| a_T \right) \tag{2.24}$$

where v is the true velocity field in m/s ($v_\alpha = u_\alpha / (\phi S_\alpha)$), and a_L and a_T are the longitudinal and transverse dispersivities in m.

For the two-phase relationship, the capillary pressure describes the pressure difference between the liquid and the gaseous phase:

$$p_c\left(S_w\right) = p_g - p_w \tag{2.25}$$

where p_c is the capillary pressure in Pa, p_g is the pressure of the gaseous phase in Pa, and p_w corresponds to the liquid phase in Pa. Frequently, generalized models such as the one proposed by Brooks and Corey [18] are used for determining saturation and capillary pressure functions:

$$p_c = p_e S_{we}^{-\frac{1}{\lambda}} \tag{2.26}$$

where p_e is the capillary entry pressure in Pa, S_{we} is the effective water saturation, and λ is the Brooks-Corey coefficient.

Following the model of Brooks and Corey [18], the relative permeabilities of the aqueous and gaseous phases are defined as follows:

$$k_{rw}\left(S_w\right) = S_{we}^{\frac{2+\lambda}{\lambda}} \tag{2.27}$$

$$k_{rg}\left(S_w\right) = \left(1 - S_{we}\right)^2 \left(1 - S_{we}^{\frac{2+\lambda}{\lambda}}\right) \tag{2.28}$$

Regarding the phase saturations, the effective liquid saturation depends on the residual saturations of the wetting (water) and non-wetting (gas) phases:

$$S_{we} = \frac{S_w - S_{wr}}{1 - S_{wr} - S_{gr}} \tag{2.29}$$

The mathematical model considers thermodynamic equilibrium for the distribution of the chemical components in the two phases. More precisely, the fugacity f of the components in the phases are identical.

$$f_g^\kappa = f_w^\kappa \tag{2.30}$$

With the assumption of Dalton's law (total pressure of a mixture is equal to the sum of the partial pressures of the individual components), the thermodynamic equilibrium in terms of molar concentrations c_α^κ, fugacity coefficient φ_α^κ in 1/Pa, and partial pressure p_α^κ in Pa can be expressed as follows:

$$c_g^\kappa \varphi_g^\kappa p_g^\kappa = c_w^\kappa \varphi_w^\kappa p_w^\kappa \tag{2.31}$$

To solve the system of equations, further requirements have to be fulfilled. It is obvious that the sum of the phase saturations has to sum up to unity:

$$\sum_\alpha S_\alpha = 1 \tag{2.32}$$

A similar requirement to the saturations has to be satisfied regarding the concentrations. Here, the sum of the concentrations of the individual components within one phase has to be unity.

$$\sum_\kappa c_\alpha^\kappa = 1, \quad \alpha = g, w \tag{2.33}$$

2.2.2. Discretization in time and space

In comparison to analytical models, numerical models require discrete locations in time and space where the solution of the system is investigated. The discretization allows the transformation of the mathematical model into a numerical model, where the solution is approximated at specific points in time and space. Based on the discretization, a system of nonlinear equations can be derived for each time step, which can be solved using an iterative method.

In the following, the temporal and spatial discretization schemes used in this study are briefly explained on the basis of the general transport equation:

$$\frac{\partial}{\partial t} u + \nabla \cdot f\,(u) = q(u) \tag{2.34}$$

where u is the vector containing the primary variables (unknowns), f encompasses the flux terms, and q is the source term.

2.2.2.1. Temporal discretization

The temporal discretization involves two steps. Firstly, approximating the time derivative (discretization scheme) followed by the time stepping defining the steps between the discrete points in time. The time derivative can be approximated by a first-order difference quotient:

$$\frac{\partial}{\partial t} u \approx \frac{u^{t+1} - u^{t}}{\Delta t} \tag{2.35}$$

Inserting Eq. 2.35 in the general transport equation (Eq. 2.34) two obvious options are possible to insert as a quotient: 1) forward ($u \to u^{t}$), which corresponds to the explicit Euler scheme or 2) backward ($u \to u^{t+1}$), yielding the implicit Euler approach. Although the implicit Euler subsequently requires the solution of a system of equations, it is unconditionally stable in comparison to the explicit Euler scheme [21]. Consequently, the implicit Euler approach is applied:

$$\frac{u^{t+1} - u^{t}}{\Delta t} + \nabla \cdot f\left(u^{t+1}\right) = q(u^{t+1}) \tag{2.36}$$

2.2.2.2. Spatial discretization

The discretization in space consists of two steps: firstly, selection of the discretization scheme and secondly, gridding, which partitions the simulation domain into subdomains (called elements or cells). Regarding discretization schemes, finite difference methods (FD), finite element methods (FE), and finite volume methods (FV) are common schemes, but mixed types such as control volume finite element (CVFE) methods also exist. In general, all schemes have their raison d’être, coming with pros and cons in factors such as convergence rate, mass conservation, and grid requirements.

In the field of reservoir engineering, early simulators commonly used the FD method, while the FV method has gained more popularity in recent years. This shift is due to the increasing computational power, better discretization of complex domains, and the mass conservation properties of the FV method.

2.2.2.2.1 Finite volume method

In the FV method, the space is discretized into control volumes where the discrete values are solved at their centers (cell-centered). Figure 2.18 provides an overview of relevant components of the cell-centered FV scheme for two neighboring cells, denoted as i and j. For each of these control volumes, the integral of the variable u is approximated using the following equation:

$$\frac{\partial}{\partial t}\int_{V_i} u \mathrm{d}V_i + \int_{V_i} \nabla \cdot f(u) \mathrm{d}V_i = \int_{V_i} q(u) \mathrm{d}V_i \tag{2.37}$$

By applying Gauss's theorem to the flux term (volume integral of the divergence is equal to the surface integral over the closed boundary surface), the equation can be rewritten as:

$$\frac{\partial}{\partial t}\int_{V_i} u \mathrm{d}V_i + \int_{\partial V_i} f(u) \cdot n \mathrm{d}A_i = \int_{V_i} q(u) \mathrm{d}V_i \tag{2.38}$$

where n is the unit normal vector on the corresponding control volume face σ, and A represents the total boundary area of the control volume faces.

Consequently, the changes due to the flux over all boundaries can be approximated by summing up the fluxes over the control volume faces to the neighboring elements:

$$\int_{\partial V_i} f(u) \cdot n \mathrm{d}A_i \approx \sum_{j=1}^{m} g_{ij}\left(u_i, u_j\right) \tag{2.39}$$

Here, the index i denotes the individual cell, j represents the neighboring control volume, and m is the number of neighboring cells of i. The function g_{ij} takes into account geometrical parameters such as the area of the face and

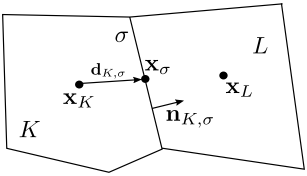

Figure 2.18: Two neighboring control volumes with the common face σ [86]

the distance between the centers. Additionally, it includes (averaged) fluid and rock properties like viscosity, density, porosity, and permeability.

As the quantities and unknowns are located in the center of the cell, they represent the average over the volume of the cell:

$$u_i = \frac{1}{V_i} \int_{V_i} u \mathrm{d}V_i \tag{2.40}$$

Similarly, this concept can be applied to the source/sink term to obtain the averaged quantity:

$$q(u_i) = \frac{1}{V_i} \int_{V_i} q(u) \mathrm{d}V_i \tag{2.41}$$

By dividing Eq. 2.38 by the volume of the cell V_i and inserting Eqs. 2.40 and 2.41, the mass conservation can be expressed as follows:

$$\frac{\partial}{\partial t} u_i + \frac{1}{V_i} \sum_{j=1}^{m} g_{ij} \left(u_i, u_j\right) = q(u_i) \tag{2.42}$$

In conclusion, Eq. 2.42 corresponds to the discrete cell-centered FV method formulation for the general transport equation. By inserting the already presented implicit Euler (Eq. 2.36) for temporal discretization, Eq. 2.42 yields for each time step and grid cell:

$$\frac{u_i^{t+1} - u_i^t}{\Delta t} + \frac{1}{V_i} \sum_{j=1}^{m} g_{ij} \left(u_i^{t+1}, u_j^{t+1}\right) = q(u_{t+1}) \tag{2.43}$$

or alternatively:

$$u_i^{t+1} = u_i^t + q(u_{t+1}) \Delta t - \frac{\Delta t}{V_i} \sum_{j=1}^{m} g_{ij} \left(u_i^{t+1}, u_j^{t+1}\right) \tag{2.44}$$

Generally, the FV scheme is well-suited for structured grids due to the straightforward arrangement of matrices, leading to a robust implementation. It is worth noting that sometimes unstructured grids are also suitable [88]. This scheme is globally and locally mass conservative, in contrast to the FD method, and less computationally expensive than FE method approaches [80].

2.2.2.2.2 Control volume finite element method

The CVFE method (also: box method) is a mix between the FV and FE methods possessing the advantages of both discretization methods. The idea is to discretize the domain into a primary FE and secondary FV mesh (cf. Figure 2.19).

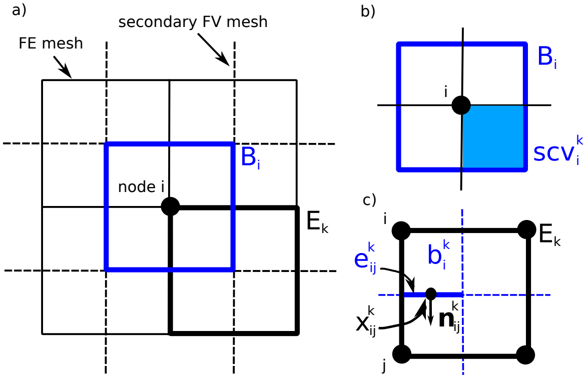

Figure 2.19: Overview of the different grids (a) and subgrids during the box method. (b) corresponds to the FV and (c) to FE mesh respectively [86]

The FE mesh consists of nodes i and their corresponding elements E_k. The FV mesh is built by connecting the midpoints and barycenters of neighboring elements, constructing a box around the node i. The combination of both grids leads to the creation of subcontrol volumes (scv). Additionally, the subcontrol volume b_i has faces to the subcontrol volume of neighboring box j, which is called the subcontrol volume face (scvf) e_{ij}^k.

Consequently, the balances of the fluxes over the subcontrol volume faces can be determined according to the FV method, whereby the fluxes over the boundaries at the integration point x_{ij}^k are obtained from the FE method.

In general, for FE methods, the transport problem can be expressed in its weak formulation as follows:

$$f(u) = \int_\Omega \frac{\partial u}{\partial t} \mathrm{d}\Omega + \int_\Omega \nabla \cdot F(u) \mathrm{d}\Omega - \int_\Omega q \mathrm{d}\Omega = 0 \tag{2.45}$$

where u are the unknowns (primary variables), Ω is the domain, F encompasses the flux terms, and g represents the source/sink term.

The unknowns can be interpolated in the finite elements by defining ansatz/basis functions N_i^k according to Lagrange:

$$u(\mathcal{X}) \approx \tilde{u}(\mathcal{X}) = \sum_i N_i(\mathcal{X})\tilde{u}_i \tag{2.46}$$

where $\tilde{u}$ is the approximate solution at an arbitrary spatial point $\mathcal{X}$ in the domain, and N_i is the ansatz function which is linear independent among themselves ($\sum_i N_i = 1$). However, the differential equation is not exactly fulfilled; moreover, a residual ε is created:

$$f(u) = 0 \rightarrow f(\tilde{u}) = \varepsilon \tag{2.47}$$

Next, weighting functions are introduced, which are multiplied by the residual. The aim is that the residual disappears in the entire domain:

$$\int_\Omega W_j \varepsilon \mathrm{d}\Omega \overset{!}{=} 0 \tag{2.48}$$

In analogy to the ansatz functions, the weighting functions are also linear independently ($\sum_i W_i = 1$). By replacing the unknowns u by approximated unknown $\tilde{u}$ (Eq. 2.46) and inserting the weighting functions to vanish ε (Eq. 2.48) in Eq. 2.45 yields:

$$\int_\Omega \frac{\partial \tilde{u}}{\partial t} W_j \mathrm{d}\Omega + \int_\Omega \nabla \cdot F(\tilde{u}) W_j \mathrm{d}\Omega - \int_\Omega q W_j \mathrm{d}\Omega \overset{!}{=} 0 \tag{2.49}$$

Depending on the selection of the weighting function, different schemes result. Choosing the ansatz and weighting function identically yields the standard Galerkin scheme. For the CVFE method, the weighting functions are defined as piece-wise constant functions over the FV mesh resulting in divergent definitions of weighting and ansatz function (Petrov-Galerkin scheme) [86, 160]:

$$N_i(\mathcal{X}) = \begin{cases} 1 & \mathcal{X} \in E_i \\ 0 & \mathcal{X} \notin E_i \end{cases} \quad \text{and} \quad W_j(\mathcal{X}) = \begin{cases} 1 & \mathcal{X} \in B_j \\ 0 & \mathcal{X} \notin B_j \end{cases} \tag{2.50}$$

where E_i and B_j correspond to the element of the FE and FV mesh.

Applying Green-Gaussian integral theorem for Eq. 2.49 yields:

$$\int_{B_j} \frac{\partial \tilde{u}}{\partial t} \mathrm{d}\Omega + \int_{\partial B_j} F(\tilde{u}) \cdot \mathrm{n} \mathrm{d}\Gamma_{B_j} - \int_{B_j} q \mathrm{d}\Omega \overset{!}{=} 0 \tag{2.51}$$

where Γ_{B_j} is the boundary region of the FV box B_j.

The storage term in Eq. 2.51 can be transformed as follows:

$$\int_{B_j} \frac{\partial \tilde{u}}{\partial t} \mathrm{d}\Omega = \frac{\mathrm{d}}{\mathrm{d}t} \int_{B_j} \sum_i \tilde{u}_i N_i \mathrm{d}\Omega = \sum_i \frac{\partial \tilde{u}_i}{\partial t} \int_{B_j} N_i \mathrm{d}\Omega \tag{2.52}$$

By introducing a mass lumping technique, the integral $M_{i,j} = \int_{B_j} N_i \mathrm{d}\Omega$ is replaced by the mass lump term $M_{i,j}^{\mathrm{lump}}$:

$$M_{i,j}^{\mathrm{lump}} = \begin{cases} |B_j| & j = i \\ 0 & j \neq i \end{cases} \tag{2.53}$$

where $|B_j|$ corresponds to the volume of the FV box B_j.

Combining Eqs. 2.51 and 2.53 yields:

$$|B_j| \frac{\partial \tilde{u}_i}{\partial t} + \int_{\partial B_j} F(\tilde{u}) \cdot \mathrm{n} \mathrm{d}\Gamma_{B_j} - Q_j = 0 \tag{2.54}$$

where Q_j represents the approximation of the integrated source/sink term.

In the last step, in analogy to the FV scheme, the time derivative can be replaced by the implicit Euler, resulting in the final equation, which has to be fulfilled for each box B_j and every timestep:

$$|B_j| \frac{\tilde{u}_i^{t+1} - \tilde{u}_i^t}{\Delta t} + \int_{\partial B_j} F(\tilde{u}^{t+1}) \cdot \mathrm{n} \mathrm{d}\Gamma_{B_j} - Q_j^{t+1} = 0 \tag{2.55}$$

As mentioned earlier, the resulting discretization scheme combines the advantages of FE and FV methods by having the gradient in every arbitrary spatial point in the domain (FE) and simultaneously achieving local mass conservation (FV). It is well-suited for unstructured grids, and local adaptation is possible. However, the grid requires certain conditions (e.g. conforming grid), which leads to a more complicated grid generation process compared to the standard FV or FD method. Additionally, it is more computationally expensive than FV or FD for simple problems in particular.

2.2.3. General structure and solving strategy

After defining the temporal and spatial discretization schemes, the unknowns can be determined in an iterative process that follows the workflow as depicted in Figure 2.20. The total number of unknowns corresponds to the number of primary variables multiplied by the number of grid cells. In the first step, the initial value of the unknowns is defined (initialization), followed by three interlaced loops: one for each time step, one for each Newton iteration, and one for each element.

```
1. main     2. time step     3. Newton     4. element

initialize
foreach time step
        foreach Newton iteration
                  foreach element
                            - calculate element
                              residual vector and
                              Jacobian matrix
                            - assemble into global
                              residual vector and
                             Jacobian matrix
                  endfor
                  solve linear system
                  update solution
                  check for Newton convergence
        endfor
        - adapt time step size,
          possibly redo with smaller step size
        - write result
endfor
finalize
```

Figure 2.20: Example of a solution scheme [86]

Beginning with the innermost loop, the vector of residuals and the Jacobian matrix are calculated for each grid cell. The Jacobian matrix contains all first-order derivatives in space, which are determined numerically. As a result, one obtains a linear equation system where the change in the solution Δu_n is solved:

$$J(u_n)\Delta u_n = -R(u_n) \tag{2.56}$$

where J is the Jacobian matrix, u_n is the vector containing the unknowns, and R is the residual vector.

Next, the new solution is obtained following the Newton's method:

$$u_{n+1} = u_n + \Delta u_n \tag{2.57}$$

where u_{n+1} corresponds to the next Newton iteration.

The convergence is achieved by comparing the relative and absolute errors of the consecutive solutions. After fulfilling the convergence criteria, the output is written out, and subsequently, the next time step is started until reaching the final simulation time.

2.2.4. Overview of the open-source simulator DuMu^x

Nowadays, a large variety of simulators is available for the numerical simulation of transport processes. In general, one distinguishes between commercial/proprietary (e.g. SLB Eclipse/E300, SLB Intersect, Rock Flow Dynamics tNavigator, and CMG STARS/GEM/IMEX) and open-source simulators (e.g. OpenPorousMedia (OPM) and DuMu^x). While the first group benefits from good numerical optimization and ease of use through a defined interface, open-source simulators are typically distributed as source code, which is less user-friendly due to its structure and limited interface for the user. However, they have an outstanding level of adaptability to specific needs, leading to high popularity within research.

Focusing on open-source simulators, a proper candidate to model reactive transport processes in porous media is DuMu^x. It has been in development by the University of Stuttgart (Institute of Modeling Hydraulic and Environmental Systems) since 2007 [38, 82]. It is based on DUNE [7] and is provided as an additional module to simulate fluid flow in porous media, including chemical reactions. DuMu^x stands for 'DUNE for Multi-{Phase, Component, Scale, Physics, ...} flow and transport in porous media'. The simulator comes with various implementations for a large field of applications (e.g. fuel-cell and soil evaporation processes). The core is the model that defines the type of involved transport processes and the number of phases and components. For this study, all simulations are inherited from the two-phase n-component porous medium flow model (2pnc). The primary variables are consequently one phase pressure, one phase saturation, and n-2 component concentrations. Furthermore, DuMu^x contains already preexisting fluid and solid systems describing the phase equilibrium and properties of the fluid and solid phases, respectively.

Regarding the simulation of UHS operations, the open-source simulator DuMu^x already showed its good potential to cover the transport process. The comparison with SLB Eclipse (E300), a representative of commercial reservoir simulators, showed congruent results for the pure transport [70] and pressure development during operations. Additionally, first implementations of biochemical reactions related to hydrogen were modeled in DuMu^x [31, 54, 55]. To date, the implementation of the particular biochemical model is unique and it has already shown excellent results during the application for an accompanying simulation for a pilot test [136].

Chapter 3

Extension and calibration of the bio-geo-reactive transport model for UHS

This chapter presents the mathematical model for bio-geo-reactive transport, along with the implementation and calibration of the associated processes in DuMu$^\text{x}$. Subsequently, the results of the first simulation runs on a field scale are presented, which were used to verify the model and its potential application for predicting UHS. The primary focus of the biochemical reactions was on methanation and sulfate reduction, while the geochemical aspects included the reduction of pyrite to pyrrhotite. However, it is essential to note that the mathematical model and its implementation were designed in a general form, allowing for easy adaptation to other relevant reactions and potential extensions.

This chapter contains work that was mainly developed and published [66, 71, 72, 74, 75, 96] during the EU research project "HyUSPRe - Hydrogen Underground Storage in Porous Reservoirs" funded from the Fuel Cells and Hydrogen 2 Joint Undertaking (now Clean Hydrogen Partnership) under grant agreement No 101006632. This Joint Undertaking receives support from the European Union's Horizon 2020 research and innovation programme, Hydrogen Europe and Hydrogen Europe Research.

3.1. Mathematical model of bio-geo-reactive transport processes

To model the unique processes during UHS, the transport equation for two phases (gas and water) with multiple components is considered. The continuity equation component-wise can be expressed as follows:

$$\frac{\partial\phi \sum\limits_{\alpha=g,w} \varrho_\alpha c_\alpha^\kappa S_\alpha}{\partial t} + \nabla \cdot \sum_{\alpha=g,w} \left(\varrho_\alpha c_\alpha^\kappa \frac{K k_{r\alpha}}{\mu_\alpha} \nabla \left(\rho_\alpha g - p_\alpha\right) - \varrho_\alpha D_{\mathrm{diff},\alpha}^\kappa \nabla c_\alpha^\kappa \right) = q^\kappa \tag{3.1}$$

where ϕ is the porosity, ϱ denotes the molar density in mol/m^3, c is the molar concentration, S is the saturation of the phase α, K is the absolute permeability in m^2, k_r is the relative permeability, μ is the phase's dynamic viscosity in Pa $\cdot$ s, ρ is the phase's density in kg/m^3, g is the gravitational acceleration in m/s^2, D_{diff} is the diffusion coefficient in m^2/s, and q is the source term in mol/(m^3 $\cdot$ s). The subscript α indicates the phases water (w) and gas (g), and the superscript κ represents the fluid components.

In comparison to Eq. 2.20, the contribution of mechanical dispersion is neglected in this study as the current implementation in DuMu$^\mathrm{x}$ does not allow the consideration of this process in the used discretization scheme (FV). Additionally, the porosity within the storage term is time-dependent as the pore space is dynamic over time due to reactions with the solid phase. Since the solid phase is assumed to be immobile, the material balance for the solid phase can be expressed as follows:

$$\varrho^{\kappa_s} \frac{\partial \phi_s^{\kappa_s}}{\partial t} = q^{\kappa_s} \tag{3.2}$$

where ϱ^{κ_s} denotes the molar density of the solid component κ_s in mol/m^3, $\phi_s^{\kappa_s}$ is the volume fraction of the solid component, and q corresponds to the source term in mol/(m^3 $\cdot$ s).

Similar to the sum of saturations (Eq. 2.32) and concentrations (Eq. 2.33), the volume fractions and the porosity have to sum up to unity:

$$\phi + \phi_s^{\mathrm{inert}} + \sum_{\kappa_s} \phi_s^{\kappa_s} = 1 \quad \text{or} \quad \phi = \phi_0 - \sum_{\kappa_s} \phi_s^{\kappa_s} \tag{3.3}$$

where ϕ_s^{inert} corresponds to the volume fraction of the inert mineral, and ϕ_0 corresponds to the maximum porosity ($\phi_0 = 1 - \phi_s^{\mathrm{inert}}$).

The source term permits the introduction of artificial sources and sinks in the domain. In the first place, this term is used to implement the bio- and geochemical reactions, but also the operation by a well is considered within this term. Consequently, it can be expressed by the following equations:
For fluid components κ:

$$q^{\kappa} = q^{\kappa}_{\text{bio}} + q^{\kappa}_{\text{geo}} + q^{\kappa}_{\text{well}} \tag{3.4}$$

For solid components κ_s:

$$q^{\kappa_s} = q^{\kappa_s}_{\text{geo}} \tag{3.5}$$

where q^{κ}_{bio} is the biochemical source in $\text{mol}/(\text{s} \cdot \text{m}^3)$, q^{κ}_{geo} is the geochemical source in $\text{mol}/(\text{s} \cdot \text{m}^3)$, and q^{κ}_{well} is the source due to the operation of the well in $\text{mol}/(\text{s} \cdot \text{m}^3)$.

3.1.1. Biochemical reactions

To consider the presence and activity of microorganisms, the interdependent growth and conversion are modeled. In general, the mathematical model of the biochemical reactions relies on the work of Hagemann [54]; however, changes in the implementation in DuMu$^\text{x}$ are performed within this study. Accordingly, the dynamic size of the microorganisms' population is governed by the continuous growth and decay of individuals:

$$\frac{\partial (n S_w \phi)}{\partial t} = \left(\psi^{\text{growth}} - \psi^{\text{decay}}\right) \cdot n \cdot S_w \cdot \phi \tag{3.6}$$

where n is the number of microbes in $1/\text{m}^3$, ψ^{growth} is the growth rate in 1/s, and ψ^{decay} is the decay rate in 1/s.

The dependency on water saturation is obvious as the microorganisms live only in the aqueous phase, where growth and decay can occur. Consequently, the growth depends on the substrates available in the aqueous phase. The growth itself is expressed by a double Monod model [102] where every substrate is expressed by a Monod term (see Section 2.1.2.1):

$$\psi^{\text{growth}} = \psi^{\text{growth}}_{\max} \left(\frac{c_w^{S1}}{\alpha^{S1} + c_w^{S1}}\right) \left(\frac{c_w^{S2}}{\alpha^{S2} + c_w^{S2}}\right) \tag{3.7}$$

where $\psi_{\max}^{\text{growth}}$ is the maximum growth rate in 1/s, c_w^S is the molar concentration of substrate S (e.g. H_2, CO_2) in the aqueous phase , and α^S is the half velocity constant.

The continuous decay of individuals depends on the number of microbes present. Generally said, the higher the microbial density, the higher the decay. Consequently, the decay is defined as follows:

$$\psi^{\text{decay}} = bn \tag{3.8}$$

where b is the decay factor in m^3/s.

The growth of the microorganisms is governed by their metabolism, where the substrate is converted to extract the required energy. Hence, the conversion of substrates to products is controlled by the growth rate of the microbes. This conversion is reflected in the source term:

$$q_{\text{bio}}^{\kappa} = \phi \gamma_{\text{bio}}^{\kappa} \frac{\psi^{\text{growth}}}{Y} n S_w \tag{3.9}$$

where $\gamma_{\text{bio}}^{\kappa}$ is the stoichiometric coefficient of the reaction and Y is the yield factor in 1/mol. The yield factor defines the amount of mole converted per cell division, whereby the higher the yield, the lower the conversion.

This mathematical model can be implemented for every microbial species independently, while the only interaction of the species is the conceivable share of substrates (substrate-limited model).

3.1.2. Geochemical reactions

Interactions between the fluid and solid phases can have various impacts on the storage process. Changes in fluid composition and alterations in petrophysical properties are the main concerns regarding UHS. To consider geochemical reactions, the changes in the phase composition are coupled with the source term. As mentioned earlier (see Subsection 2.1.3.1), geochemical reactions are typically modeled with 1) kinetic or 2) equilibrium models. In the present study, kinetic models are the focus, although the implementation allows an interface for equilibrium models in analogy to the kinetic models. A general formulation for kinetic models can be expressed as follows [84]:

$$q_{\text{geo}}^{\kappa} = \gamma_{\text{geo}}^{\kappa} \left(A_s^{r_s} k \left(1 - \frac{Q_m}{K_m} \right)^{\theta} \right) \phi_s^{r_s} \tag{3.10}$$

where γ_{geo} is the stoichiometric coefficient of component κ, $A_s^{r_s}$ is the reactive specific surface area of the reactive mineral r_s in $\mathrm{m}^2/\mathrm{m}^3$, k is the rate constant in $\mathrm{mol}/(\mathrm{s} \cdot \mathrm{m}^2)$, Q_m and K_m are mass coefficients, θ is a tuning parameter, and $\phi_s^{r_s}$ is the solid reactant's volume fraction.

The dissolution and precipitation of minerals result in changes in porosity and permeability. The variation in porosity is accounted for in Equation 3.3. To represent alterations in permeability, the Kozeny-Carman model [23, 83] is utilized:

$$K(\phi) = K_0 \left(\frac{1 - \phi_0}{1 - \phi} \right)^2 \left(\frac{\phi}{\phi_0} \right)^3 \tag{3.11}$$

where K_0 and ϕ_0 are the reference permeability and porosity, respectively. In general, small changes in porosity already lead to a significant change in permeability.

3.2. Realization of bio-geo-reactive transport model in DuMu$^\mathsf{x}$

The developed mathematical model was subsequently integrated into the open-source simulator DuMu$^\mathsf{x}$. The primary objective was to expand the existing `2pnc` model [54] by incorporating bio- and geochemical reactions (`2pncbiogeo`) and subsequently calibrating the model based on empirical data. Significant improvements were made to the fluid system, solid system, and the implementation of three reactions. The extensions and modifications in DuMu$^\mathsf{x}$ are depicted in Figure 3.1. The modified DuMu$^\mathsf{x}$ source code is available as an additional module in the GitLab repository [67] (persistent version [65]). This facilitates better code maintenance and distribution.

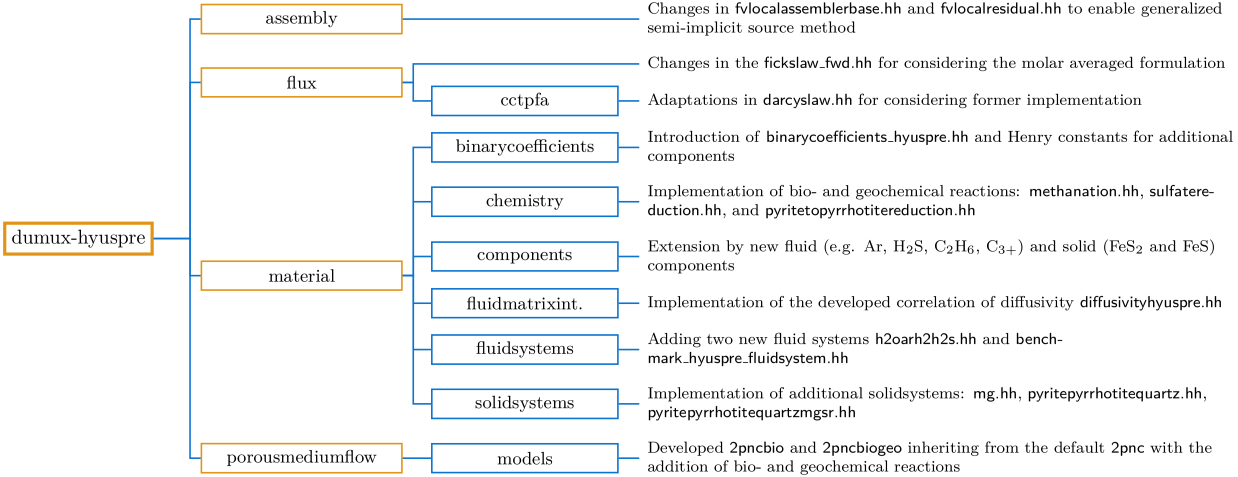

Changes in fvlocalassemblerbase.hh and fvlocalresidual.hh to enable generalized semi-implicit source method

Changes in the fickslaw_fwd.hh for considering the molar averaged formulation

Adaptations in darcyslaw.hh for considering former implementation

Introduction of binarycoefficients_hyuspre.hh and Henry constants for additional components

Implementation of bio- and geochemical reactions: methanation.hh, sulfatereduction.hh, and pyritetopyrrhotitereduction.hh

Extension by new fluid (e.g. Ar, H_2S, C_2H_6, C_{3+}) and solid (FeS_2 and FeS) components

Implementation of the developed correlation of diffusivity diffusivityhyuspre.hh

Adding two new fluid systems h2oarh2h2s.hh and benchmark_hyuspre_fluidsystem.hh

Implementation of additional solidsystems: mg.hh, pyritepyrrhotitequartz.hh, pyritepyrrhotitequartzmgsr.hh

Developed 2pncbio and 2pncbiogeo inheriting from the default 2pnc with the addition of bio- and geochemical reactions

Figure 3.1: Extensions and adaptations in comparison to the initial DuMu^x structure [86]

3.2.1. Implementation of bio-geo-reactive transport model

Focusing on the transport in porous media coupled with reactions, the default two-phase n-component model (2pnc) was extended. Two new models (2pncbio and 2pncbiogeo) were introduced. Contrary to the previous implementation of bio-reactive transport [54], the new versions inherit from the default 2pnc model to optimize code length, structure, and maintenance effort. In analogy to the compositional model, biochemical and biogeochemical models were introduced with changes in iofields.hh, localresidual.hh, model.hh, and volumevariables.hh. The changes led to the extension of the primary variables and the consideration of spatial parameters as well as output. For each reactive solid component, the number of primary variables (volume fraction) is extended by one. In addition, the pseudo components representing the microorganisms are considered as (immobile) solid components in the current implementation. However, the microbial density is the corresponding primary variable instead of the volume fraction. For considering the full extension by two reactive solid components and two microorganisms, the primary variables are extended by four.

3.2.2. Implementation of fluid model, solid system, and chemical reactions

In this study, a new fluid system was introduced. The fluid model (benchmark_hyuspre_fluidsystem.hh) encompasses two phases, gas and water, each comprising nine components: water (H_2O), methane (CH_4), hydrogen (H_2), carbon dioxide (CO_2), ethane (C_2H_6), a pseudo component (C_{3+}), nitrogen (N_2), sulfate (SO_4^{2-}), and hydrogen sulfide (H_2S). Phase equilibria are determined by a combination of Raoult's law and Henry's law [63], accounting for vaporization and dissolution in the phases. To calculate the density of the gas phase, the commonly used Peng-Robinson Equation of State (EoS) [116] is employed. The effects of temperature and pressure on the fluid mixture's viscosity are modeled using two correlations. Firstly, the full extended form of Stiel and Thodos [134] is used to determine low-pressure viscosity. Additionally, the Lohrenz et al. [91] correlation is employed to compute corrected high-pressure viscosity (cf. Figure 2.4).

In the solid system (`pyritepyrrhotitequartzmgsr.hh`), three solid components are taken into account: pyrite (FeS_2), pyrrhotite (FeS), and an inert component, quartz (SiO_2). The implementation of the solid phase draws partially from the work conducted by Hommel [76]. In this study, it is assumed that the rock is incompressible, and alterations in the volume fractions of the reactive minerals, as well as porosity, are solely a result of geochemical reactions. In the context of the methanation and sulfate reduction processes, microorganisms are integrated into the solid system as pseudo components, denoted as MG (for methanogens) and SR (for sulfate-reducing bacteria), respectively. Varying implementations, where only the geochemical or the biochemical components are considered, are also available (`mg.hh`, `pyritepyrrhotitequartz.hh`).

The reactions were realized as additional classes in the chemistry directory providing source-modifying reaction methods. For the biochemical reactions, the sulfate reduction (`sulfatereduction.hh`) and methanation (`methanation.hh`) are available, containing the relevant reactions and growth parameters (see Section 3.3.2). For the geochemical reaction of pyrite-to-pyrrhotite reduction, the reaction kinetics are available in the class `pyritetopyrrhotitereduction.hh`.

3.3. Calibration of simulation model based on laboratory investigations

To ensure the reliability of the numerical simulations, the model was calibrated using experimental data. In the context of gas-gas mixing, recent experiments on the molecular diffusion of a binary system, specifically methane-hydrogen, were used. Correlations based on the experimental results were developed and subsequently integrated into DuMu^x. The simulator was afterwards employed to replicate these experiments. Additionally, to model the biochemical reactions, static growth experiments were reproduced to obtain growth parameters in a matching procedure. Finally, the pyrite-to-pyrrhotite reduction was empirically modeled based on reactor experiments from literature to calibrate the developed model.

3.3.1. Calibration of gas-gas diffusion process for a hydrogen-methane binary system at underground gas storage conditions

To calibrate the process of molecular diffusion, recent experiments conducted by Michelsen et al. [95] were used to build correlations and subsequently implement them into DuMu$^{\mathrm{x}}$. Afterwards, the developed model was employed to verify the implementation by reproducing the experiments. This section corresponds to a large extent to the work published in Hogeweg et al. [72].

As introduced in Section 2.1.1.2, the process of molecular diffusion originates from the general tendency of balancing concentration differences caused by the Brownian motion of the molecules. Fick [37] developed a model describing this concentration gradient-driven flux, which is known as Fick's first law:

$$J_D^\kappa = -\rho D^\kappa \nabla c_g^\kappa \tag{3.12}$$

where J_D^κ is the diffusive flux of component κ in $\mathrm{mol}/\left(\mathrm{m}^2 \cdot \mathrm{s}\right)$, ρ is the molar density in $\mathrm{mol/m^3}$, D^κ is the diffusion coefficient in $\mathrm{m^2/s}$, and ∇c_g^κ the concentration gradient (mole fraction) in the gaseous phase in $1/\mathrm{m}$.

In the simplest case, a binary system composed of two components can be considered. Here, it is evident that each component's flux must be balanced to conserve the material balance [10]:

$$\sum_\kappa J_D^\kappa = 0 \tag{3.13}$$

Fulfilling this condition, the diffusion coefficients of both components have to be identical:

$$D^{\mathrm{A}} = D^{\mathrm{B}} = D^{\mathrm{AB}} \tag{3.14}$$

A recent approach of measuring bulk diffusion coefficients at higher temperatures ($T = 19.4\,°\mathrm{C}$ to $59.7\,°\mathrm{C}$) and pressures ($p = 90\,\mathrm{bar}$ to $147\,\mathrm{bar}$) for the binary system methane-carbon dioxide was shown in [53], where diffusion coefficients in the range of $1.46 \cdot 10^{-8}\,\mathrm{m^2/s}$ to $3.7 \cdot 10^{-8}\,\mathrm{m^2/s}$ were observed. To estimate gas-gas diffusion coefficients, numerous correlations (e.g. Fuller's method [41] or Wilke's method [159]) have been developed in the past, whereby they are typically limited to low pressure and temperature ranges. Therefore, these models have limited applicability to the conditions during the storage of gases in the porous subsurface. Furthermore, diffusion can only occur within the pores in porous media and is therefore decelerated compared to the open flow due to the reduced space for exchange. For the one-dimensional system, the flow pathway through the rock is extended due to the tortuosity of the pore structure. This reduction can be expressed as follows [61]:

$$D_{\mathrm{pm}}^{\mathrm{AB}} = \phi \tau S_g D_{\mathrm{bulk}}^{\mathrm{AB}} \tag{3.15}$$

where $D_{\mathrm{pm}}^{\mathrm{AB}}$ is the effective binary diffusion coefficient of the porous media in m^2/s, ϕ is the porosity, τ is the tortuosity factor of the porous medium, S_g is the gas saturation, and $D_{\mathrm{bulk}}^{\mathrm{AB}}$ is the binary diffusion coefficient for the bulk medium in m^2/s.

So far, only a few measurements of effective diffusion coefficients in porous media have been conducted. Pandey et al. [109] and Chen et al. [27] performed steady-state and unsteady-state measurements at pressures up to 5 bar. Pandey et al. [109] used a steady-state method for dry samples, while an unsteady-state measurement method was selected for saturated and low-permeable samples. Here, effective diffusion coefficients for the binary system helium-nitrogen in the range of $2.14 \cdot 10^{-6}\,\mathrm{m}^2/\mathrm{s}$ to $1.19 \cdot 10^{-4}\,\mathrm{m}^2/\mathrm{s}$ (steady-state method) and $1.67 \cdot 10^{-8}\,\mathrm{m}^2/\mathrm{s}$ to $1.88 \cdot 10^{-5}\,\mathrm{m}^2/\mathrm{s}$ (unsteady-state method) were measured. Chen et al. [27] observed higher diffusion coefficients ($2.59 \cdot 10^{-5}\,\mathrm{m}^2/\mathrm{s}$ to $2.00 \cdot 10^{-3}\,\mathrm{m}^2/\mathrm{s}$) for methane-nitrogen at a pressure of $p = 1\,\mathrm{bar}$ and a temperature of $T = 35\,^{\circ}\mathrm{C}$.

Overall, the lack of experimental data and insufficient characterization of molecular diffusion at storage conditions leads to a knowledge gap, which is addressed in this work. To close this gap, recently conducted and analyzed experiments of effective diffusion for the binary system hydrogen-methane [97, 98] were used to develop proper correlations in the following form of Eq. 3.16:

$$D_{\mathrm{pm}}^{\mathrm{AB}} = \phi \tau \left(\phi, S_g, K\right) S_g D_{\mathrm{bulk}}^{\mathrm{AB}} \left(p, T\right) \tag{3.16}$$

where p corresponds to the pore pressure in bar, T is the temperature in K, and K is the effective permeability in m^2.

Subsequently, the correlation was implemented in DuMu^x, and the experimental observations were reproduced to calibrate the numerical model with respect to the forecast of UHS scenarios.

3.3.1.1. Experimental procedure of measuring gas-gas molecular diffusion in the laboratory

To measure molecular diffusion, Michelsen et al. [96, 98] used a binary diffusion setup, which was adapted from the work of Wicke and Kallenbach [158]. The measurements were performed with a quasi-stationary one-chamber method. The main component of the setup is a core holder, which is developed for rock samples with a length of up to 6 cm and a diameter of 3 cm, as depicted in Figure 3.2. The core holder, also known as the diffusion cell, consists of a hollow cylinder that contains a rock sample, one gas distribution element, one gas injection element, and two end pieces. The hollow cylinder is a large chamber on one side of the rock sample. It must have a volume multiple of the rock sample's pore volume. Before placing these components into the diffusion cell, they are inserted into a Viton sleeve. On the other side of the rock sample is the gas distribution element with an inlet and an outlet. Before the experiment, the water-filled annulus surrounding the Viton sleeve is slowly pressurized to build up a certain radial pressure on the core specimen. This radial pressure is greater than the measurement pore pressure of the gas. Simultaneously, the diffusion cell is filled and pressurized with hydrogen step-wise along with the radial pressure. During the experiment, methane is injected into the diffusion cell through the inlet, controlled by a syringe pump that drives a floating piston chamber. A backpressure regulator is installed at the target outlet to maintain a constant pressure in the diffusion cell during the measurement. A gas chromatograph, which continuously analyses the gas composition, is located behind the backpressure regulator. The injection is continued until a clear trend (straight line) in the gas composition is identi-

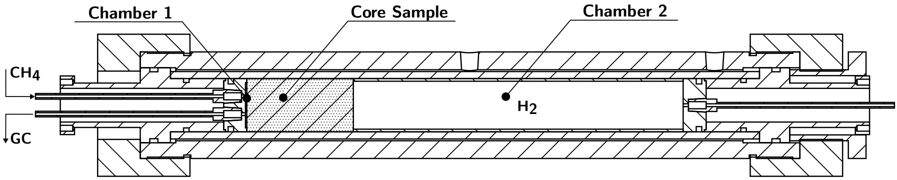

Figure 3.2: Schematic representation of the diffusion cell

fiable. The effective diffusion coefficients were determined by matching the measurement results with a one-dimensional numerical simulation model implemented in COMSOL Multiphysics. A more extensive description can be found in [96, 98], and an example of the COMSOL simulation can be found in the repository [73].

3.3.1.2. Development of a correlation for molecular diffusion in porous media

To develop a mathematical model characterizing the diffusive flux of the binary system hydrogen-methane in the subsurface, three data sets [95] of experiments were investigated. The first set (see Table 3.1) contains various samples from actual storage formations (samples B to H) at the reference temperature and pore pressure conditions of $T = 40\,°\mathrm{C}$ and $p = 100\,\mathrm{bar}$ isolating the dependency of the petrophysical properties of the porous media. The second set (cf. Table 3.2) is composed of the measurements performed on the reference sample A (Bentheimer Sandstone) at various thermodynamic conditions to establish the dependency of the diffusion coefficient on pressure and temperature. A final extended data set was used to validate and assess the accuracy of the developed correlation (see Tables 3.3 and 3.4).

Overall, the laboratory measurements show a dependency on the thermodynamic conditions and the influence of the petrophysical properties on the strength of the molecular diffusion. The experimental observations generally indicate that the effective diffusion coefficient decreases with increasing temperature. In low-pressure ranges ($< 75\,\mathrm{bar}$), the coefficient decreases with increasing pressure, followed by an increasing trend for higher pressures. Higher porosities, low water saturations, and higher permeabilities show a higher effective molecular diffusion coefficient.

Table 3.1: Data Set 1 - Measurements at T = 40 °C and p = 100 bar

Sample	Porosity [-]	Permeability [mD]	Gas sat. [-]	Eff. diff. coeff. [m^2/s]
A	0.247	2500	0.4	$5.00\cdot10^{-9}$
A	0.247	2500	0.6	$4.00\cdot10^{-8}$
A	0.247	2500	1	$1.10\cdot10^{-7}$
B	0.299	71	1	$7.00\cdot10^{-8}$
C	0.268	157.6	1	$6.00\cdot10^{-8}$
D	0.317	718.6	1	$2.30\cdot10^{-7}$
E	0.199	23.6	1	$2.60\cdot10^{-8}$
F	0.321	288.2	1	$1.20\cdot10^{-7}$
G	0.274	263.1	1	$9.80\cdot10^{-8}$
H	0.176	17.2	1	$1.80\cdot10^{-8}$
I	0.210	105	1	$3.70\cdot10^{-8}$

Table 3.2: Data Set 2 - Measurements with constant petrophysical properties ($\phi = 0.247$, k = 2500 mD, and $S_g = 1$)

Sample	Temperature [°C]	Pressure [bar]	eff. Diff. Coeff. [m^2/s]
A	40	20	$1.55\cdot10^{-7}$
A	40	20	$1.64\cdot10^{-7}$
A	40	50	$1.20\cdot10^{-7}$
A	40	75	$9.00\cdot10^{-8}$
A	40	100	$1.10\cdot10^{-7}$
A	40	125	$1.26\cdot10^{-7}$
A	40	150	$1.55\cdot10^{-7}$
A	40	150	$1.60\cdot10^{-7}$
A	40	175	$1.72\cdot10^{-7}$
A	40	200	$2.00\cdot10^{-7}$
A	25	100	$1.20\cdot10^{-7}$
A	55	100	$1.00\cdot10^{-7}$
A	70	100	$9.60\cdot10^{-8}$
A	85	100	$9.50\cdot10^{-8}$
A	100	100	$9.30\cdot10^{-8}$
A	85	150	$1.49\cdot10^{-7}$
A	40	10	$3.71\cdot10^{-7}$
A	40	10	$3.70\cdot10^{-7}$

3.3.1.2.1 Modeling of the tortuosity factor representing the influence of the porous medium

In the first step, the dependency of the diffusion coefficient on the properties of the porous media was analyzed. Here, the data from Table 3.1 was used. The intention was to develop a correlation for the tortuosity factor in dependency of porosity, permeability, and gas saturation, as these parameters are typically already determined on investigations such as well logging, routine core analysis (RCAL), and operation history. A straightforward trial and error approach led to a satisfying result, as depicted in Figure 3.3. Merely one measurement point (sample D) deviates from the developed correlation. In this case, diverging pore connectivity and topology of the sample on pore scale could explain this deviation. The best match has the following form:

$$D_{\mathrm{pm}}^{\mathrm{AB}} = \phi^2 S_g^2 k_{\mathrm{eff}}^{1/5} \cdot 3.785 \cdot 10^{-4} \tag{3.17}$$

where $D_{\mathrm{pm}}^{\mathrm{AB}}$ is the binary diffusion coefficient between hydrogen and methane in m^2/s, ϕ is the porosity, S_g is the gas saturation, and k_{eff} is the effective permeability in m^2.

To isolate the tortuosity factor of the porous medium, the Fuller method [40, 41, 42] was selected due to its reported good accuracy at low pressures and temperatures to describe the bulk diffusion coefficient. Evaluating Fuller's method at $T = 40\,^\circ\mathrm{C}$ and $p = 10\,\mathrm{bar}$ ($D_{\mathrm{bulk}}^{\mathrm{AB}} = 2.1395 \cdot 10^{-6}\,\mathrm{m}^2/\mathrm{s}$) allowed

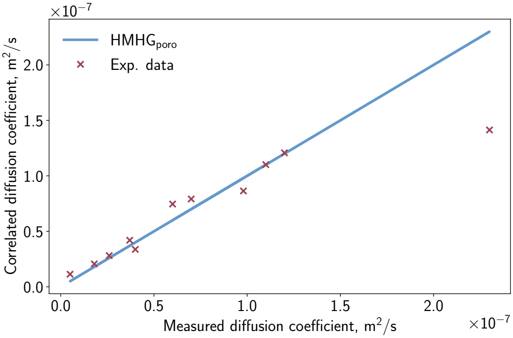

Figure 3.3: Developed correlation $\mathrm{HMHG}_{\mathrm{poro}}$ of the effective diffusion coefficient based on various rock samples varying in petrophysical properties and saturation

to determine the tortuosity factor of the Bentheimer sample ($\tau_A = 0.208$). In the general form, the first part of the correlation can be expressed as follows:

$$D_{\mathrm{pm}}^{\mathrm{AB}} = \phi S_g \tau D_{\mathrm{bulk}}^{\mathrm{AB}} \tag{3.18}$$

$$\mathrm{HMHG}_{\mathrm{poro}}: \quad \tau = \phi S_g k_{\mathrm{eff}}^{1/5} \cdot 176.916\,\mathrm{m}^{-2/5} \tag{3.19}$$

3.3.1.2.2 Modeling the impact of pressure and temperature on the process of molecular diffusion

A mathematical model to describe the bulk diffusion coefficient in dependency on pressure and temperature was developed based on the correlation for the tortuosity factor. Here, a second-degree (2x2y) polynomial regression of the second data set (see Table 3.2) was used to predict the effective diffusion coefficient (see Figure 3.4). The impact of the porous medium could be eliminated with Eqs. 3.18-3.19. The best fit for the bulk diffusion coefficients in dependency of temperature and pressure was achieved with the following coefficients:

$$\mathrm{HMHG}_{\mathrm{thermo}}: \; D_{\mathrm{bulk}}^{\mathrm{AB}}(T,p) = \beta_1 + \beta_2 T + \beta_3 p + \beta_4 T^2 + \beta_5 Tp + \beta_6 p^2 \tag{3.20}$$

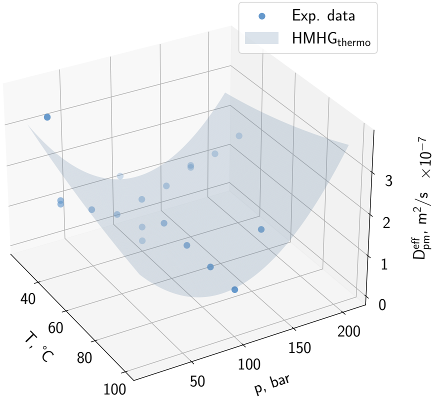

Figure 3.4: Effective diffusion coefficient as a function of pressure and temperature for the Bentheimer Sandstone sample (sample A)

$$\beta_1 = 3.610\,69 \cdot 10^{-5}\,\mathrm{m^2/s} \wedge \beta_2 = -1.466\,72 \cdot 10^{-7}\,\mathrm{m^2/s/K} \tag{3.21}$$

$$\beta_3 = -1.748\,42 \cdot 10^{-12}\,\mathrm{m^2/s/Pa} \wedge \beta_4 = 1.677\,93 \cdot 10^{-10}\,\mathrm{m^2/s/K^2} \tag{3.22}$$

$$\beta_5 = 2.951\,55 \cdot 10^{-15}\,\mathrm{m^2/s/K/Pa} \wedge \beta_6 = 3.718\,63 \cdot 10^{-20}\,\mathrm{m^2/s/Pa^2} \tag{3.23}$$

Afterwards, the developed correlations (Eqs. 3.19, 3.20-3.23) were merged into the final form of:

$$D_{\mathrm{pm}}^{\mathrm{AB}} = \phi\tau\left(\phi, S_g, k\right) S_g D_{\mathrm{bulk}}^{\mathrm{AB}}\left(p, T\right) \tag{3.24}$$

in terms of the new correlation:

$$D_{\mathrm{pm}}^{\mathrm{AB}} = \phi \mathrm{HMHG}_{\mathrm{poro}}(\phi, S_g, k) S_g \mathrm{HMHG}_{\mathrm{thermo}}(p, T) \tag{3.25}$$

3.3.1.2.3 Comparison to existing correlations and estimation of relative error

The developed correlations (Eqs. 3.19, 3.20, and 3.25) were compared with existing models. Correlations for the tortuosity factor and the bulk diffusion coefficient were examined independently. Afterwards, the relative error of the developed and existing correlation sets was estimated and compared.

The difficulty of accurately measuring gas-gas bulk diffusion coefficients at higher temperatures and pressures leads to a limited number of correlations describing this parameter. A typical correlation is Fuller's method (cf. Eq. 3.26) [40, 41, 42], which shows good accuracies in the low-pressure range ($< 10\,\mathrm{bar}$) according to the literature [120]. An advantage of this correlation is the general formulation, which enables the prediction of various binary combinations of components:

$$D_{\mathrm{bulk}}^{\mathrm{AB}} = \frac{0.0143 T^{1.75}}{p M_{\mathrm{AB}}^{0.5} \left((\Sigma_v)_A^{1/3} + (\Sigma_v)_B^{1/3} \right)^2} \tag{3.26}$$

$$M_{\mathrm{AB}} = \frac{2}{\frac{1}{M_{\mathrm{A}}} + \frac{1}{M_{\mathrm{B}}}} \tag{3.27}$$

where $D_{\mathrm{bulk}}^{\mathrm{AB}}$ is the bulk binary diffusion coefficient in $\mathrm{m^2/s}$, T is the temperature in K, p is the pressure in Pa, M_{AB} is the harmonic mean of the molecular weight of components A and B in g/mol, and Σ_v is the atomic diffusion volume.

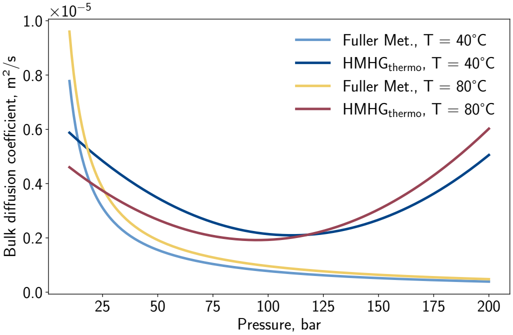

Figure 3.5: Comparison of bulk diffusion coefficients determined with Fuller's method and the proposed correlation as a function of pressure

Figure 3.5 depicts the trend of the bulk diffusion coefficient versus pressure according to Fuller's method and the developed correlation. While Fuller's method leads to a strongly monotonic decreasing diffusion coefficient with increasing pressure, the developed correlation leads to an initial decrease followed by an increasing diffusion coefficient. This yields consistent results at low-medium pressures (≈ 25 bar), but the deviation between both models grows with increasing pressure. Based on the experimental investigations and developed correlation, the bulk diffusion coefficients seem to be higher than expected. According to the theory [32, 156], the behavior as predicted by Fuller's method is more reasonable than the correlation in the present study. However, Guevara-Carrion et al. [53] described a similar trend as observed in the presented experiments. Guevara-Carrion et al. [53] concluded that this phenomenon is caused by the transition from a liquid-like to gas-like state within the supercritical region, which could also be applicable in the present study. Nevertheless, the measurement of the bulk diffusion coefficient in a similar experimental approach without a core specimen is recommended to determine the data point, which is currently based on Fuller's method experimentally (see Section 3.3.1.2.1).

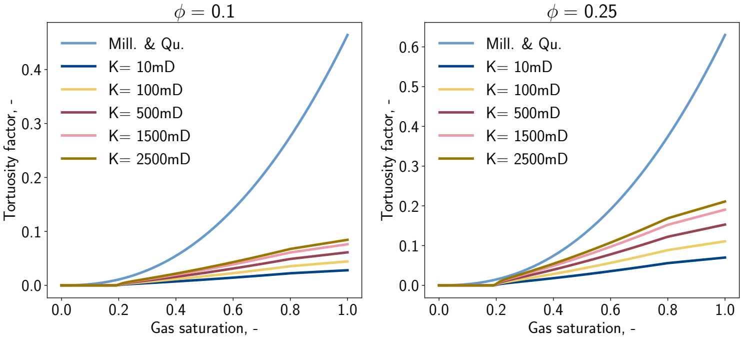

Figure 3.6: Comparison of tortuosity factor determined with Millington & Quirk and the proposed correlation as a function of gas saturation, porosity, and absolute permeability. To determine the impact of relative permeability, the Brooks-Corey model [18] is used, parameterized with $\mathrm{S_{wc}} = 0.2$ and $\lambda = 2$

The commonly used model of Millington and Quirk [99] was compared with the developed correlation for the tortuosity factor. The model of Millington & Quirk estimates the tortuosity factor of a porous medium based on its porosity and gas saturation (cf. Eq. 3.28). Figure 3.6 compares the developed correlation for two different porosities. Both correlations generally show an increasing tortuosity factor with increasing petrophysical properties and gas saturation. This is physically justified as the higher the tortuosity factor, the more it behaves as a bulk volume ($\tau_{\text{bulk}} = 1$). Furthermore, with increasing saturation, the deviation between both models increases so that at high gas saturations, the tortuosity factor in the correlation is approximately 3 to 4 times lower than the result of the model of Millington & Quirk.

$$\tau = \phi^{1/3} S_g^{7/3} \tag{3.28}$$

3.3.1.2.4 Overview of correlated effective diffusion coefficients and error analysis

Concerning the accuracy of the correlations, the correlated results of the proposed model (HMHG) and the established combination of Fuller's method and Millington & Quirk (FMQ) to the laboratory observations were compared. For the reference sample A, the comparison is depicted in Figure 3.7.

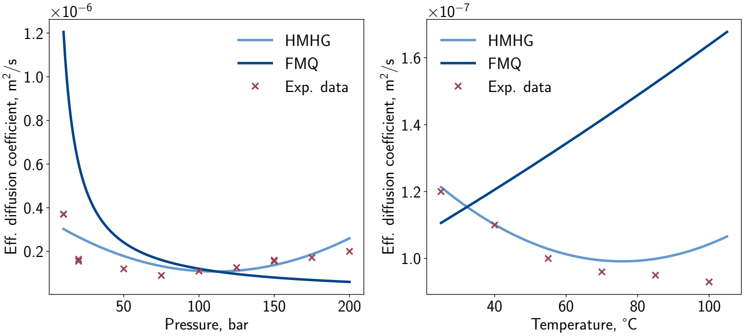

Figure 3.7: Comparison of correlated (model HMHG and FMQ) and measured effective diffusion coefficient of the porous media (sample A)

Regarding the pressure trend, the observations are analogous to the bulk diffusion as it is only scaled by the product of the porosity, gas saturation, and tortuosity factor of sample A. More interesting is the diverging trend of the diffusion coefficient with increasing temperatures. Here, the results of model FMQ show an increasing quasi-linear behavior, while the experimental observations indicate a decreasing trend. The general trend is reproduced by model HMHG, although the deviation between measured and correlated coefficients is increasing at high temperatures. As an additional parameter of the accuracy of the models, the relative error is determined:

$$\delta_{D_{\mathrm{pm}}^{\mathrm{AB}}} = \frac{D_{\mathrm{pm}}^{\mathrm{measured}} - D_{\mathrm{pm}}^{\mathrm{correlated}}}{D_{\mathrm{pm}}^{\mathrm{measured}}} \tag{3.29}$$

An overview of the corresponding results is listed in Tables 3.3 and 3.4. The suggested model shows good results mimicking and predicting the measured effective diffusion coefficients with relative errors of less than 50 %. Only four experiments showed higher relative errors for which the correlation shows insufficient accuracy. The high error with the saturated samples is subject to stronger uncertainties in the experimental procedure and, therefore, the relative error may not be representative. The remaining remarkable deviations were samples measured at the experimental matrix's higher boundaries and exceeding these conditions. Furthermore, the binary diffusion coefficient is overestimated for these cases; therefore, the coefficient is higher than observed. Regarding the significant deviation of 615 % for sample H, the temperature is

Table 3.3: Overview of the correlated diffusion coefficients - Model HMHG corresponds to the proposed correlation of this study, while model FMQ represents the combination of Fuller's method and Millington & Quirk

Sample	Thermodynamic		Petrophysical properties			Effective diffusion coefficient $D_{\mathrm{pm}}^{\mathrm{eff}}$, m^2/s			Relative error $\delta_{D_{\mathrm{pm}}^{\mathrm{AB}}}$, %	
	T, °C	p, bar	ϕ, -	k, mD	S_g, -	Lab.	HMHG	FMQ	HMHG	FMQ
A	40	50	0.247	2500	1	$1.20{\cdot}10^{-7}$	$1.79{\cdot}10^{-7}$	$2.41{\cdot}10^{-7}$	-48.90	-100.91
A	40	75	0.247	2500	1	$9.00{\cdot}10^{-8}$	$1.32{\cdot}10^{-7}$	$1.61{\cdot}10^{-7}$	-47.16	-78.59
A	40	100	0.247	2500	1	$1.10{\cdot}10^{-7}$	$1.10{\cdot}10^{-7}$	$1.21{\cdot}10^{-7}$	-0.12	-9.59
A	40	125	0.247	2500	1	$1.26{\cdot}10^{-7}$	$1.12{\cdot}10^{-7}$	$9.64{\cdot}10^{-8}$	11.31	23.46
A	40	150	0.247	2500	1	$1.55{\cdot}10^{-7}$	$1.37{\cdot}10^{-7}$	$8.04{\cdot}10^{-8}$	11.43	48.15
A	40	150	0.247	2500	1	$1.60{\cdot}10^{-7}$	$1.37{\cdot}10^{-7}$	$8.04{\cdot}10^{-8}$	14.19	49.77
A	40	175	0.247	2500	1	$1.72{\cdot}10^{-7}$	$1.87{\cdot}10^{-7}$	$6.89{\cdot}10^{-8}$	-8.58	59.95
A	40	200	0.247	2500	1	$2.00{\cdot}10^{-7}$	$2.60{\cdot}10^{-7}$	$6.03{\cdot}10^{-8}$	-30.08	69.86
A	25	100	0.247	2500	1	$1.20{\cdot}10^{-7}$	$1.21{\cdot}10^{-7}$	$1.11{\cdot}10^{-7}$	-1.10	7.81
A	55	100	0.247	2500	1	$1.00{\cdot}10^{-7}$	$1.03{\cdot}10^{-7}$	$1.31{\cdot}10^{-7}$	-2.84	-30.83
A	70	100	0.247	2500	1	$9.60{\cdot}10^{-8}$	$9.94{\cdot}10^{-8}$	$1.41{\cdot}10^{-7}$	-3.57	-47.37
A	85	100	0.247	2500	1	$9.50{\cdot}10^{-8}$	$9.99{\cdot}10^{-8}$	$1.52{\cdot}10^{-7}$	-5.16	-60.50
A	100	100	0.247	2500	1	$9.30{\cdot}10^{-8}$	$1.04{\cdot}10^{-7}$	$1.64{\cdot}10^{-7}$	-12.11	-76.16
A	85	150	0.247	2500	1	$1.49{\cdot}10^{-7}$	$1.61{\cdot}10^{-7}$	$1.02{\cdot}10^{-7}$	-8.22	31.78
A	40	10	0.247	2500	1	$3.71{\cdot}10^{-7}$	$3.02{\cdot}10^{-7}$	$1.21{\cdot}10^{-6}$	18.48	-224.93
A	40	10	0.247	2500	1	$3.70{\cdot}10^{-7}$	$3.02{\cdot}10^{-7}$	$1.21{\cdot}10^{-6}$	18.26	-225.80
A	40	20	0.247	2500	1	$1.55{\cdot}10^{-7}$	$2.66{\cdot}10^{-7}$	$6.03{\cdot}10^{-7}$	-71.46	-288.86
A	40	20	0.247	2500	1	$1.64{\cdot}10^{-7}$	$2.66{\cdot}10^{-7}$	$6.03{\cdot}10^{-7}$	-62.05	-267.52
A	40	100	0.247	2500	0.4	$5.00{\cdot}10^{-9}$	$1.14{\cdot}10^{-8}$	$5.68{\cdot}10^{-9}$	-127.10	85.79
A	40	100	0.247	2500	0.6	$4.00{\cdot}10^{-8}$	$3.37{\cdot}10^{-8}$	$2.20{\cdot}10^{-8}$	15.72	-339.23

Table 3.4: Overview of the correlated diffusion coefficients - Model HMHG corresponds to proposed correlation of this study, while model FMQ represents the combination of Fuller's method and Millington & Quirk

Sample	Thermodynamic		Petrophysical properties			Effective diffusion coefficient $D_{\text{pm}}^{\text{eff}}$, m^2/s			Relative error $\delta_{D_{\text{pm}}^{\text{AB}}}$, %	
	T, °C	p, bar	ϕ, -	k, mD	S_g, -	Lab.	HMHG	FMQ	HMHG	FMQ
B	40	100	0.299	71	1	$7.00{\cdot}10^{-8}$	$7.92{\cdot}10^{-8}$	$1.56{\cdot}10^{-7}$	-13.09	-122.17
B	50	106	0.299	71	1	$6.50{\cdot}10^{-8}$	$7.47{\cdot}10^{-8}$	$1.55{\cdot}10^{-7}$	-14.96	-138.49
C	40	100	0.299	157.6	1	$6.00{\cdot}10^{-8}$	$9.29{\cdot}10^{-8}$	$1.56{\cdot}10^{-7}$	-54.75	-159.20
C	25	53.5	0.268	157.6	1	$1.10{\cdot}10^{-7}$	$1.30{\cdot}10^{-7}$	$2.31{\cdot}10^{-7}$	-18.56	-109.58
D	40	100	0.317	718.6	1	$2.30{\cdot}10^{-7}$	$1.41{\cdot}10^{-7}$	$1.68{\cdot}10^{-7}$	38.54	26.90
D	45	88.3	0.317	718.6	1	$2.00{\cdot}10^{-7}$	$1.46{\cdot}10^{-7}$	$1.96{\cdot}10^{-7}$	26.93	2.12
E	40	100	0.199	23.6	1	$2.60{\cdot}10^{-8}$	$2.81{\cdot}10^{-8}$	$9.04{\cdot}10^{-8}$	-8.21	-247.58
E	107	140.5	0.199	23.6	1	$1.70{\cdot}10^{-8}$	$4.18{\cdot}10^{-8}$	$9.03{\cdot}10^{-8}$	-145.67	-431.21
F	40	100	0.321	288.2	1	$1.20{\cdot}10^{-7}$	$1.21{\cdot}10^{-7}$	$1.71{\cdot}10^{-7}$	-0.62	-42.47
F	86	116.5	0.321	288.2	1	$1.10{\cdot}10^{-7}$	$1.21{\cdot}10^{-7}$	$1.87{\cdot}10^{-7}$	-9.62	-69.57
G	40	100	0.274	27.4	1	$9.80{\cdot}10^{-8}$	$5.50{\cdot}10^{-8}$	$1.38{\cdot}10^{-7}$	43.93	-41.26
G	96	287.3	0.274	27.4	1	$1.70{\cdot}10^{-7}$	$4.27{\cdot}10^{-7}$	$6.43{\cdot}10^{-8}$	-151.15	62.19
H	40	100	0.176	17.2	1	$1.80{\cdot}10^{-8}$	$2.07{\cdot}10^{-8}$	$7.67{\cdot}10^{-8}$	-14.76	-326.23
H	92	203	0.176	17.2	1	$9.00{\cdot}10^{-9}$	$6.44{\cdot}10^{-8}$	$4.95{\cdot}10^{-8}$	-615.39	-449.46
I[1]	25	40	0.21	105	1	$1.15{\cdot}10^{-7}$	$8.77{\cdot}10^{-8}$	$2.23{\cdot}10^{-7}$	23.73	-93.70
I[1]	25	60	0.21	105	1	$6.50{\cdot}10^{-8}$	$6.81{\cdot}10^{-8}$	$1.49{\cdot}10^{-7}$	-4.78	-128.46
I[1]	40	100	0.21	105	1	$3.70{\cdot}10^{-8}$	$4.22{\cdot}10^{-8}$	$9.71{\cdot}10^{-8}$	-14.13	-162.41

---

[1] Berea sandstone sample

located at the upper boundary, the pressure exceeds the upper limit, and the permeability is the lowest of the entire measurement series. In this region, the model reaches its limitations. In these circumstances, additional experiments could lead to improved tuning within this region. Nevertheless, the correlation shows promising results for typical storage conditions within the European Union regarding temperature, pressure, and petrophysical properties.

In comparison to the developed correlation, model FMQ indicates higher relative errors. Here, deviations of more than 100 % can be regularly observed. Therefore, the developed correlation seems to give more accurate results. Remarkable are high errors within model FMQ's low temperature and pressure region. Within this region, Fuller's method is stated to be accurate, which could indicate inaccurate modeling of the tortuosity factor of the investigated rock samples by Millington & Quirk.

3.3.1.2.5 Validation of numerical implementation by reproduction of experimental results

To predict the mixing effects governed by molecular diffusion on larger scales, the experiments were reproduced within numerical simulations in DuMu^x. For this purpose, the developed fluid system (see Section 3.2.2) was used. For the spatial discretization, representing the core sample ($\approx 6\,\mathrm{cm}$) between the two chambers, a one-dimensional grid with 100 equidistant elements was defined. While the first chamber possesses a relatively large volume, the second chamber solely represents the gas distribution element. An extrusion factor corresponding to its area was introduced to consider the axial cross-section of the rock specimen. The CVFE method was selected for the discretization method due to its versatile possibilities of evaluating gradients locally. The porosity and permeability of the domain were defined homogeneously and parameterized with the measured values from the laboratory. With respect to the initialization of the system, all elements contain only gas, which is composed entirely of hydrogen following the experimental procedure. Both pressure and temperature were defined as the experimental conditions. To model the two chambers at the sides of the core sample, time-dependent Dirichlet boundaries were used to mimic the changing concentrations of hydrogen and methane within the chambers as displayed in Figure 3.8. The time-dependent Dirichlet boundaries are updated explicitly in every time step. Based on the substance present in a chamber (cf. Eq. 3.30), the molar concentration can

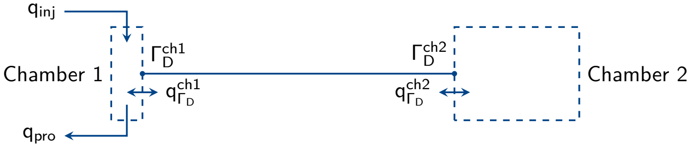

Figure 3.8: Schematic representation of the domain including the modeling of the chambers

be determined by Eq. 3.31.

$$pV = nRTZ \tag{3.30}$$

$$c^\kappa = \frac{n^\kappa}{\sum_\kappa n^\kappa} \tag{3.31}$$

where p is the pressure in Pa, V is the volume of the chamber in m^3, n is the amount of substance in mol, R is the universal gas constant in J/(K·mol), Z is the compressibility factor, and c^κ is the concentration of component k.

The concentration change in the chambers is determined by a material balance of each chamber of the previous and current time step (Eq. 3.32).

$$n_t^\kappa = n_{t-1}^\kappa - \frac{\mathrm{d}n^\kappa}{\mathrm{d}t}\Delta t \tag{3.32}$$

where t denotes the new time, $t-1$ corresponds to the previous time step, and Δt is the time step size in s. The change in substance over time is thereby influenced by the flux over the boundary and additional injection/production in/from the chamber.

$$\frac{\mathrm{d}n^\kappa}{\mathrm{d}t} = q_{\Gamma_D}^\kappa + q_{\mathrm{inj}}^\kappa - q_{\mathrm{pro}}^\kappa \tag{3.33}$$

where q_{Γ_D} is the flux over the Dirichlet boundary in mol/s and q_{inj} and q_{prod} are the injection and production rates from a chamber in mol/s. The boundary flux can be obtained implicitly with:

$$q_{\Gamma_D}^\kappa = \Big(\underbrace{c_g^\kappa \frac{K k_{rg}}{\mu_g} \nabla p}_{\text{advective flux}} + \underbrace{D_{\mathrm{pm}}^{\kappa,\mathrm{eff}} \nabla c_g^\kappa}_{\text{diffusive flux}}\Big) \varrho_g A \tag{3.34}$$

where K is the absolute permeability in m^2, k_{rg} is the relative permeability (here: $k_{rg} = 1$ due to single-phase gas flow), μ_g is the dynamic viscosity of the gaseous phase in $\mathrm{Pa \cdot s}$, ϱ_g is the molar density in $\mathrm{mol/m^3}$, and A is the cross-section area in m^2.

Concerning the first chamber, where a continuous injection of methane and production of the gas mixture occurs, the contribution to the gas composition is summarized in Eqs. 3.35 to 3.36. For the production composition, the concentration of the previous time step was selected to simplify the numerical model. However, one limitation is that the maximum time step size directly depends on the volume of the tiny chamber 1 and the rate of the continuous flushing and is therefore set to 20 s in the present study.

$$q^{\kappa}_{\mathrm{inj}} = c^{\kappa}_{\mathrm{inj}} q_{\mathrm{flush}} \tag{3.35}$$

$$q^{\kappa}_{\mathrm{pro}} = c^{\kappa}_{\mathrm{ch1},t-1} q_{\mathrm{flush}} \tag{3.36}$$

where c_{inj} is the injection composition (here: only methane), q_{flush} is the continuous production and injection rate in mol/s, and $c^{\kappa}_{\mathrm{ch1},t-1}$ is the concentration in chamber 1 of the previous time step.

A summary of the boundary definition can be found in Table 3.5.

Table 3.5: Overview of the definition of the primary variables of the Dirichlet boundaries for chamber 1 and 2

Pri. variables	Chamber 1	Chamber 2
p_g	$p_{\mathrm{init}} = p_{\mathrm{exp}}$	$p_{\mathrm{init}} = p_{\mathrm{exp}}$
S_w	0	0
c^{κ}_g	$c^{\kappa}_{\mathrm{ch1},t} = \frac{n^{\kappa}_{\mathrm{ch1},t-1} - (q^{\kappa}_{\Gamma_D} + q^{\kappa}_{\mathrm{inj}} - q^{\kappa}_{\mathrm{pro}})\Delta t}{\sum_k n^{\kappa}_{\mathrm{ch1},t-1} - (q^{\kappa}_{\Gamma_D} + q^{\kappa}_{\mathrm{inj}} - q^{\kappa}_{\mathrm{pro}})\Delta t}$	$c^{\kappa}_{\mathrm{ch2},t} = \frac{n^{\kappa}_{\mathrm{ch2},t-1} - q^{\kappa}_{\Gamma_D} \Delta t}{\sum_k n^{\kappa}_{\mathrm{ch2},t-1} - q^{\kappa}_{\Gamma_D} \Delta t}$

3.3.1.2.6 Results and comparison of numerical simulations with the laboratory observations

Figure 3.9 compares the simulated and measured results of the reference case. The general matching parameter is the hydrogen concentration in the gas stream of chamber 1. It is evident that initially, the hydrogen in the chamber is displaced by methane, leading to a rapid drop in the hydrogen concentration. Generally speaking, the higher the hydrogen concentration in the first

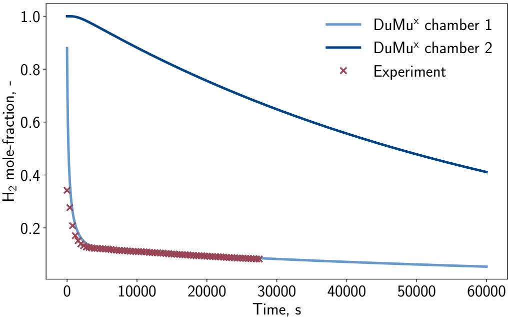

Figure 3.9: Comparison of hydrogen fractions versus time observed in laboratory and modeled in DuMu^x for the reference sample at reference conditions ($T = 40\,^\circ C$ and $p = 100\,\text{bar}$)

chamber, the higher the flux by molecular diffusion. Regarding the match quality between observed and modeled data, the implementation in DuMu^x shows similar hydrogen concentrations and a congruent slope dependent on time. Based on the simulations, it is also possible to evaluate the spatial distribution of the gas composition within the core sample as depicted in Figure 3.10. Again, the simultaneous decrease in the hydrogen concentration and increase in methane content can be observed. For this specific case, the first influence of methane in the second chamber is remarkable after approximately 2000 s, with a continuously increasing trend.

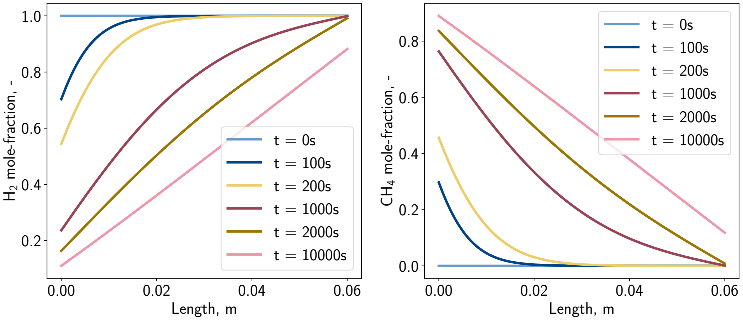

Figure 3.10: Spatial distribution of hydrogen and methane concentration within the first 10 000 s

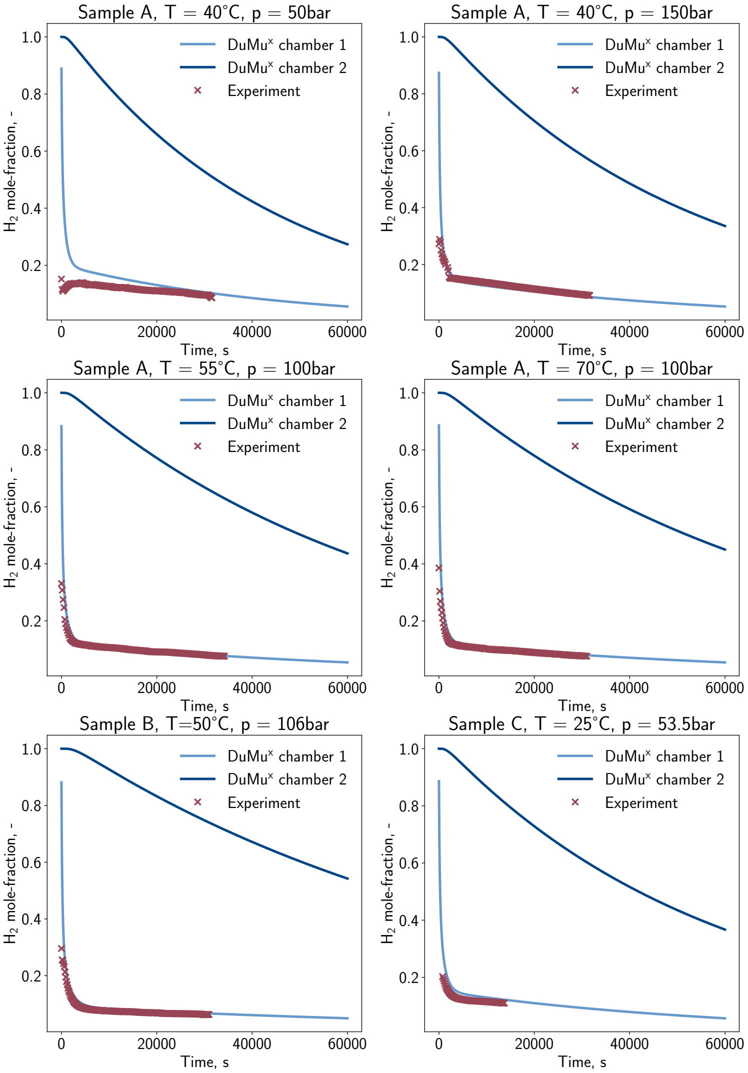

Figure 3.11: Hydrogen concentration versus time for four selected cases of sample A (Bentheimer) at different thermodynamic conditions and for two arbitrary samples from actual storage formations

The quality of the correlations and implementation was evaluated at different thermodynamic conditions. Figure 3.11 depicts measurements and the results of the simulation at typical and actual storage conditions. The first case ($T = 40\,^\circ\mathrm{C}$ and $p = 50\,\mathrm{bar}$) shows a deviation, which is expected due to the high relative error of $\delta_{D_{\mathrm{pm}}^{\mathrm{AB}}} \approx 50\,\%$ of the correlation. For the other three cases, the modeling of the experiments yields congruent and satisfying results. Similar qualities of match with minor variance can be observed for the samples from actual storage formations.

In general, implementing the developed correlation in DuMu$^\mathrm{x}$ permitted a good reproduction of the laboratory experiments. Deviations between the modeled and observed results were mainly caused by inaccuracies in the developed correlation.

3.3.2. Characterization of microbial growth parameters on laboratory scale

To calibrate the implementation in DuMu$^\mathrm{x}$ qualitatively and quantitatively, microbiological experiments conducted and published in Strobel et al. [140] were reproduced in this work. The corresponding study focused on the growth of microbes in batch reactors, allowing growth parameters such as maximum growth rate and yield to be obtained.

3.3.2.1. Experimental investigations of microbial growth in batch

In the experimental work of Strobel et al. [140], an isolated species of methanogenic microbes (Methanothermococcus thermolithotrophicus - DSMZ No. 2095) was placed in reactors and exposed to a H_2-CO_2 (80:20) atmosphere. The reactors ($V = 132.5\,\mathrm{ml}$) were filled with nutrient medium to provide a suitable growth environment. The temperature was set constantly to $T = 60\,^\circ\mathrm{C}$, which corresponds to the optimal temperature for this particular species, and the initial pressure was set to $p_{\mathrm{init}} = 1.8\,\mathrm{bar}$. The parameters measured included the absolute pressure (continuously) as it progressively decreased during the experiment and the microbial density, which was determined by counting the microorganisms before, during, and after the experiment. The substrate was supplied only once at the beginning of the experiment.

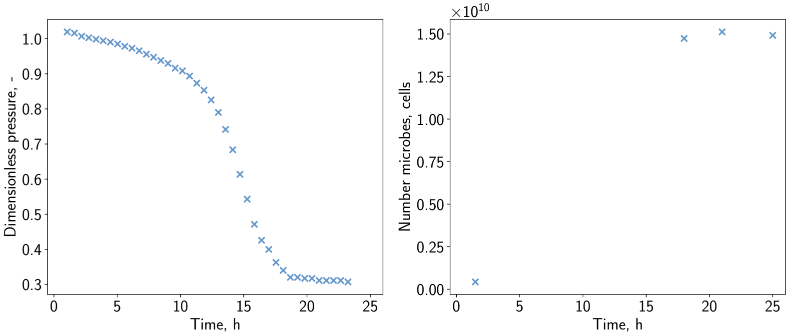

Figure 3.12: Results of batch experiment [140] - Pressure (standardized) decrease with simultaneously growth versus time

Figure 3.12 displays the observations from the laboratory. The simultaneous decrease in pressure and an increase in population size provide evidence of biochemical metabolism associated with the conversion of hydrogen and carbon dioxide to methane and water. The pressure trend can be explained by the exponential growth of the organisms while the substrate supply is sufficient. However, the pressure drop halts as soon as one of the substrates becomes the limiting factor (retardation phase: $15\,\mathrm{h} < t < 18\,\mathrm{h}$), and growth subsequently decreases until it stops completely (stationary phase: $t > 18\,\mathrm{h}$).

Subsequently, Strobel et al. [140] conducted a matching procedure to determine microbial growth parameters. Compared to the present study, their model accounted for thermodynamic non-equilibrium to investigate the potential mass transfer limitations of substrates from the gaseous to the liquid phase. Additionally, since decay is challenging to observe in batch experiments and substrate limitation is expected, the impact of dying microorganisms was neglected in their model. During the matching process, the experiments were successfully reproduced with excellent accuracy, and a potential limitation related to mass transfer during the retardation phase was identified [140].

3.3.2.2. Implementation and matching of batch experiments in DuMu^x

The batch experiment was reproduced to integrate the experimental observations into the DuMu^x model. For this purpose, the developed 2pncbiogeo model with the fluid system described in Section 3.2.2 was used. A simple

0D simulation was achieved by defining a simulation domain consisting of a single cell (1D) with Neumann no-flow boundaries. The porosity was set to unity, and the system was initialized at the initial pressure of the reactor ($p_{\text{init}} = 1.8\,\text{bar}$), with a saturation of $30\,\%$ ($V_w = 40\,\text{ml}$). At the beginning of the experiment, it is assumed that only water, hydrogen, and carbon dioxide are present and distributed in the phases according to thermodynamic equilibrium. Since the DuMu$^\text{x}$ implementation does not cover the lag phase, the reaction was activated after passing this phase.

The biochemical model in DuMu$^\text{x}$ considers the continuous growth and decay of individuals as proposed by Hagemann [54]:

$$\frac{\partial(nS_w\phi)}{\partial t} = \left(\psi^{\text{growth}} - \psi^{\text{decay}}\right) \cdot n \cdot S_w \cdot \phi \tag{3.37}$$

Growth is realized through double Monod terms (see Eq. 3.7) and is primarily controlled by substrate availability. As a result, growth decelerates when substrates start to become depleted. In reality, other limiting factors, such as space or the availability of micronutrients, can also influence growth. In the model developed by Hagemann [54], the decay term (cf. Eq. 2.10) accounts for the continuous death of microbes and serves to define the upper limit of microbial density. During UHS, substrates are expected to be provided in sufficient quantities near the wellbore to reach the maximum microbial density. Theoretically, at this point, the derivative of microbial density becomes zero, and growth balances the decay rate at the maximum microbial density.

$$\frac{\partial(nS_w\phi)}{\partial t} = \left(\psi^{\text{growth}} - \psi^{\text{decay}}\right) \cdot n \cdot S_w \cdot \phi \overset{!}{=} 0 \tag{3.38}$$

Assuming that the maximum density is achieved at a water saturation and porosity of unity, the equation can be rearranged as follows:

$$\psi^{\text{growth}} n = \psi^{\text{decay}} n \tag{3.39}$$

With a linear decay rate as proposed by Hagemann [54] and inserting the double Monod terms, the model can be expressed as:

$$\psi^{\text{growth}}_{\text{max}} \underbrace{\left(\frac{c_w^{S1}}{\alpha^{S1} + c_w^{S1}}\right)}_{\to 1} \underbrace{\left(\frac{c_w^{S2}}{\alpha^{S2} + c_w^{S2}}\right)}_{\to 1} = bn \tag{3.40}$$

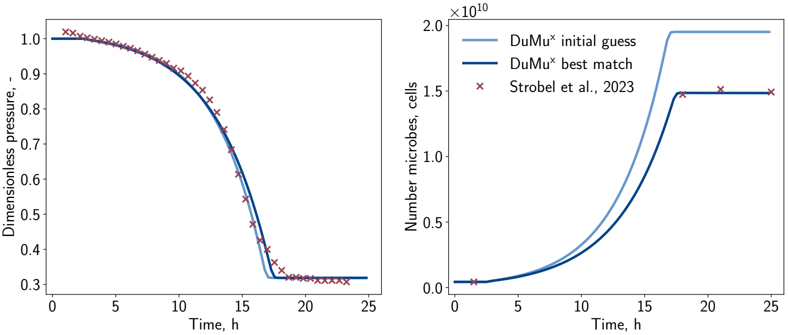

Figure 3.13: Results of the simulations in DuMu$^\text{x}$ in comparison to the observed laboratory data in [140] - Pressure drop and number of microbes in the reactor dependent on time

At maximum microbial density, the limitation is not due to an insufficient substrate supply, but rather it is caused by factors such as insufficient available space. In this case, the Monod terms tend to unity, which allows to determine the maximum microbial density as follows:

$$n_\text{max} = \frac{\psi^\text{growth}_\text{max}}{b} \tag{3.41}$$

Alternatively, for dimensionless microbial density ($n^*(t) = n(t)/n_\text{init}$):

$$n^*_\text{max} = \frac{n_\text{max}}{n_\text{init}} = \frac{\psi^\text{growth}_\text{max}}{b} \tag{3.42}$$

Assuming a volume of $1 \cdot 10^{-12}$ ml for a single microbe [142], the theoretical maximum microbial density is $1 \cdot 10^{18}/\text{m}^3$. Based on this theoretical maximum density and the initial microbial density of the batch experiment ($n_\text{init} = 1.079 \cdot 10^{13}/\text{m}^3$), the maximum density is approximately 92 655 times the initial one.

To proceed with the matching procedure, the first step involved running a simulation using parameters from Strobel et al. [140] as an initial guess (cf. Figure 3.6). Figure 3.13 presents the simulation results for the initial guess and the best match. The parameters fine-tuned during the matching process included the maximum growth rate $\psi^\text{growth}_\text{max}$, the decay factor b, and the yield factor Y. During the matching, the maximum microbial density n^*_{max} was set constant. The best match was achieved for the values listed in Table 3.6.

Table 3.6: Overview of relevant growth parameters from literature, matched within this study, and later used on field scale

Parameter	Initial guess DuMu$^{\mathrm{x}}$ [140]	Best match DuMu$^{\mathrm{x}}$	Fieldscale DuMu$^{\mathrm{x}}$	Unit
Initial number of micro., n_{init}	$1.079 \cdot 10^{13}$	$1.079 \cdot 10^{13}$	$1 \cdot 10^{7}$	$1/\mathrm{m}^3$
Maximum growth rate, $\psi^{\mathrm{growth}}_{\mathrm{max}}$	$7 \cdot 10^{-4}$	$6.3 \cdot 10^{-4}$	$6.3 \cdot 10^{-5}$	1/s
Decay factor, ψ^{decay}	0	$6.78 \cdot 10^{-10}$	$6.78 \cdot 10^{-10}$	1/s
H_2-half velocity const., $\alpha_{\mathrm{H_2}}$	$4.483 \cdot 10^{-8}$	$4.483 \cdot 10^{-8}$	$4.483 \cdot 10^{-8}$	mol/mol
CO_2-half velocity const., $\alpha_{\mathrm{CO_2}}$	$2.465 \cdot 10^{-8}$	$2.465 \cdot 10^{-8}$	$2.465 \cdot 10^{-8}$	mol/mol
Yield factor, $Y_{\mathrm{H_2}}$	$4.1 \cdot 10^{12}$	$3.1 \cdot 10^{12}$	$3.1 \cdot 10^{12}$	1/mol
Maximum micro. density, n^*_{max}	$\to \infty$	92 655	9265.5	-

Although the DuMu$^{\mathrm{x}}$ implementation allows for proper reproduction of the experiment, some limitations of the model become evident. The first limitation is in modeling the previously mentioned lag phase without deactivating the microbial reaction. The second limitation is related to reproducing the retardation phase. In the simulation, a discontinuity is observed, whereas laboratory observations indicate a smooth transition from the exponential to the stationary phase. Strobel et al. [140] successfully modeled this phase by assuming that mass transfer from the gaseous phase into the liquid phase is limited, gradually limiting the substrate for growth. However, this extension is restricted to thermodynamic non-equilibrium models and is not applicable in the current DuMu$^{\mathrm{x}}$ implementation. Although not visible in the simulation results, the model faces difficulties in modeling the stationary phase when $\psi^{\mathrm{decay}} \neq 0$.

In addition to matching observed data, the simulation provides insights into limiting mechanisms. Figure 3.14 depicts the amount of substance of each species in the reactor over time. The reaction pathway is clearly visible, with hydrogen and carbon dioxide decreasing as methane is produced. Growth limitation, as expected and also observed by Strobel et al. [140], is caused by the depletion of the substrate hydrogen, as the hydrogen content tends to zero.

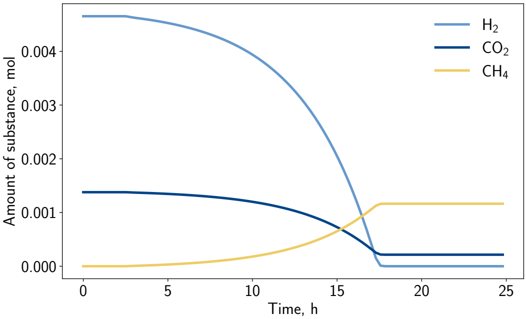

Figure 3.14: Results of simulation in DuMu^x - Total amount of substance (gas and water) versus time

3.3.2.3. Transfer from laboratory scale to field scale

The batch experiment demonstrated that introducing hydrogen into the subsurface in combination with the initial gas can promote microbial growth, resulting in a significant loss of stored hydrogen. However, the transfer from laboratory observations to the field scale remains unknown. As mentioned earlier, there are reasons for both acceleration and deceleration of the reaction in the subsurface. Acceleration is mainly attributed to the larger interface between the phases inside the pores compared to batch experiments, allowing for faster substrate transfer. However, the experiments in Strobel et al. [140] indicate that this effect has only a minor impact on growth and is related to substrate limitations. On the contrary, deviations from ideal growth conditions, such as temperature, pH, salinity, and micronutrient availability, will lead to a reduced growth rate. Missing trace elements must be obtained from dead cells, and the available space is shared with other microorganisms. Therefore, the different behavior of batch and in-situ growth is case dependent and the transfer between these scenarios is still a subject of research.

In this study, the selection of growth parameters for the field scale was based on laboratory observations, assuming that growth occurs one order of magnitude slower due to inappropriate growth conditions. Furthermore, it was assumed that the initial microbial density is lower ($n_{\text{init}} = 1 \cdot 10^7/\text{m}^3$). The decay rate was selected identically to the batch experiment due to the presence of other species (space limitation) and limitations of trace elements. This leads to a maximum microbial density for the field case of $n_{\text{max}} = 9.2655 \cdot 10^{10}/\text{m}^3$. Concerning the sulfate-reducing bacteria, the growth parameters for the field-scale simulation were based on previous studies and literature [55] and defined as listed in Table 3.7. After the calibrations, first simulation runs on the field scale with the developed growth kinetics were performed to assess the potential impact on UHS efficiency.

Table 3.7: Overview of used growth parameters for the subsequent field case study

Parameter	Methanation	Sulfate reduction [55]	Unit
Initial number of microorganisms	$1 \cdot 10^7$	$6 \cdot 10^{10}$	$1/\text{m}^3$
Maximum growth rate	$6.3 \cdot 10^{-6}$	$2.0 \cdot 10^{-5}$	1/s
Decay factor	$6.78 \cdot 10^{-10}$	$2.315 \cdot 10^{-6}$	1/s
H_2-half velocity const.	$4.483 \cdot 10^{-8}$	$5 \cdot 10^{-6}$	mol/mol
CO_2/SO_4^{2-}-half velocity const.	$2.465 \cdot 10^{-8}$	$1.8 \cdot 10^{-6}$	mol/mol
Yield factor	$3.1 \cdot 10^{12}$	$1.2 \cdot 10^{13}$	1/mol
Maximum micro. density	9265.5	8.64	-

3.3.3. Calibration of pyrite-to-pyrrhotite reduction based on modeling of laboratory experiments

Various geochemical reactions are suspected to occur during the injection of hydrogen into the subsurface [60]. However, a significant part of these reactions has only a minor impact on the operation and/or is not relevant to the time horizon of interest. One of the most controversial reactions is the pyrite-to-pyrrhotite reduction coming with the generation of harmful hydrogen sulfide. A simplified reaction stoichiometry, assuming that the reaction is only occurring in one direction, can be expressed as follows:

$$\text{FeS}_2 + \text{H}_2 \longrightarrow \text{FeS} + \text{H}_2\text{S} \tag{3.43}$$

Hydrogen sulfide leads to the corrosion of well materials and is also toxic to human beings. Laboratory experiments in the early 2010s [150] addressed this reaction and observed a significant amount of generated hydrogen sulfide. To predict the pyrite-to-pyrrhotite reduction on larger scales and thereby assess the potential risk, these experiments were reproduced in DuMu$^\text{x}$ on a lab scale so that they can be afterwards applied on the field scale. The work presented in this section has been published in Hogeweg et al. [75].

3.3.3.1. Description of laboratory procedure and observations

To observe the reaction, Truche et al. [150] exposed pure pyrite to an argon-hydrogen (10 % H_2) atmosphere at pressures of 80 bar to 180 bar and temperatures of 90 °C to 180 °C. In the first step, ultrafine pyrite was exposed to this atmosphere, and quantitative analyses proved the presence of the reaction. For buffering, minor parts of calcite were added to the pyrite powder. During the exposure, a progressive precipitation of pyrrhotite with a simultaneous discharge of hydrogen sulfide was observed. To quantify the amount of hydrogen sulfide produced and subsequently build a model, experiments on crushed pyrite powder (measured specific surface area $A_{\mathrm{spec}} = 0.78\,\mathrm{m}^2/\mathrm{g}$) were performed.

In general, the experimental workflow was composed of the following steps: 1) Placing solid and liquid material in the high-pressure reactors (300 ml and 450 ml), 2) flushing with argon to remove dissolved oxygen, and 3) increasing the pressure by injecting the argon-hydrogen gas to the defined experimental condition [150]. During the exposure with a time of up to 14 days, liquid samples were taken from the reactor periodically. Scanning electron microscope (SEM) images were taken after the experiment for textural and morphological analysis. Additionally, specific surface area analyses (BET) and electron microprobe (EMP) analyses were performed.

With a focus on modeling the reaction quantitatively, Truche et al. [150] selected eight out of eleven performed experiments with sized pyrite particles and reproduced the experiments within PHREEQC [26]. The corresponding experimental matrix is depicted in Table 3.8. For the selection of experiments, the amount of hydrogen sulfide released was determined, and afterwards, a

Table 3.8: Experimental matrix design for the characterization of pyrite-to-pyrrhotite reduction with crushed pyrite powder [150]

T [°C] p_{H_2} [bar]	120	150	165	180
8	x	x	x	x
15		x		
18	x	x		x

correlation in dependency of pressure, temperature, and time was developed:

$$\log n_{\mathrm{H_2S}} = -5.22 + 0.47 \log t + 1.10 \log p_{\mathrm{H_2}} - 2755/T \tag{3.44}$$

where $n_{\mathrm{H_2S}}$ is the hydrogen sulfide production in mol/m^2, t is the elapsed time in h, $p_{\mathrm{H_2}}$ is the partial pressure in Pa, and T is the temperature in K.

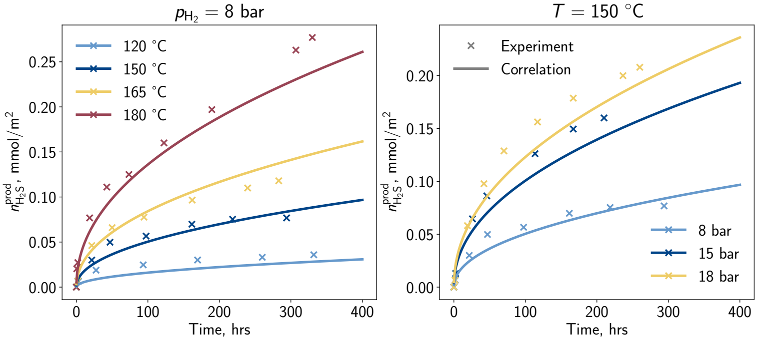

Figure 3.15: Hydrogen sulfide per surface area generated by the pyrite-to-pyrrhotite reduction determined in the laboratory and the proposed correlation [150] - Impact of temperature and pressure

The experimental data and the trend of the developed correlation (Eq. 3.44) are depicted in Figure 3.15. In general, the highest reaction rates are observed at the beginning of the experiment, with a truncating behavior in the later phase. Further, higher partial pressures and temperatures lead to a promoting effect with respect to the reaction rate.

Truche et al. [150] supposed that the reaction follows a dissolution-precipitation reaction where the pyrite dissolves into the liquid phase, reacts, and afterwards partially precipitates as pyrrhotite. Regarding the sharp reduction of the hydrogen sulfide generation, potential reasons such as approaching the equilibrium conditions or diffusive effects on the microscale were concluded. Nevertheless, it seemed that the reaction is controlled by many factors such as temperature, partial pressure of hydrogen, specific surface area, pH, and also present hydrogen sulfide content [150].

However, this model (Eq. 3.44) was developed in 0D simulations and may not be suitable for implementation in a transport model. For the purpose of field-scale simulations, hydrogen may only be present locally and time-delayed. With this correlation (Eq. 3.44), the reaction would even take place when the partial pressure of hydrogen was zero (= no hydrogen present). Additionally, big pressure changes during the operations are expected, which could cause problems. To allow the implementation for more complex systems, the results of Truche et al. [150] were used to develop a new kinetic model in this study.

3.3.3.2. Implementation of laboratory experiments case in DuMu^x

To develop the new kinetic model, the reactor experiments with pure pyrite samples of Truche et al. [150] were reproduced within DuMu^x, including the development of a new mathematical model describing the kinetics of the reaction. For the matching with the laboratory observations, the developed 2pncbiogeo model (Eq. 3.1) was used with a modified fluid system. The experiments of Truche et al. [150] involved the chemical components of water (H_2O), argon (Ar), hydrogen (H_2), and hydrogen sulfide (H_2S). Therefore, this simplified fluid system consisting of these four components was implemented in DuMu^x. The density of the gas is described by Peng and Robinson [116] EoS, and further, thermodynamic properties are in alignment with previous fluid system implementations. Besides the fluid system, a new solid system consisting of three components was defined: pyrite (FeS_2) and pyrrhotite (FeS) as reactive and quartz as inert. As the volume fraction of quartz is assumed to behave static, it can be neglected in the system of equations and defines rather the maximum porosity. Furthermore, the solid components are assumed to be insoluble in the fluid phase.

A simple 1D simulation with only one grid cell containing the volume of the reactor (300 ml/450 ml) was defined and the initialization was according to the experimental procedure. The water saturation ranged from 55 % to 71 %. The initial volume fraction of pyrite grains ($A_{\text{spec}} = 780\,\text{m}^2/\text{kg}$) was defined as 5 %. The temperature (120 °C, 150 °C, 165 °C, and 180 °C) and partial pressure (8 bar, 15 bar, and 18 bar) was initialized based on the experiments. Noteworthy, all laboratory experiments were conducted with a gas composition of 10 % H_2 and 90 % Ar, merely the absolute pressure was changed to achieve the variance in partial pressure of hydrogen.

During the simulation, all spatial boundaries were defined as Neumann no-flow boundaries. This led to an implementation where no flow can occur and the PDE system from Eqs. 3.1 and 3.2 could be reduced to the following system of ODEs:
For fluid components $\kappa = H_2O, Ar, H_2, H_2S$:

$$\frac{d\phi \sum\limits_{\alpha=g,w} \varrho_\alpha c_\alpha^\kappa S_\alpha}{dt} = q_{\text{geo}}^\kappa \tag{3.45}$$

For solid components $\kappa_s = FeS_2, FeS$:

$$\varrho^{\kappa_s} \frac{d\phi_s^{\kappa_s}}{dt} = q_{\text{geo}}^{\kappa_s} \tag{3.46}$$

Here, only changes in the fluid composition are caused by the geochemical reaction represented by the source term.

3.3.3.3. Development of kinetic reaction model describing pyrite-to-pyrrhotite reduction

After implementing the experimental conditions in DuMu$^\text{x}$, a mathematical model was developed and matched with the laboratory observations. The limited amount of experiments did not allow to build a typical kinetic rate relationship, including mass action coefficients. Hence, an empirical rate model mimicking the experimental results was developed, which, nevertheless, originated from the general formulation (Eq. 2.17):

$$q_{\text{geo}}^\kappa = \gamma_{\text{geo}}^\kappa \left(A_s^{\text{FeS}_2} k \underbrace{\left(1 - \frac{Q_m}{K_m}\right)^\theta}_{\delta} \right) \phi_s^{\text{FeS}_2} \tag{3.47}$$

where q_{geo}^κ is the geochemical source term of component κ in $\text{mol}/(\text{m}^3 \cdot \text{s})$, $\gamma_{\text{geo}}^\kappa$ is the stoichiometric coefficient of the reaction, $A_s^{\text{FeS}_2}$ is the specific surface area of the mineral pyrite in m^2/m^3, k is the rate constant in $\text{mol}/(\text{m}^2 \cdot \text{s})$, δ is representing the dimensionless mass action term of the general formulation, and $\phi_s^{\text{FeS}_2}$ corresponds to the volume fraction of pyrite.

With respect to the simplified form of the pyrite-to-pyrrhotite reduction (Eq. 3.43), the stoichiometric coefficients γ_{geo} can be expressed as follows:

$$\gamma_{\text{geo}} \begin{pmatrix} \text{H}_2\text{O} \\ \text{Ar} \\ \text{H}_2 \\ \text{H}_2\text{S} \\ \dots \\ \text{FeS}_2 \\ \text{FeS} \end{pmatrix} = \begin{pmatrix} 0 \\ 0 \\ -1 \\ 1 \\ 0 \\ -1 \\ 1 \end{pmatrix} \tag{3.48}$$

For non-participating components such as H_2O and Ar the coefficient is zero.

In the experimental work of Truche et al. [150], a progressive reduction of the reaction rate was observed. As mentioned earlier, Truche et al. [150] concluded that beyond other influencing parameters, the hydrogen and hydrogen sulfide concentrations are crucial parameters controlling the overall reaction. For this purpose, the mass action term is represented by the coefficient δ which depends on the mentioned concentrations in the liquid phase ($c_w^{\text{H}_2}$ and $c_w^{\text{H}_2\text{S}}$). Furthermore, the rate constant k depends on the thermodynamic parameters of temperature and pressure. For the experiments, it is assumed that the surface is completely exposed for the reaction, while in the subsurface, the pyrite is incorporated in other minerals of the rock matrix. In order to achieve circumstances mirroring reality, the introduction of a dimensionless scaling factor C_{scaling} is commonly applied to reduce the exposed reactive surface and simultaneously the reaction rate. Typically, this parameter is fitted to the experimental observations on compositional rock samples, or arbitrary values are taken [16]. Established values are in the range of 10^{-3} to 10^{-1} [16]. For the reproduction of the experiments, it was assumed that the surface of the pyrite grains is fully accessible, and consequently, the scaling factor equals one ($C_{\text{scaling}} = 1$). Overall, this yields the following kinetic reaction rate:

$$q_{\text{geo}} = \gamma_{\text{geo}} A_s^{\text{FeS}_2} k\,(p, T)\,\delta\left(c_w^{\text{H}_2}, c_w^{\text{H}_2\text{S}}\right)\phi_s^{\text{FeS}_2} C_{\text{scaling}} \tag{3.49}$$

It is expected that due to the reaction, the pressure, hydrogen, and pyrite concentrations decrease while the hydrogen sulfide and pyrrhotite contents increase. However, this requires a simultaneous matching of the kinetic rate k and the mass action term δ. The matching was performed within an iterative process (trial and error) in DuMu$^{\text{x}}$. Due to the limited amount of data

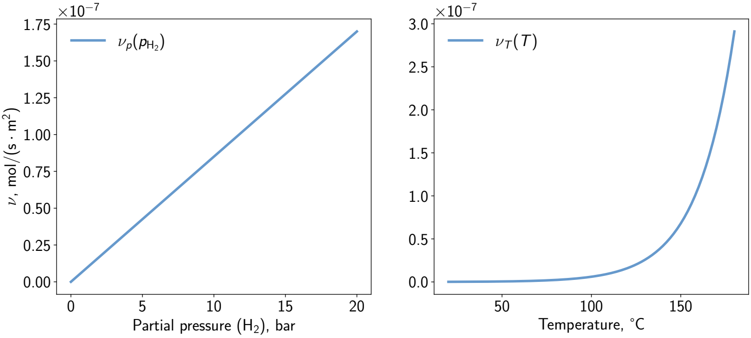

Figure 3.16: Trend of the developed correlation modeling the impact of (a) partial pressure (T = 150 °C) and (b) temperature (p = 80 bar) on the geochemical reaction

points, the correlation was built based on basic functions such as linear for the pressure and exponential function for temperature. For the kinetic rate constant, the best match was achieved as follows:

$$k\left(p,T\right) = 4.23 \cdot 10^{-18} p \cdot 1.010\,15^{4.8T-1050} \tag{3.50}$$

The resulting trends of the pressure and temperature dependency are visible in Figure 3.16. Due to the linear trend, with doubling the pressure, the reaction rate is also doubled. The strongly increasing kinetic rate with higher temperatures is visible. However, it is worth mentioning that the experimental data are only available for discrete points within the interval 120 °C to 180 °C, leading to uncertainties at lower temperatures. For the mass term, a rational term was used. For the denominator (here: hydrogen sulfide concentration), a case distinction for values tending against zero is required:

$$\delta\left(c_w^{\mathrm{H_2}}, c_w^{\mathrm{H_2S}}\right) = \frac{{c_w^{\mathrm{H_2}}}^2}{c_w^{\mathrm{H_2S}}} \quad \text{with: } c_w^{\mathrm{H_2S}} = \begin{cases} 10^{-8}, & \text{for } c_w^{\mathrm{H_2S}} \leq 10^{-8} \\ c_w^{\mathrm{H_2S}}, & \text{for } c_w^{\mathrm{H_2S}} > 10^{-8} \end{cases} \tag{3.51}$$

The result of the developed correlation for constant temperature ($T = 150\,°\mathrm{C}$) and varying initial pressure experiments is depicted in Figure 3.17A. A proper match is visible for the low and medium-pressure experiments, and only a minor deviation in the advanced experiment is observable for the high-pressure case. Figure 3.17B depicts the results of the matching regarding varying tem-

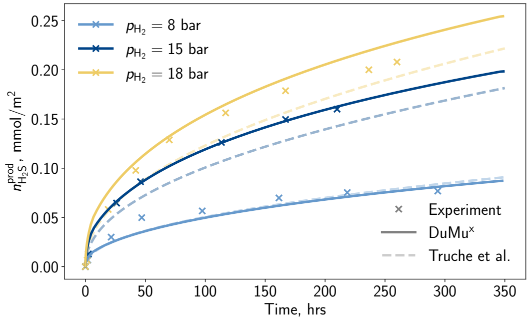

(A) Pressure dependency (T = 150 °C))

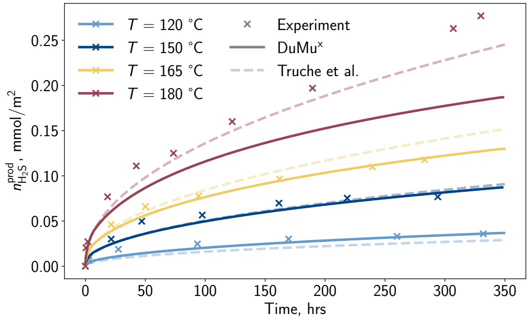

(B) Temperature dependency ($p_{H_2} = 8$ bar)

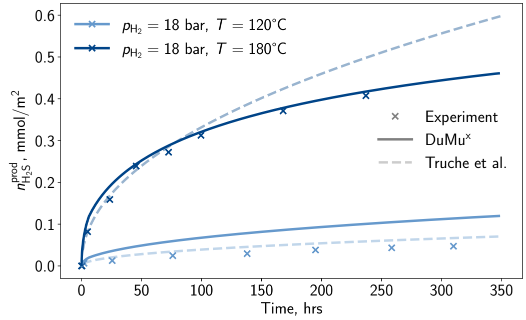

(C) Additional experiments outside of the reference conditions

Figure 3.17: Hydrogen sulfide per surface area generated by the pyrite-to-pyrrhotite reduction determined in the laboratory [150], with the correlation of Truche et al. [150], and the model developed in this study

peratures. For temperatures below 165 °C a good match is achieved, while for 180 °C a deviation from the experimental observations is remarkable. Besides the measurements at reference partial pressures and temperatures, two additional measurements were selected by Truche et al. [150] for developing the correlation. In the present study, these additional experiments were used to validate the new model. The comparison between measured and modeled data is depicted in Figure 3.17C.

In summary, the recently developed correlation (cf. Eq. 3.49) demonstrates the capability to reproduce the experimental findings of Truche et al. [150] within an acceptable accuracy. It provides a satisfactory match for measurements beyond the reference conditions. Compared to the correlation developed by Truche et al. [150], the recent correlation exhibits similar quality, with improved behavior regarding pressure dependency. Moreover, this correlation can be implemented in time- and spatial-dependent simulations to assess the risk of hydrogen sulfide production resulting from pyrite-to-pyrrhotite reduction. However, it is crucial to note that the modeling of the kinetic rate relies on eight experiments conducted at high temperatures, primarily for potential nuclear waste disposal scenarios. The exact impact of hydrogen concentration and absolute pressure is still uncertain due to the experiments maintaining a static hydrogen concentration of 10 %. It is recommended to conduct independent analyses involving additional experimental investigations with varying hydrogen concentrations and absolute pressures, followed by modeling to enhance the developed correlation describing the reaction.

3.4. Benchmark study for the simulation of UHS operations

Benchmarking is a crucial method for comparing implementations in different tools, such as simulators, by analyzing predefined inputs and comparing their outcomes. This study presents an extension of a recently developed benchmark study for UHS scenarios [70]. The focus was on incorporating geochemical reactions and comparing their impact on the UHS operation. This section corresponds to a large extent to the work published in Hogeweg et al. [70] and Hogeweg et al. [75].

3.4.1. Benchmark scenario description

While the original benchmark scenario primarily addressed variations in injection fluid composition (low and high hydrogen content), this study extends the investigation to explore the effects of both geochemical and biochemical reactions on UHS operations. Four cases were defined to achieve this, each varying in the presence of reactions (see Figure 3.18).

3.4.1.1. Field characteristics/static model

A corner-point grid based on a semi-artificial geological structure was used for the spatial discretization of the simulation (cf. Figure 3.19). Overall, it consists of 44 652 (61 x 61 x 12) grid cells with a dimension of 50 m x 50 m (x- and y-direction) and a varying thickness. The petrophysical properties (porosity and permeability) were distributed heterogeneously, and the permeability was additionally defined as anisotropic. The average porosity is 15 %, and the mean horizontal permeability is 143 mD ($k_v \sim 3$ mD), which can be observed in some sandstone formations in Northern Germany (permeability distribution based on a modified poro-perm-correlation).

3.4.1.2. Initialization

The system was initialized with a pressure of $p_{\mathrm{GWC}} = 81.6$ bar at the gas-water-contact at a depth of 1210 m. A transition zone was established by the capillary pressure (Brooks-Corey [18] parameter $\lambda = 2.0$, $p_e = 0.1$ bar) separating the gas and water zone. The initial gas composition in the gas zone was defined as natural gas (see Table 3.9) [47]. Due to the vaporization

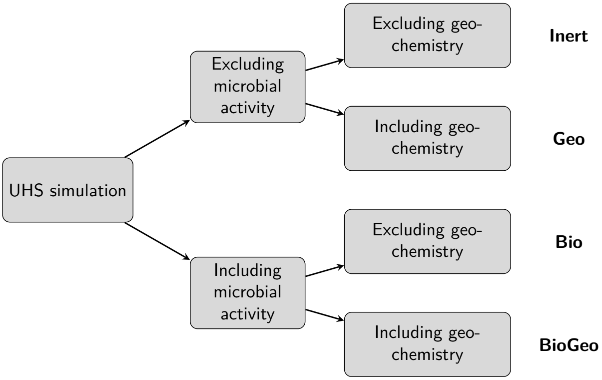

Figure 3.18: Simulation cases varying in presence of bio- and geochemical reactions

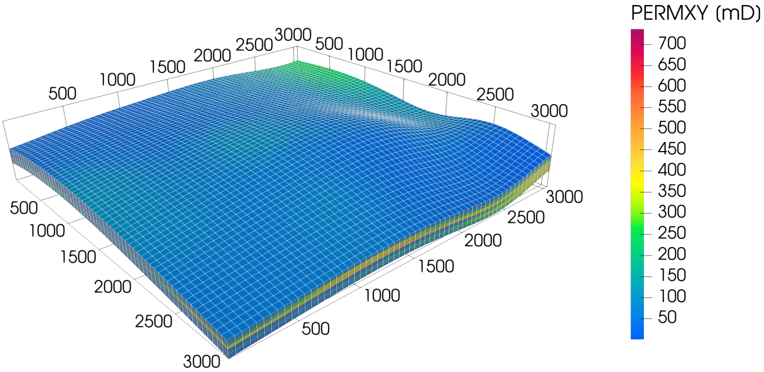

Figure 3.19: General overview of the geological structure (here: k_h)

Table 3.9: Relevant fluid compositions in molar percent

Component	Initial	Injection
Methane (CH_4)	87.61	78.85
Ethane (C_2H_6)	0.12	0.65
Pseudo comp. (C_{3+})	0.06	0.05
Hydrogen (H_2)	0.00	10.00
Carbon dioxide (CO_2)	2.52	2.27
Nitrogen (N_2)	9.09	8.18
Sum	100.00	100.00

of water in the gaseous phase, there is a minor concentration of H_2O in the gas phase. The liquid phase additionally contained sulfate (0.033 75 %) and, depending on the case, microorganisms (methanogenic archaea and sulfate-reducing bacteria). The initial mineral concentration of pyrite was defined homogeneously as 1 % (total volume fraction), whereby it typically varies from not detectable up to a few percentages for sandstones [5, 119]. The isothermal temperature was set to 80 °C, different from the initial study (60 °C), as geochemical reactions are not expected at lower temperatures.

3.4.1.3. Operation schedule

In the present study, the schedule comprises two sections: 1) Conversion from natural gas storage into UHS and 2) Regular storage operation. In both sections, the injection/production occurs along a single well located in the center of the structure. The injected gas compositions remain constant (see Table 3.9). With respect to the step-wise development of UHS, a low hydrogen concentration of 10 % may be interesting in first field projects (e.g. Underground Sun Storage [124] and HySTORAGE [141]). The first section, the conversion cycle, is characterized by a bottom-hole-pressure controlled injection, which is incrementally increased from 90 bar to 102 bar (step size: 4 bar) to increase the reservoir pressure and raise the hydrogen content in the storage. In total, four cycles consisting of 60 days with one month of idle time between each cycle were simulated. After the conversion cycles, regular storage cycles are conducted. The regular operation consists of alternating injection and production with a constant rate of $q = 293.13\,\mathrm{mol/s} = 6 \cdot 10^5\,\mathrm{Sm^3/d}$. The duration of the injection is identical to the withdrawal (90 days) to equalize the cumulative volumes. Like the conversion cycles, the regular storage cycles are separated by idle times.

3.4.2. Results and discussion

In general, four simulation cases were conducted, varying in the presence of bio- and geochemical reactions. Figure 3.20 illustrates relevant field parameters of the simulations. In the initial cycles, pressure-controlled injection is notably evident, characterized by varying rates and progressively decreasing behavior. After the conversion cycles, the regular operation with constant rates becomes visible. All cases exhibit identical behavior in this phase, and no differences are observed regarding the operation rate. During the conversion cycles, a step-wise increase in pressure from 81.6 bar to 93 bar is observed and attributed to the injection of the natural gas-hydrogen blend to establish an initial hydrogen cushion within the storage. The subsequent storage cycles feature alternating pressure with an amplitude of approximately 2 bar. While the pressure trend is nearly identical for all cases during the conversion period, initial differences emerge during the storage operation phase. A progressive pressure drop over time is observed for cases considering biochemical reactions, while geochemical reactions appear to have a negligible impact on the average reservoir pressure. The pressure drop caused by biochemical reactions arises from the consumption of 5 and 6 moles of substrate and the discharge of 3 and 5 moles of products, respectively.

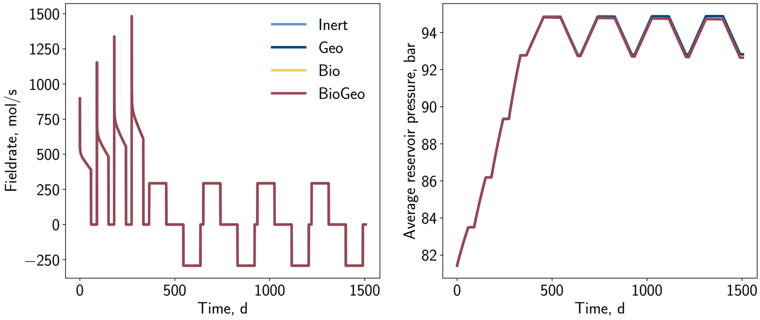

Figure 3.20: Field rate and average reservoir pressure in dependency of time

During UHS, the composition of the gas produced is essential. Significant variations and contamination by specific components, such as hydrogen sulfide, are unfavorable. Figure 3.21 displays the corresponding mole fractions of relevant gases (H_2, CO_2, and H_2S) during the four production cycles. The

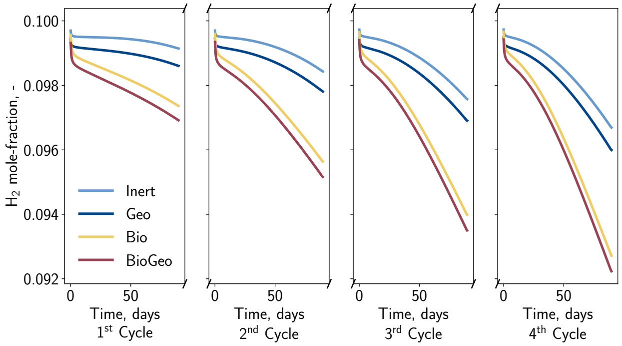

(A) Hydrogen mole fraction

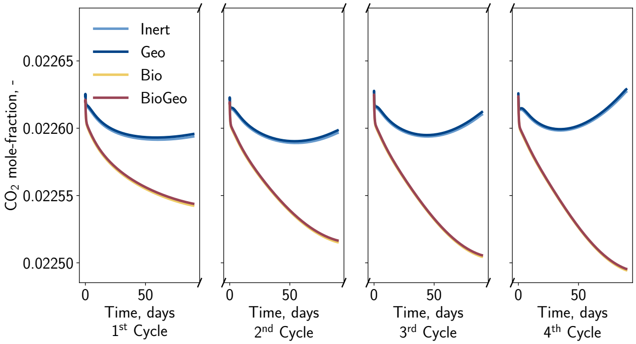

(B) Carbon dioxide mole fraction

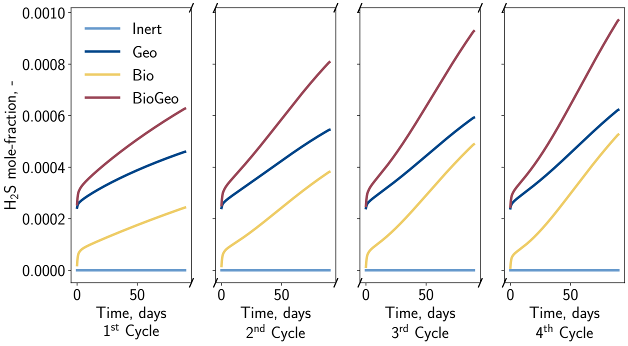

(C) Hydrogen sulfide mole fraction

Figure 3.21: Gas composition in the gas stream during the four withdrawal phases

impact of the general mixing but also the impact of potential bio- and geochemical reactions is observable.

Generally, it is reasonable that the share of hydrogen in the production stream (see Figure 3.21A) is close to the injection concentration at the beginning of each cycle. This fraction decreases with time as the gas is recovered from more distant regions, which is more likely to be mixed with the initial gas. Overall, this mixing can be counted as a loss of hydrogen and is, therefore, mainly responsible for the efficiency of UHS. Contrary to chemical reactions, this hydrogen loss can be partially compensated during the final depletion of the storage and can be assumed to be temporary. Regarding cases considering chemical reactions, the drop in the hydrogen fraction in the withdrawal stream is more significant, indicating additional losses. For the particular growth conditions, the influence of methanation and sulfate reduction seems to be stronger than the pyrite-to-pyrrhotite reduction.

Further conclusions can be obtained from evaluating additional major relevant components such as carbon dioxide (cf. Figure 3.21B). In cases where carbon dioxide acts as a substrate for methanation, the carbon dioxide concentration monotonously decreases within each cycle. For the remaining cases, the concentration drops initially but recovers thereafter. This behavior can be used to detect the presence of microorganisms consuming carbon dioxide, while the hydrogen fraction could be interpreted as ambiguous, as the mixing with the initial gas could also cause the reduction.

The products of the reactions are also visible in the production stream. Due to the initial absence of hydrogen sulfide, it can be clearly distinguished from the injected and cushion gas. In Figure 3.21C, it is visible that with increasing cycles, the hydrogen sulfide content in the gas stream increases. Remarkably, for cases including the geochemical reactions, the hydrogen sulfide concentration at the beginning of each cycle does not correspond to the injection concentration; moreover, it seems that pyrite and hydrogen are progressively converted during the idle state of the well. This can be explained by the fact that the reaction is far from equilibrium at higher hydrogen fractions in combination with low or absent hydrogen sulfide, which leads to an acceleration of the reaction. Conversely, the presence of sulfate-reducing bacteria decreases the reaction rate of the pyrite-to-pyrrhotite reduction over time.

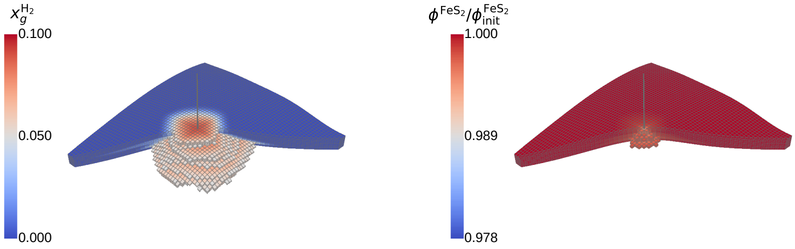

Figure 3.22: Spatial distribution of a) hydrogen mole fraction (gaseous phase) and b) the ratio of current to initial pyrite volume fraction at the end of the fourth storage cycle for case BioGeo (threshold: 50 % and 80 %)

The observations from the gas composition during withdrawal can also be seen when looking at the spatial distribution of hydrogen, pyrite, and microbial density of the two species. Focusing on the hydrogen fraction (cf. Figure 3.22), the highest hydrogen content remains close to the wellbore. It decreases with growing distance until reaching the initial cushion gas. The geochemical reaction mainly occurs around the wellbore, indicated by a ratio of the actual to initial pyrite smaller than unity. Here, the cyclic displacement of hydrogen sulfide leads to a repeated reaction rate acceleration. More distanced regions are consequently more saturated with hydrogen sulfide due to the displacement and generation by sulfate-reducing bacteria. This leads to conditions close to the equilibrium of the geochemical reaction. The accumulation of hydrogen sulfide similar to a halo around the wellbore is observable in Figure 3.23.

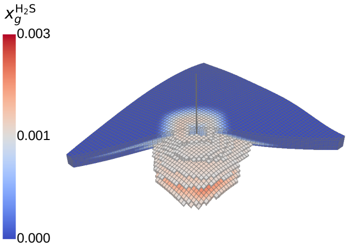

Figure 3.23: Spatial distribution of hydrogen sulfide mole fraction at the end of the fourth storage cycle for case BioGeo (threshold: 50 %)

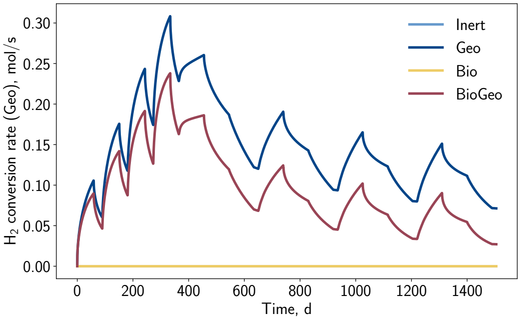

Figure 3.24: Hydrogen conversion rate by geochemical reaction (pyrite-to-pyrrhotite reduction) in the entire storage formation versus time

The observations from the spatial analysis are also visible in the geochemical conversion rate, as depicted in Figure 3.24. A step-wise increase in the reaction rate is discernible, caused by the growing hydrogen cushion. Nevertheless, the equilibrium of the reaction is progressively achieved, indicated by a drop in the reaction rate. With the overall increasing hydrogen sulfide content, the reaction decelerates globally, and it becomes less dominant with increasing storage cycles. It is visible that the geochemical reaction occurs slower for cases where sulfate-reducing bacteria are active, as they contribute to a higher overall hydrogen sulfide concentration, easing the reaction.

Focusing on the activity of microorganisms (cf. Figure 3.25), it is expected

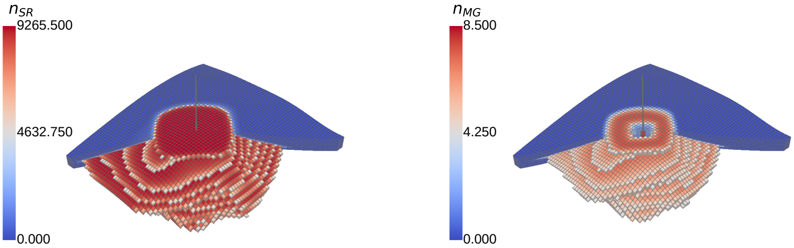

Figure 3.25: Spatial distribution of (dimensionless) microbial density of a) sulfate-reducing organisms and b) methanogenic microbes at the end of the fourth storage cycle of case BioGeo (threshold: 50 %)

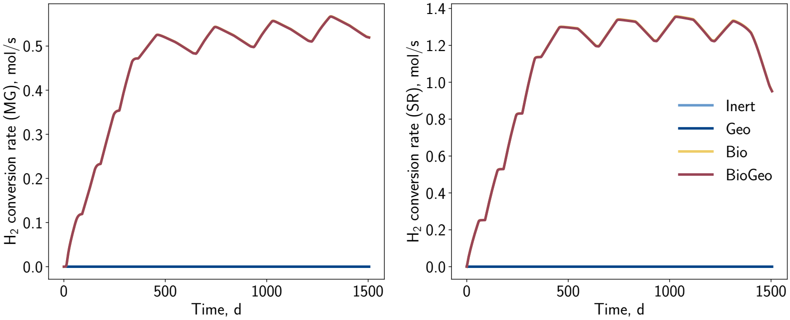

Figure 3.26: Hydrogen conversion rates by the biochemical reactions versus time

that the microorganism populations follow the spatial distribution of hydrogen, and their population density achieves the highest number around the wellbore, as a continuous substrate supply is ensured. This expectation is true for methanogenic archaea, as the injection stream provides the substrates continuously, and it achieves the maximum expected microbial density of $n^*_{\mathrm{max}} = 9265$ (cf. Section 3.3.2.1). Conversely, as sulfate is only considered to be present initially and not generated by an additional source, one of the sulfate-reducing bacteria's substrates becomes progressively limiting. This limitation is visible in the near-wellbore area, where the density of sulfate-reducing bacteria is low after some time. In the wellbore cells, the concentration is at its maximum, as it is drying out ($S_w \to 0$), and the habitat of the microorganisms vanishes.

The start of substrate limitation for the sulfate-reducing organisms is also visible in the conversion rates as depicted in Figure 3.26. During the conversion phase, the reaction rate increases for both species. During regular operation, the spatial extent of the hydrogen cushion only grows slowly (mainly gas-gas mixing by molecular diffusion), yielding only small variances in growth rate later on. The substrate becomes progressively depleted during the last cycle for the sulfate-consuming organisms, indicated by a substantial drop.

During the operation, the injected hydrogen is distributed in the system. Partially, it will be reproduced, converted, and also remain in storage. Figure 3.27 displays this distribution for the case BioGeo, where all reactions are considered. The storage operation is clearly visible together with the step-wise behavior in hydrogen injected and produced. As the presence of the reactions is independent of the operation rates, the reactions occur continuously,

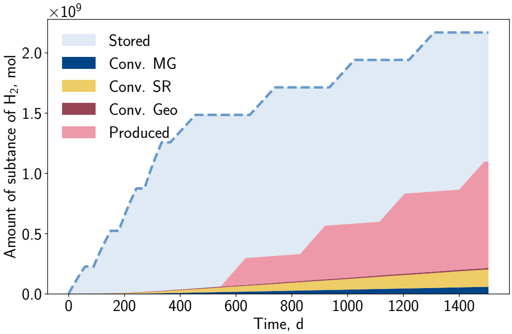

Figure 3.27: Distribution of hydrogen in the system versus time for case BioGeo

leading to a progressive hydrogen loss. Due to the high amounts of hydrogen introduced during the conversion phase and the consecutive injection and withdrawal rates being balanced, it is expected that after four storage cycles, a large portion of the total injected hydrogen ($\approx 49.4\,\%$) remains in the formation. Another $40.7\,\%$ of the injected hydrogen is recovered during the four production periods. The remaining part ($\approx 9.9\,\%$) is a permanent loss of hydrogen caused by chemical reactions.

The share of consumed hydrogen for each chemical reaction is depicted in Figure 3.28. Here, the previously mentioned dominance of sulfate reduction ($6.6\,\%$) over methanation ($2.7\,\%$) and pyrite-to-pyrrhotite reduction ($0.6\,\%$) is

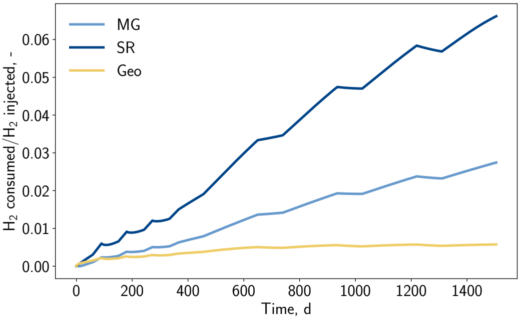

Figure 3.28: Fraction of consumed hydrogen by bio- and geochemical reactions over the injected hydrogen amount versus time for case BioGeo

evident. Nevertheless, the shares of sulfate reduction and pyrite-to-pyrrhotite reduction are expected to decrease due to substrate limitation and reaching overall equilibrium, respectively.

In addition to the field data, it is essential to consider some general simulation parameters while analyzing the simulation results. A common method for assessing the accuracy of the simulation involves determining the material balance error for each time step. This error arises from the numerical approximation and should be sufficiently small. The discretization scheme also influences the magnitude of the error. The FV method is locally and globally mass conservative and typically results in minor errors. In contrast, non-mass conservative discretization schemes, such as the FD method, tend to exhibit higher errors. In this study, the global material balance error (MBE) for the hydrogen component is evaluated:

$$\mathrm{MBE}_{\mathrm{H}_2} = \sum_i I^{t}_{\mathrm{H}_2,i} - \sum_i I^{t+1}_{\mathrm{H}_2,i} - \sum_i q^{t+1}_{\mathrm{H}_2,i} V_i \Delta t \tag{3.52}$$

where $\mathrm{MBE}_{\mathrm{H}_2}$ is the material balance error in mol, $\sum_i$ is the sum over all grid cells, I is the inventory in mol, q_{H_2} is the source/sink term ($q_{\mathrm{H}_2} = q^{\mathrm{H}_2}_{\mathrm{well}} + q^{\mathrm{H}_2}_{\mathrm{bio}} + q^{\mathrm{H}_2}_{\mathrm{geo}}$) in mol/(s $\cdot$ m^3), V_i is the volume of the grid cell i in m^3, and Δt is the time step size in s.

The inventory $I_{\mathrm{H}_2,i}$ which corresponds to amount of substance in the grid cell i can be determined by:

$$I_{\mathrm{H}_2,i} = \phi_i V_i \sum_{\alpha=g,w} \varrho_\alpha c^{\mathrm{H}_2}_\alpha S_\alpha \tag{3.53}$$

Figure 3.29 illustrates the material balance error for the inert case and the scenario involving all reactions. As the hydrogen content in the storage formation increases, the material balance error also grows. However, the positive and negative errors balance over time, preventing the error from amplifying. At any given time, the material balance error for hydrogen ($|\mathrm{MBE}_{\mathrm{H}_2}|$) remains below $9.2 \cdot 10^{-6}$ mol, corresponding to a relative error of less than $10 \cdot 10^{-11}$, which is deemed acceptable.

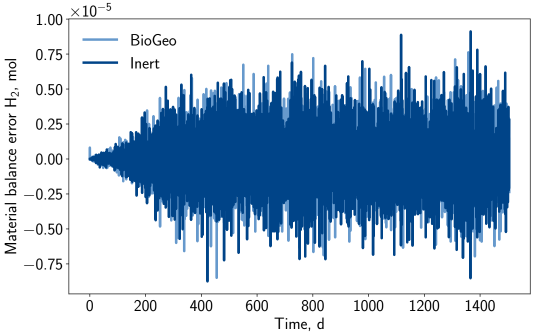

Figure 3.29: Material balance error for the inert and reactive case versus time

In addition, the simulation run time is an essential criterion, which ranged from 21.25 hrs for the inert case to 29.27 hrs for case BioGeo, both ran on four cores (Intel® Core™ i7-12700, 32 GB DDR4 RAM). The relatively high simulation time was influenced by a relatively small maximum time step size, $\Delta t_{\mathrm{max}} = 0.5\,\mathrm{d}$, which is considered more than sufficient. However, activating the chemical reactions appears to increase the simulation time by a factor of approximately 1.4 compared to the base case.

3.4.3. Summary

The field-scale simulations in DuMu$^\mathrm{x}$ show great potential for application in UHS. The observations from the laboratory scale regarding chemical reactions were also observed in the field-scale simulations, with a noticeable impact on the reproduction of stored hydrogen. Approximately 10 % of the hydrogen was converted by the reactions. The gas composition during production can serve as an indicator of reactions taking place. However, even without bio- and geochemical reactions, the fluid composition behaves dynamically due to progressive gas-gas mixing with cushion gas, leading to a reduced hydrogen fraction in the withdrawn gas over time. Increasing the amount of injected hydrogen during the conversion phase could temporarily compensate for the varying withdrawal concentrations. Comparing the general parameters of the simulations indicates that chemical reactions extend the simulation runtime but have no significant impact on the material balance error.

3.5. Conclusions and outlook

- The mathematical model describing the bio-reactive transport process in DuMu^x was extended to incorporate geochemical reactions, resulting in a versatile model that captures both bio- and geo-reactive transport processes during UHS.

- The calibration of the DuMu^x implementation involved multiple steps. Firstly, based on 32 experiments with reference and actual storage core samples, empirical correlations for molecular diffusion were developed for the binary system hydrogen-methane. These correlations were successfully implemented in DuMu^x, reproducing the experimental data with satisfying accuracy. Secondly, one biochemical reaction was calibrated using a batch experiment, adapting growth parameters directly in DuMu^x. Lastly, the reduction of pyrite to pyrrhotite, which produces harmful hydrogen sulfide, was calibrated based on reactor experiments from the literature. Due to limited data, a kinetic rate model was developed, providing satisfying accuracy in reproducing hydrogen sulfide production.

- The developed bio-geo-reactive transport model was implemented for a benchmark scenario on a semi-artificial geological structure. Simulations of a simplified UHS operation, including conversion and consecutive storage cycles, revealed permanent hydrogen losses due to reactions and temporary losses induced by gas-gas mixing with the initial and cushion gas. Approximately 10 % of the injected hydrogen was converted by reactions, and an increasing share of cushion gas was detected in the withdrawal stream, indicating gas-gas mixing. Indicators for specific reactions were identified based on the composition of the production gas, allowing for insights into potential risks.

- The calibration of the model primarily relies on laboratory observations, and while this already offers a necessary scientific foundation, the transfer from laboratory to field scale remains a critical step. Real field tests are necessary to further develop and validate the model in a realistic subsurface environment.

Chapter 4

Extension of UHS field-scale simulation on CVFE method to allow for the modeling of mechanical dispersion

During the storage of hydrogen in the subsurface, the mixing with the initial gas is a critical aspect that can result in temporary hydrogen losses during operation. This interaction is influenced by molecular diffusion and mechanical dispersion. The following chapter presents the extension of the implementation in DuMu$^{\text{x}}$ by the transport process of mechanical dispersion for the two-phase n-component transport. Since the velocity field is required to determine the contribution of mechanical dispersion, the previously used cell-centered FV method is inadequate. Hence, the CVFE method was employed for the simulation, leading to requirements in gridding and additional implementations. The developed workflow was subsequently applied to predict the operational phase of the *HySTORAGE* field test, initiated and operated by Uniper Energy Storage GmbH.

4.1. Extension of source code and modeling description

Several modifications in the implementation in DuMu$^{\text{x}}$ were required to model the effect of mechanical dispersion: 1) Extension of advective-diffusive flow term by mechanical dispersion for two-phase n-component transport; 2) Development of a workflow for converting existing FV grids to FE method capable meshes to enable the CVFE scheme as discretization method; 3) Due to new discretization method, a new well model in analogy to Voronoi grids needed to be developed and implemented. Besides the requirements for the mechanical dispersion, additional extensions were developed and implemented. An interface for processing dynamic field data, including modification in the adaptive time step manager, was established. Additionally, a new fluid system, including new components, was developed for the simulation of the field test.

The starting point was the implementation of the previous chapter (see Section 3.2) that was once more extended. The new structure is displayed in Figure 4.1, where packages irrelevant for this implementation are removed from the overview. The changes in the transport model and other extensions of this chapter can be found in the previously mentioned persistent repository [65].

4.1.1. Implementation of mechanical dispersion for a two-phase n-component system

As introduced in Chapter 2.1.1.2, the mechanical dispersion encompasses the compositional mixing caused by varying lengths of flow paths and velocities. The phenomena are considered in the mathematical model in the diffusive/dispersive flux term, which can be expressed as follows:

$$J_\alpha^\kappa = -\varrho_\alpha \left(D_{\text{diff},\alpha}^\kappa + D_{\text{disp},\alpha}^\kappa \right) \nabla c_\alpha^\kappa, \quad \alpha = g, w \tag{4.1}$$

For modeling mechanical dispersion, various approaches were developed in the past [11, 105, 128, 130]. Here, the focus was placed merely on the dispersive flux of dilute species in a single phase instead of the more complex multiphase system. An outcome was a general formulation of the dispersion coefficient governed by the velocity field:

$$D_{\text{disp}} = \phi \left(a_{ijkl} \frac{v_i v_j}{\|v\|} \right) \tag{4.2}$$

where D_{disp} is the dispersion tensor in m^2/s, a_{ijkl} is the dispersivity in m, and v is the true velocity field in m/s ($v = u/\phi$).

Consequently, the strength of the mixing is proportional to the flow velocity [130]. For an isotropic medium, the dispersivity is a second-order tensor containing two dispersivities a_L and a_T [11], which are also called longitudinal and transverse dispersivity, respectively. The longitudinal dispersivity acts parallel to the flow direction, while the transversal dispersivity establishes the contribution of the dispersion perpendicular to the main flow direction. As the dispersivity depends mainly on the pore morphology, it is regularly assumed to be a petrophysical property. Based on this assumption, Scheidegger [130]

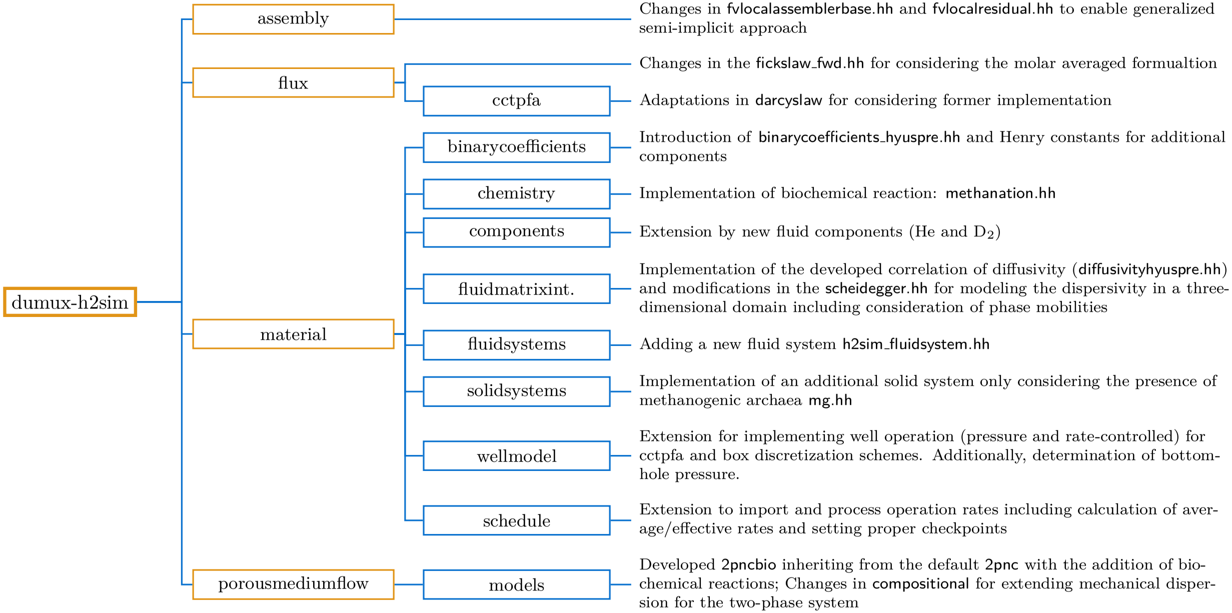

Changes in fvlocalassemblerbase.hh and fvlocalresidual.hh to enable generalized semi-implicit approach

Changes in the fickslaw_fwd.hh for considering the molar averaged formualtion

Adaptations in darcyslaw for considering former implementation

Introduction of binarycoefficients_hyuspre.hh and Henry constants for additional components

Implementation of biochemical reaction: methanation.hh

Extension by new fluid components (He and D_2)

Implementation of the developed correlation of diffusivity (diffusivityhyuspre.hh) and modifications in the scheidegger.hh for modeling the dispersivity in a three-dimensional domain including consideration of phase mobilities

Adding a new fluid system h2sim_fluidsystem.hh

Implementation of an additional solid system only considering the presence of methanogenic archaea mg.hh

Extension for implementing well operation (pressure and rate-controlled) for cctpfa and box discretization schemes. Additionally, determination of bottom-hole pressure.

Extension to import and process operation rates including calculation of average/effective rates and setting proper checkpoints

Developed 2pncbio inheriting from the default 2pnc with the addition of biochemical reactions; Changes in compositional for extending mechanical dispersion for the two-phase system

Figure 4.1: Extensions and adaptations in comparison to the initial DuMu^x structure [86]

suggested the dispersivity of a porous media in the following form:

$$a_{ijkl} = a_T \delta_{ij}\delta_{kl} + \frac{a_L - a_T}{2}(\delta_{ik}\delta_{jl} + \delta_{il}\delta_{jk}) \tag{4.3}$$

where δ is the Kronecker delta.

Inserting Eq. 4.3 in Eq. 4.2, and considering a Cartesian coordinate system, the dispersion coefficient can be expressed as follows [130]:

$$D_{\text{disp}} = \phi \left(\|v\| a_T + \frac{vv^T}{\|v\|} (a_L - a_T) \right) \tag{4.4}$$

While the previously presented models were developed for diluted species in a single-phase system, the formulation can be extended for the multiphase system:

$$D^{\kappa}_{\text{disp},\alpha} = \phi S_\alpha \left(\|v_\alpha\| a_T + \frac{v_\alpha v_\alpha^T}{\|v_a\|} (a_L - a_T) \right) \tag{4.5}$$

where the index a indicates the corresponding parameters of the phase.

In DuMu$^{\text{x}}$, the dispersive flux of a diluted species was previously implemented for the single phase system (cf. Eq. 4.4). Consequently, the source code of the 2pncbio model (see Section 3.1 excluding geochemical reactions) was extended for the multiphase system as presented in Eq. 4.5 in this study.

4.1.2. Workflow of modification from non-conforming to conforming mesh

With the increasing interest in numerical simulations, various grid types were developed within the last decades coming with their individual advantages but also requirements. Within the field of reservoir engineering, corner-point grids were developed in the late 1980s [121] and since then have become the industry standard for field-scale simulations. Corner-point grids are often referred to as pillar grids due to their appearance. Each cell is parameterized with the global coordinate triplet (i, j, and k) representing the three dimensions [121]. The spatial extension of each cell is then defined by eight corners (global or local coordinate system) setting up pillars. Each cell has six faces, and the resulting grid counts as a structured grid due to its logical arrangement. Overall, corner-point grids allow excellent adaptability for reproducing the geometry of a geological formation, layering, and faults [121]. Special issues can appear during pinch-outs (layers are vanishing) due to the logical arrangement of cells. The corner-point grid shows its full potential for spatial discretization methods where the unknowns are located in the center of the cell, such as FD and FV methods. However, for schemes where the unknowns are located on the nodes/corners (e.g. FE method), these grids are not applicable as the connectivity between the nodes may not be sufficiently defined. Grids, where nodes without connectivity to the corners of the neighboring cell are allowed, are called non-conforming grids (cf. Figure 4.2).

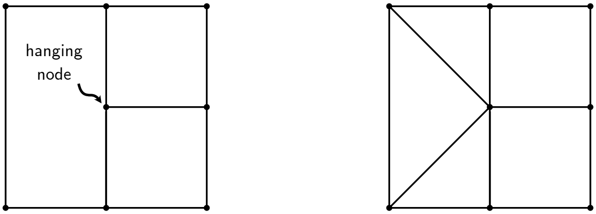

(A) Non-conforming

(B) Conforming

Figure 4.2: Non-conforming versus conforming grids

To apply FE schemes, the non-conforming grid has to be transformed into a conforming mesh type. In the present study, a new grid was meshed based on the geological formation and afterwards parameterized regarding petrophysical properties. For the meshing of the grid, the open-source tool Gmsh [49] was used because it possesses a large variety of grid geometries and types, mainly focusing on the FE method. Additionally, it comes with straightforward methods for grid refinements (globally and locally) and can be handled within DuMu$^\text{x}$ using the Dune UGGrid grid manager [129]. The shape of the cells was set as prisms with a triangular base, allowing the main flux (horizontally) to be almost perpendicular to the faces. The resulting grid is an unstructured mesh without logical arrangement but a conforming grid fulfilling the requirements that were striven for. The general workflow of gridding was composed of five steps:

1. Export of sampled surfaces from the geological model (e.g. from SLB Petrel), followed by reading in the coordinates of points in surface (x, y, and z) within the script.

2. Based on input resolution (r_{domain}) distribution of points on surface (OpenCASCADE) with the subsequent definition of boundary by closing the outer loop.
3. Transposition of the surface by the thickness of the layer.
4. Meshing with Gmsh between the defined points (resolution sensitive).
5. Parameterize the new grid with petrophysical properties by using nearest neighbor interpolation.

The workflow for grid generation, applied to the specific field case, was realized in a Python script accessing the Gmsh API and producing a grid that satisfies the requirements of the CVFE method. Figure 4.3 presents an overview of the relevant grids used in this study. The results successfully replicate the original domain, and petrophysical properties are accurately transferred. Since the initial domain has a coarser discretization than the resulting one, the former grid pattern is identifiable on the final grid. However, diffusive and dispersive flow processes demand a relatively fine spatial and temporal discretization resolution to suppress contributions of numerical diffusion/dispersion. For this specific case, a local fine grid is introduced where hydrogen is expected during operation (wellbore region). The refinement was implemented by adjusting the resolution radially around the wellbore in the second step of the workflow. A triangular base plane allows a smooth transition from the wellbore region to the rest of the domain.

4.1.3. Extension of Peaceman well model for CVFE method

Within numerical simulations on a field scale, the dimensions of the well are inevitably smaller than the spatial discretization. This leads to the issue of determining the representative bottom-hole pressure present at the wellbore. Typically, two options to determine the bottom-hole pressure are commonly applied: 1) Local grid refinement, which resembles the wellbore geometry and its vicinity, resulting in a significant increase in computational costs; 2) Introduction of a well model to determine the bottom-hole pressure based on an equivalent/effective wellbore radius [114]. The second approach was selected in this work due to its numerical simplicity and general acceptance in reservoir simulators.

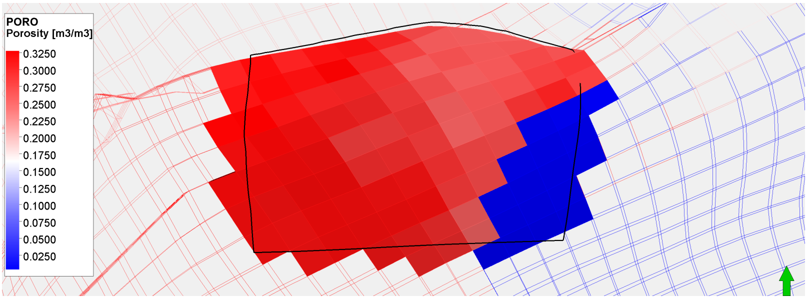

(A) Area of investigation (length: 500 m, width: 290 m to 340 m, and thickness: 2.4 m) - Corner-point grid

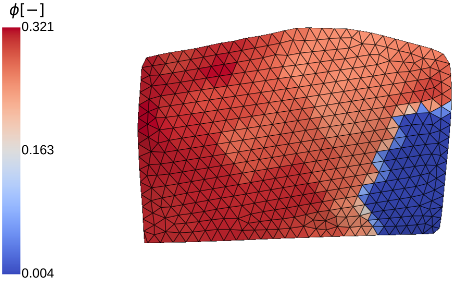

(B) Transformed grid geometry of the area of investigation with the developed workflow (9500 cells)

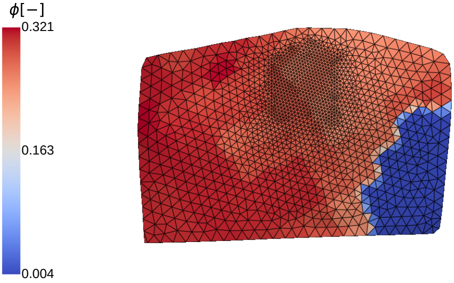

(C) Transformed grid geometry of the area of investigation including a fine grid around the wellbore (31 020 cells)

Figure 4.3: Overview of relevant grids used in the study

Assuming a perfect vertical well, the flow through a horizontal permeable layer to the well is radial and can be vertically extruded over the length of the well (cf. Figure 4.4). Consequently, the well model is often applied for a 2D grid (top-view) and - if required - afterwards averaged over the thickness of the well or evaluated at a particular depth.

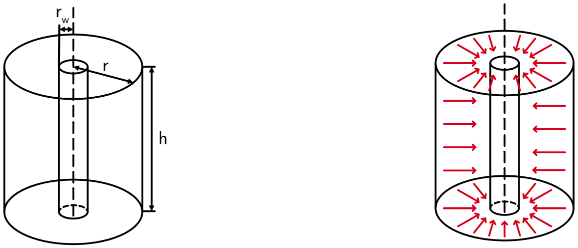

(A) Relevant well parameters (B) Radial flow regimes to a vertical well

Figure 4.4: Schematic representation of an ideal vertical well

A general form of the radial single-phase flow to the well can be expressed as follows [131]:
In terms of pressure drop:

$$p_{\mathrm{BHP}} - p = \frac{q\mu}{2\pi\varrho K h}\left(\ln\left(\frac{r_{\mathrm{eff}}}{r_w}\right) + s\right) \tag{4.6}$$

In terms of flow rate:

$$q = \frac{2\pi\varrho K h}{\mu\left(\ln\left(\frac{r_{\mathrm{eff}}}{r_w}\right) + s\right)}\left(p_{\mathrm{BHP}} - p\right) \tag{4.7}$$

where p_{BHP} is the bottom-hole pressure in Pa, p is the pressure of the well block in Pa, q is the flow rate in mol/s, ϱ is the molar density in mol/m^3, K is the horizontal permeability in m^2, h is the thickness of the grid block in m, μ is the dynamic viscosity in Pa $\cdot$ s, r_{eff} is the effective wellbore radius in m, r_w is the wellbore radius in m, and s is the wellbore skin factor.

The determination of the effective wellbore radius depends on the spatial discretization (see Figure 4.5). For cell-centered FV and FD methods, the well is accounted to penetrated grid cells where the injection and production

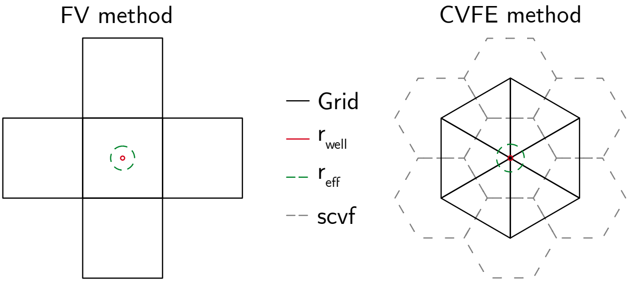

Figure 4.5: Comparison of effective wellbore radius for cell-centered FV and CVFE discretization schemes

are coupled in the source/sink term. For these types of discretization, one popular model is the Peaceman well model [114], which can be expressed for two-dimensional uniform Cartesian grids including an isotropic permeability distribution as follows:

$$r_{\text{eff}} = \frac{e^{-\gamma}}{4}\sqrt{\Delta x^2 + \Delta y^2} \tag{4.8}$$

where γ is the Euler's constant and Δx and Δy are the grid cell lengths in m.

For anisotropic horizontal permeabilities ($K_{xx} \neq K_{yy}$), this term can be extended [115]:

$$r_{\text{eff}} = \frac{e^{-\gamma}}{2}\frac{\left(\Delta x^2\sqrt{K_{yy}/K_{xx}} + \Delta y^2\sqrt{K_{xx}/K_{yy}}\right)^{1/2}}{\left(K_{xx}/K_{yy}\right)^{1/4}\left(K_{yy}/K_{xx}\right)^{1/4}} \tag{4.9}$$

The horizontal permeability K in Eq. 4.6 can be determined as follows:

$$K = (\det \mathbf{K})^{1/2} = \sqrt{K_{xx} \cdot K_{yy}} \tag{4.10}$$

where $\mathbf{K}$ is the permeability tensor.

Contrary to the cell-centered FV scheme, for the CVFE method, the unknowns are located on the grid nodes. This leads to the fact that the well is likewise located on the node, which is associated with more than one element (FE) but within one box (FV). With the assumption of an equilateral triangle shape of the cells from the top, the subcontrol volumes form an ideal hexagon, similar to Voronoi grids. There are existing well models for these types of grids, such as those proposed by Palagi and Aziz [108] or Aavatsmark [1]. According to Aavatsmark [1] for isotropic Voronoi grids, the effective wellbore radius can be calculated based on the following equation:

$$r_{\text{eff}} = \frac{e^{-\gamma}}{4} D \tag{4.11}$$

where D is the length of the diagonals in the hexagonel cells.

For anisotropic distribution of permeabilities, the formulation can be extended as proposed by Aavatsmark [1]:

$$r_{\text{eff}} = \frac{e^{-\gamma}}{2} \frac{\|\mathbf{K}^{-1/2}\mathbf{d}\|_2}{\operatorname{tr}\left(\mathbf{K}^{-1/2}\right)} \tag{4.12}$$

where $\|\cdot\|_2$ corresponds to the Euclidian norm, $\mathbf{K}$ is the permeability matrix in m^2, $\mathbf{d}$ is the length of the diagonals of the hexagonal cells (= FV box) in m, and $\operatorname{tr}(\cdot)$ denotes the trace of a matrix.

With a focus on the CVFE method, the subcontrol volumes of the box containing the well are required to determine the effective wellbore radius. Consequently, Eq. 4.12 can be modified for the calculation of the effective wellbore radius of the subcontrol volume:

$$r_{\text{eff, scv}} = \frac{e^{-\gamma}}{2} \frac{\|\mathbf{K}^{-1/2}(2 \cdot \mathbf{r}_{\text{scv}})\|_2}{\operatorname{tr}\left(\mathbf{K}^{-1/2}\right)} \tag{4.13}$$

where $\mathbf{r}_{\text{scv}}$ is the length of the vector from the well origin to the outer corner of the subcontrol volume (cf. Figure 4.6).

Typically, permeability tensors are defined as a diagonal matrix, which allows the following simplification:

$$\mathbf{K}^{-1/2} = \begin{bmatrix} K_{xx} & 0 \\ 0 & K_{yy} \end{bmatrix}^{-1/2} = \begin{bmatrix} 1/\sqrt{K_{xx}} & 0 \\ 0 & 1/\sqrt{K_{yy}} \end{bmatrix} \tag{4.14}$$

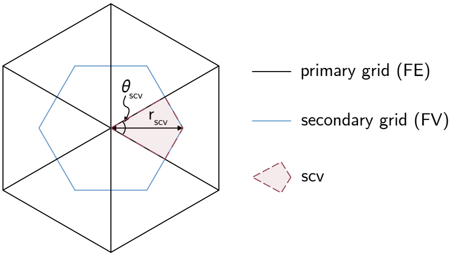

Figure 4.6: Relevant parameters regarding the well model for the CVFE method

Due to the radial flow to the well, a simple averaging in dependency of the connectivity angle (θ_{scv}) of Eq. 4.6 can be performed:

$$p_{\text{BHP, scv}} = p + \sum_{\text{scv}} \frac{\theta_{\text{scv}}}{360°} \cdot \frac{q_{\text{scv}} \cdot \mu_{\text{scv}}}{2\pi \varrho_{\text{scv}} K_{\text{scv}} \cdot h_{\text{scv}} \cdot \left(\ln \left(\frac{r_{\text{eff, scv}}}{r_w} \right) + s \right)} \tag{4.15}$$

where $\sum_{\text{scv}}$ corresponds to the sum over the subcontrol volumes in the box (FV mesh) of the perforated layer.

Assuming a homogeneous distribution of prisms with an equilateral triangular base, every connection angle is equal to 60°. Here, the equation can be simplified and yields:

$$p_{\text{BHP, scv}} = p + \sum_{\text{scv}} \frac{1}{6} \cdot \frac{q_{\text{scv}} \cdot \mu_{\text{scv}}}{2\pi \varrho_{\text{scv}} K_{\text{scv}} \cdot h_{\text{scv}} \cdot \left(\ln \left(\frac{r_{\text{eff, scv}}}{r_w} \right) + s \right)} \tag{4.16}$$

Depending on the spatial discretization, wells often penetrate more than one cell in the z-direction. Here, common approaches are defining a reference depth, taking the first perforated layer, or alternatively, the volumetric average to determine a representative bottom-hole pressure. The developed implementation in DuMu$^\text{x}$ allows the latter one. The volumetric averaged method can be expressed as follows:

$$p_{\text{BHP, well}} = \frac{1}{V_{\text{well}}} \cdot \sum_{\text{scv}} p_{\text{BHP, scv}} \cdot V_{\text{scv}} \tag{4.17}$$

where V_{well} is the total volume of cells penetrated by the well in m^3 and V_{scv} is the volume of the individual subcontrol volumes in m^3.

The realization of the well models for both discretization schemes can be found in `wellmodel.hh` coming with the calculation of the bottom-hole pressure and features to operate the well (pressure- and rate-controlled).

4.1.3.1. Comparison of developed well model with Peaceman well model

After implementing both well models in DuMu^x, a test case was defined to verify the implementation and the outcome of them. The goal was to compare the well models for both discretization methods. For this purpose, a simplified injection and production cycle on an artificial geometry was defined and afterwards compared. The simulation domain represents a cuboid with the dimensions of 1025 m x 1025 m x 20 m. As a reference case, the grid was discretized in 3362 cuboid cells (41 x 41 x 2) for running simulations with the cell-centered FV method. For testing the implementation of the well model for the CVFE method, the grid was discretized using Gmsh [49] into 5056 cells composed of prisms with triangular base area. An overview of the grids is depicted in Figure 4.7. The porosity was parameterized homogeneously to 20 %. In the first step, the horizontal permeabilities were defined identically to 200 mD ($k_{zz} = 20\,\mathrm{mD}$), followed by the reduction of the permeability in the y-direction ($K_{yy} = 0.5 \cdot K_{xx}$) as an additional anisotropic test case. The initialization was performed based on a hydrostatic equilibrium, and the lateral boundaries were set as Dirichlet boundaries based on the initial values. The operation schedule was defined as 20 days of injection, 20 days of shut-in, 20

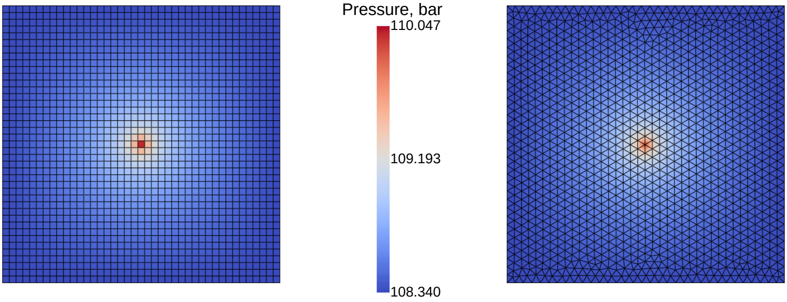

Figure 4.7: Grids used to compare the well model implementations for cell-centered FV and CVFE method (here: gas phase pressure distribution during the injection)

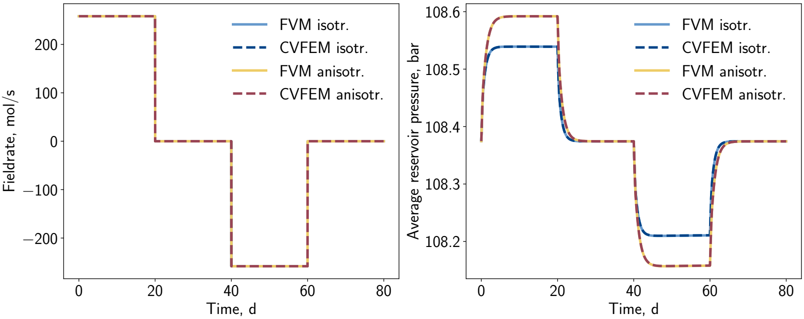

Figure 4.8: Field parameters of the well model test case

days of production, and 20 days of shut-in. The rate was selected identically for production and injection with $5 \cdot 10^5\,\mathrm{Sm}^3/\mathrm{d}$. Figure 4.8 shows the relevant field parameters of field rate and average reservoir pressure. Generally, the pressure response of the reservoir is reasonable as the pressure increases during injection, decreases during production, and approaches the initial pressure during the idle phase due to set Dirichlet boundary conditions laterally. Both discretization methods lead to almost identical results regarding the pressure feedback of the operation. Figure 4.9 presents the results of the bottom-hole pressure calculated with the implemented well models. It is expected that the bottom-hole pressure is significantly higher than the average reservoir pressure during injection, while in the case of production, the bottom-hole pressure is lower than the average one. In the case of the anisotropic perme-

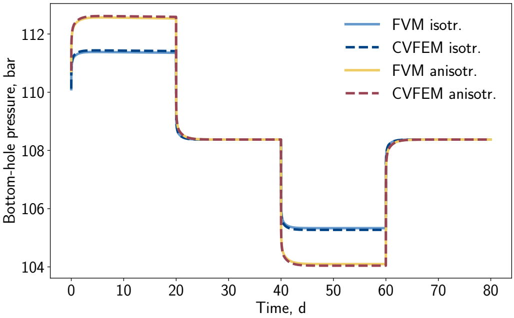

Figure 4.9: Bottom-hole pressure versus time of the well model test case

ability distribution, the bottom-hole pressure is higher than in the isotropic case, which is reasonable due to the reduced permeability in the y-direction. Nevertheless, both well models lead to congruent results for the isotropic and anisotropic permeability distribution. Only a minor deviation in the range of approximately 50 mbar can be observed. Overall, this leads to a satisfying result, implying that both well models and their implementations lead to an equivalent outcome and can be assumed as verification.

4.1.4. Operation schedule implementation for actual field data

The operation of a UGS depends on the supply and demand of the stored fluids, making it a dynamic process. Typically, injection and withdrawal rates are averaged daily and can vary significantly. An example of the fluctuations in rates in a UGS during a year is depicted in Figure 4.10.

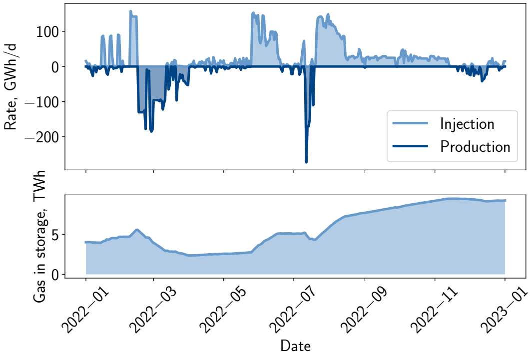

Figure 4.10: Operation of the UGS Bierwang within the year 2022 according to the GIE database [45].

Regarding simulation, the observed data frequency often does not align with the simulated discrete points in time, as the time step size behaves dynamically during the simulation. Typically, the time step sizes are selected adaptively, starting with an initial time step size, which is adjusted depending on the convergence of the Newton iterations. With good convergence, the time step size increases, while a high number of iterations leads to a reduction in time step size. Figure 4.11 depicts an arbitrary dynamic rate profile contain-

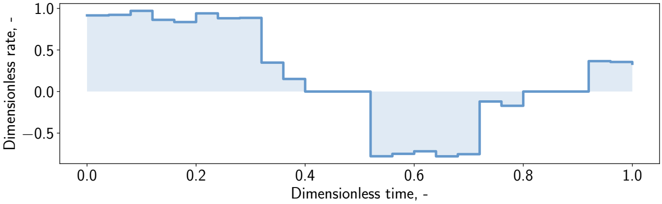

(A) Arbitrary rate profile including injection (+), withdrawal (-), and idle (0) modes

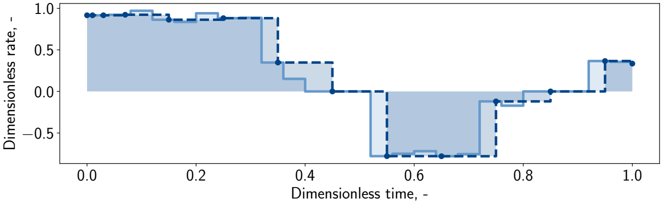

(B) Adaptive time steps without checkpoints and no averaging of rate (number of time steps: $n_{\Delta t} = 14$; relative error: $\eta = 0.132$)

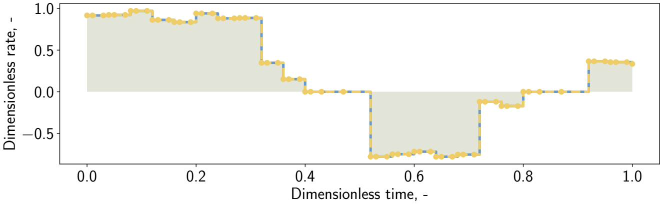

(C) Adaptive time steps including setting checkpoints after a change in rate ($n_{\Delta t} = 66$; $\eta < 1 \cdot 10^{-10}$)

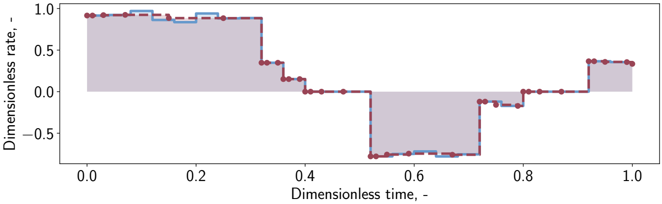

(D) Adaptive time steps including checkpoints at a change in operation mode and change of rate by a factor δ_q and averaging of rate s ($n_{\Delta t} = 34$; $\eta < 1 \cdot 10^{-10}$)

Figure 4.11: Overview of different possibilities of time stepping. For all cases, adaptive time stepping is used with an initial time step size of $\Delta t_{init} = 0.01$ which is doubled until reaching the maximum time step size of $\Delta t_{max} = 10 \cdot \Delta t_{init}$

ing different methods of regulating the time step sizes. For the particular case, simple adaptive time stepping, including a maximum time step size, leads to 14 time steps; however, the relative error concerning the cumulative injected rate is significant (cf. Figure 4.11B). Forcing a congruent simulation time with the observed time leads to a total of 66 time steps (cf. Figure 4.11C). Thus, the increased number of time steps will lead to a substantial increase in computation cost. To reduce these costs, one solution is averaging the rates by calculating cumulative rates and setting checkpoints only at remarkable changes in rate.

The cumulative rate Q within an arbitrary time interval $[t_0, t_1]$ is defined as the integral of the rate with respect to time:

$$Q(t) = \int_{t_0}^{t_1} q(t)\mathrm{d}t \tag{4.18}$$

where the rate q is in mol/s or Sm^3/s, and the time t is in s.

Assuming a discretely observed data set with a data frequency of Δt_{obs} and a time-dependent rate $q(t)$, the cumulative rate corresponds to:

$$Q(t_{i,\mathrm{obs}}) = \int_{0}^{t_{i,\mathrm{obs}}} q(t)\mathrm{d}t = \sum_{k=1}^{i} q_k \Delta t_{k,\mathrm{obs}} \tag{4.19}$$

Looking at an arbitrary point in time $t \in t_{\mathrm{obs}}$, the cumulative rate can be calculated as follows:

$$Q(t) = \int_{0}^{t_{i,\mathrm{obs}}} q\mathrm{d}t + \int_{t_{i,\mathrm{obs}}}^{t} q\mathrm{d}t = Q(t_{i,\mathrm{obs}}) + (t - t_{i,\mathrm{obs}})\, q_{i+1} \text{ with: } t_i < t < t_{i+1} \tag{4.20}$$

The effective rate for an arbitrary time step i in the simulation can be determined with:

$$q(t_i) = \frac{Q(t_{i+1}) - Q(t_i)}{t_{i+1} - t_i} \tag{4.21}$$

In general, this formulation is mass-conservative; nevertheless, it does not properly mimic the type of operation (injection, withdrawal, and idle). To ensure that the operation mode is maintained, checkpoints in the simulation can be introduced to force a time step to end. Potential criteria for a checkpoint are: 1) a change in the operation mode, 2) changes in injection concentration, and 3) a deviation (Eq. 4.22) of injection/withdrawal rate of more than a factor δ_q^{lim} (default: 0.5).

$$\delta_{q_i} = \frac{|q_{i-1} - q_i|}{q_{i-1}} \tag{4.22}$$

To improve the numerical stability, after passing a checkpoint, the time step size can be reduced to the initial time step size. Overall, this leads to a reasonable mix of relative error and number of time steps (cf. Figure 4.11D).

The implementation of the averaging of rates combined with dynamic time step sizes depending on the operation schedule was realized in DuMu$^{\mathrm{x}}$ in the present study. The corresponding class and method can be found in `schedule.hh`. Furthermore, an interface allowing the import of schedules (.JSON format) containing rates, pressures, and varying compositions grants a straightforward implementation of complex operation scenarios in DuMu$^{\mathrm{x}}$.

4.1.5. Modifications of the fluid model

For the modeling of the UHS field test, a new fluid system was developed (`h2sim_fluidsystem.hh`). The fluid system consists of nine components (H_2O, CH_4, CO_2, H_2, N_2, C_2H_6, C_{3+}, D_2, and He), which are either present initially or later introduced during the operation. The fluid system is based on the previous implementation (see Section 3.2.2) regarding thermodynamic property modeling. This study assumed no bio- and geochemical reactions, although the biochemical reactions can be activated for future matching procedures.

4.2. Numerical simulation of UHS field test

After developing the numerical model, including the extensions of the transport model and fulfilling the spatial discretization requirements, the implementations were employed to simulate the field test. Before the field test simulation, the recent field history was matched in DuMu^{x} to tune the model. Subsequently, the model was applied for initial predictions regarding the field test in *HySTORAGE*. This field test is conducted in a depleted gas field in Bavaria, Germany. The target formation for the UHS field test is a small gas-bearing horizon located above the primary storage. In three phases, different natural gas blends with increasing hydrogen concentrations will be injected (5 %, 10 %, and 25 % H_2) and after a shut-in period withdrawn. Each sub-test is composed of approximately 30 days of injection, 90 days of shut-in, and 30 days of production. Additionally, helium and deuterium as tracer species are added to the gaseous phase, concluding the transport process and potential biochemical reactions.

In this study, the first operation cycle (5 % H_2) based on the previously developed model was predicted. For this purpose, a cropped section of the geological model that partially contains the gas cap of the target formation was applied to the developed workflow for grid transformation (see Section 4.1.2). The boundaries were defined to reproduce the remaining gas cap outside of the simulation domain. For the calibration, the recent history of this formation was matched within an iterative process. Afterwards, the planned operation schedule of the field test was implemented, and first predictions were performed, focusing on gas-gas mixing by mechanical dispersion.

4.2.1. History match of recent field operation

The target layer is a depleted gas formation located above the main storage formation that has remained mainly idle in recent times, and only a few field data are available. To tune the model, the last production period and the consecutive pressure build-up from the target formation were selected and reproduced in DuMu^{x}.

4.2.1.1. Static model and initialization

For the history match, the simplified coarse grid depicted in Figure 4.12 was used. The grid, composed of 9500 elements (5676 nodes), has a spatial expansion of 500 m x 280 m to 345 m x 10 m (varying depth: $\Delta z = 23\,\mathrm{m}$). The petrophysical properties were obtained from the most recent history match in SLB Eclipse provided by the storage operator. The grid was initialized according to the hydrostatic equilibrium based on a reference pressure of 110 bar at a reference depth of 1000 m. It is assumed that the grid is entirely in the gas zone so that the water saturation is initially at its connate saturation. According to the hydrostatic and thermodynamic equilibrium, the primary variables are calculated based on the following equations:

$$p_w = p_{\mathrm{ref}} - \rho_g g \left(d_{\mathrm{ref}} - d\right) \tag{4.23}$$

$$S_g = 1 - S_{wc} \tag{4.24}$$

$$c_w^\kappa = c_g^\kappa \left(1 - \frac{\varphi_w^{\mathrm{H_2O}} p_w}{p_g}\right) \frac{p_g}{\varphi_w^\kappa p_w} \tag{4.25}$$

where p_{ref} is the reference pressure in Pa, ρ_g is the density in kg/m^3, g is the gravitational acceleration in m/s^2, d_{ref} is the reference depth in m and d is the depth of the element/node in m. Focusing on the definition of the chemical components, φ_w^κ represents the liquid fugacity coefficient of component κ in the aqueous phase.

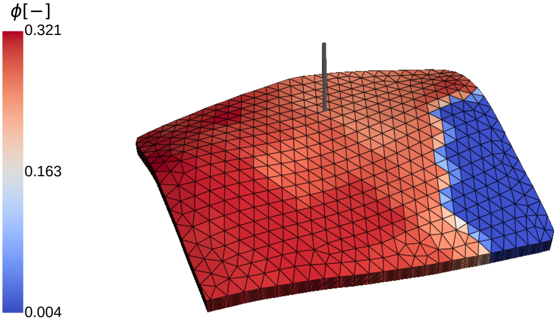

Figure 4.12: Coarse grid used for the history match with the corresponding well

Table 4.1: Initial gas composition in the storage formation in molar percent

Component	Initial
Methane (CH_4)	95.933
Ethane (C_2H_6)	1.259
Pseudo comp. (C_{3+})	1.223
Hydrogen (H_2)	0.000
Carbon dioxide (CO_2)	0.139
Nitrogen (N_2)	1.427
Helium (He)	0.019
Sum	100.000

The initial fluid composition of the gas cap is based on recent gas composition measurements of the injection and withdrawal well of the field test (cf. Table 4.1) and distributed along the phases according to the thermodynamic equilibrium.

4.2.1.2. Matching procedure & results

Focusing on the history match, the observed bottom-hole pressure (memory gauge) in the operation well was matched. Consequently, the production rates (rate-controlled implementation in DuMu^x) were the input argument for the simulation. Figure 4.13 depicts the measured pressure and the corresponding field rates. A significant pressure drop is visible during production, which progressively recovers after the shut-in. As the simulation domain composes

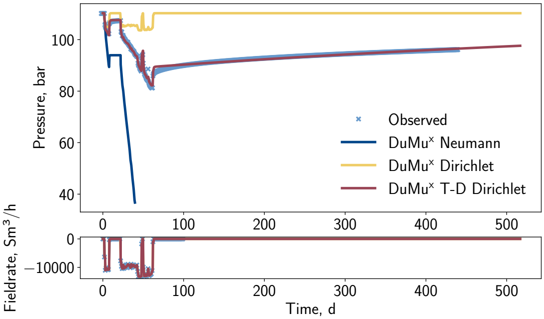

Figure 4.13: Operation history and the simulation results of DuMu^x with varying boundary definitions

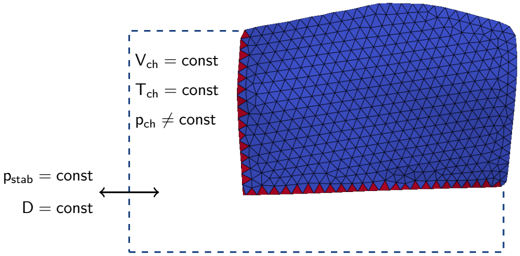

Figure 4.14: Definition of the boundary conditions - Blue corresponds to Neumann (no flow) boundary and red implies Dirichlet boundaries

only a small part of the storage formation and the gas cushion's extent exceeds these limits, the remaining gas cap was considered in the boundary conditions. The first simulation runs with typical boundary conditions showed insufficient matches (cf. Figure 4.13): Selecting a no-flow Neumann boundary at all sides leads to a significant pressure drop not fitting the observed data. The gas cap is limited to the domain size for this boundary type. In contrast, defining constant Dirichlet boundaries at lateral bounds results in the opposite. Assuming that the initial values at these boundaries persist during the entire simulation time induces an instant pressure recovery after shutting in the well. A time-dependent Dirichlet boundary was introduced to dynamically model the appending gas cap's size. For this purpose, a tank representing the exterior gas cap is located around the southwest part of the formation, containing a constant volume but variable pressure influenced by the flux over the boundary (cf. Figure 4.14). The primary values at the corresponding boundaries were defined according to the initialization method but with varying reference pressure p_{ref} in dependency on time (cf. Eq. 4.23).

To determine the variable pressure, the gas cap was modeled. Here, a simple material balance for the gas cap can be established:

$$I_{GC}^{t+1} = I_{GC}^{t} - Q_{\Gamma_D}^{t} \tag{4.26}$$

where I_{GC}^{t+1} and I_{GC}^{t} are the inventories in the gas cap in mol of the current and the previous time step, respectively. Q_{Γ}^{t} is the cumulative flux over the Dirichlet boundaries within a time step in mol.

The inventory of the gas cap can be determined by the real gas law:

$$I_{GC}^{t}=\frac{p_{GC}^{t}V_{GC}}{RT_{GC}Z_{GC}^{t}} \tag{4.27}$$

where p_{GC} corresponds to the reference pressure in the gas cap in Pa, V_{GC} is the constant gas cap volume in m^3, R is the universal gas constant in $\mathrm{J/(mol\cdot K)}$, T_{GC} is the isothermal temperature in K, and Z_{GC}^{t} is the compressibility factor of the gas cap.

Assuming a neglectable material balance error, the cumulative flux over the boundaries within a time step is approximated by calculating the following material balance:

$$Q_{\Gamma_D}^{t}=\sum_{i}I_i^{t}-\sum_{i}I_i^{t+1}-\sum_{i}q_i^{t+1}V_i\Delta t \tag{4.28}$$

where q_i is the source/sink term (e.g. well) in $\mathrm{mol/(m^3\cdot s)}$ in the grid cell i, V_i is the volume of element i, and Δt is the time step size in s.

Consequently, the new reference pressure of the gas cap can be determined in an iterative process due to the pressure dependency of the compressibility factor: $Z_{GC}^{t+1}\left(p_{GC}^{t+1}\right)$:

$$p_{GC}^{t+1}=\frac{I_{GC}^{t+1}RT_{GC}Z_{GC}^{t+1}}{V_{GC}} \tag{4.29}$$

Furthermore, to match the progressive pressure build-up during the shut-in period, an additional term similar to an aquifer model was introduced in Eq. 4.26:

$$I_{GC}^{t+1}=I_{GC}^{t}-Q_{\Gamma_D}^{t}+D(p_{GC}^{t}-p_{\mathrm{stab}})\Delta t \tag{4.30}$$

where D is a damping factor in $\mathrm{mol/(Pa\cdot s)}$ and p_{stab} is the stabilized pressure in Pa, which corresponds to the initial reference pressure used during the initialization.

Consequently, the reference pressure acts as a variable input argument for the initialization method, realizing a time-dependent pressure at the lateral boundary. Concerning the matching, varying the gas cap volume was used to

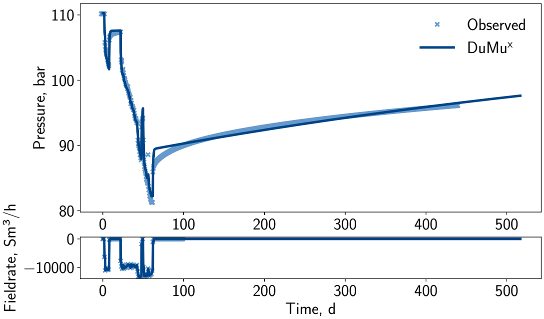

Figure 4.15: History match of the recent operation of the target formation including the observed and best match with DuMu^x

control the short-term pressure increase, while modifications of the damping factor tuned the long-term pressure behavior.

The final result of the match was achieved as depicted in Figure 4.15. For the best match, an initial reference pressure and stabilized pressure of $p_{\text{ref}}^{\text{init}} = p_{\text{stab}} = 110\,\text{bar}$ at a depth of $1000\,\text{m}$ was defined. The volume of the appended gas cap was set to $V_{GC} = 4 \cdot 10^5\,\text{Sm}^3$ and the damping factor for the long-term pressure built-up showed satisfying results for $D = 1 \cdot 10^{-6}\,\text{mol}/(\text{Pa} \cdot \text{s})$. After passing the matching process, the simulation was extended until the start point of the hydrogen injection phase to obtain the corresponding reference pressure (at the end of history match: $p_{\text{ref}}^{\text{end}} = 97.37\,\text{bar}$).

An additional simulation run on the finer grid, which was later used for the prediction, was performed to confirm congruent results during the history match.

4.2.2. Prediction of UHS field test

After passing the history match, the first operation phase of the field test was modeled. Focusing on the effect of mechanical dispersion, three simulation runs were performed where the dispersivities varied from $0\,\text{m}$ to $1000\,\text{m}$ to observe the impact on the mixing.

4.2.2.1. Static model and initialization

The used simulation domain has the exact spatial dimensions of the history match, but the grid resolution (cf. Figure 4.16) was increased. The domain comprises 31 060 cells and 17 543 nodes, including the grid refinement around the well. The petrophysical properties were selected in analogy to the history match, and the initialization was performed identically to the history match as well. Since the prediction starts immediately after the history match, the reference pressure was set to the final reference pressure of the history match. This step is durable, as it is assumed that the spatial domain is entirely in the gas cap and no injection with varying gas compositions occurred within the recent history (e.g. injection of dry gas could dry out cells around the wellbore).

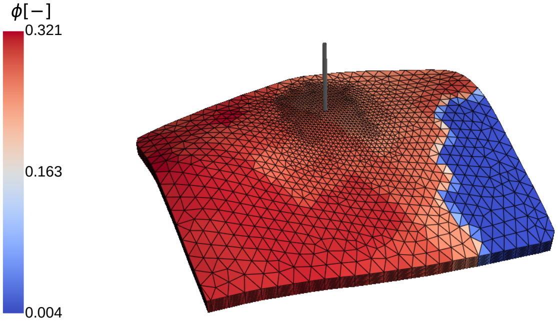

Figure 4.16: Simulation domain used for the prediction with the well

4.2.2.2. Operation schedule

The UHS field test consists of three phases with progressively increasing hydrogen concentrations (5 % to 25 % H_2) with additional tracer species (deuterium (D_2) and helium (He)). In this study, only the first phase of operation was predicted. The schedule comprises three weeks of injection ($q_{\text{inj}} = 1500\,\text{Sm}^3/\text{hr}$) followed by a shut-in period. After an idle period of 90 days, the stored gas is withdrawn at a rate of $q_{\text{pro}} = 1500\,\text{Sm}^3/\text{hr}$. While the injection is limited to 8 hrs per day of operation due to the hydrogen supply by trucks, production can be conducted continuously. Additionally, the operation is stopped for two days every week. Table 4.2 depicts the injection gas composition. The hydrogen and tracers are blended with natural gas and injected into the formation through a single-well configuration.

Table 4.2: Injection fluid compositions during the first phase in molar percent

Component	1^{st} week	2^{nd} week	3^{rd} week
Methane (CH_4)	93.553	93.800	93.800
Ethane (C_2H_6)	0.088	0.093	1.119
Pseudo comp. (C_{3+})	0.095	0.096	0.096
Hydrogen (H_2)	5.000	5.000	5.000
Carbon dioxide (CO_2)	0.063	0.063	0.063
Nitrogen (N_2)	0.695	0.697	0.697
Helium (He)	0.505	0.255	0.255
Deuterium (D_2)	$1.19 \cdot 10^{-3}$	$1.19 \cdot 10^{-3}$	$1.19 \cdot 10^{-3}$

4.2.2.3. Results & Discussion

Figure 4.17 illustrates the planned operation rates of the first phase and the simulated bottom-hole pressure of the operation well. As the rate is averaged per day, the injection rate (planned for only 8 hrs per day) corresponds to one-third of the production, where the entire day is produced. Additionally, this averaging leads to the staircase behavior during production, as the first and last day of each week are planned to operate 16 hrs instead of 24 hrs. The operation can be clearly identified regarding the bottom-hole pressure, and

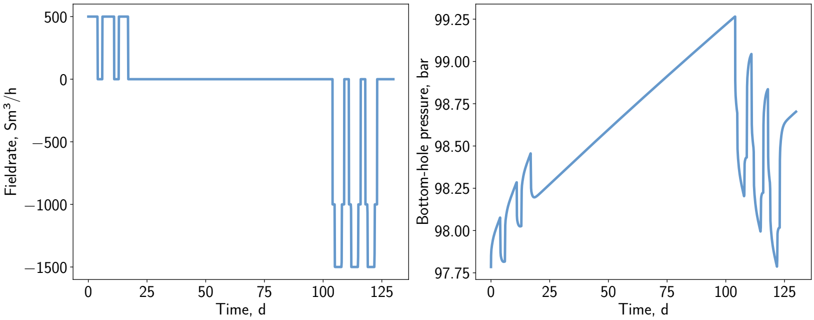

Figure 4.17: Fieldrate and bottom-hole pressure versus time of the prediction

the progressively increasing pressure of the gas cap approaching the initial reservoir pressure can be seen.

Concerning UHS, achieving a high recovery of the stored hydrogen in combination with a stable gas composition is favorable. The gas composition is influenced by the gas-gas mixing with the initial gas. A sensitivity analysis of the dispersivities was conducted to investigate the impact of mechanical dispersion on the spatial distribution of hydrogen inside the formation. The base case considers no dispersivity ($a = 0$), although the effect of numerical dispersion may be present. Additionally, two cases with dispersivities of 1) $a_L = 100\,\mathrm{m}$ and 2) $a_L = 1000\,\mathrm{m}$ were defined. While on the laboratory scale, dispersivities between 0.2 cm to 5 cm were observed [28, 96], the field-scale dispersivities are expected to be orders of magnitudes higher due to large scale heterogeneities [64]. The transverse dispersivity was set to $a_T = 1/20 \cdot a_L$ for all simulations, although its impact is expected to be low due to the radial flow regime.

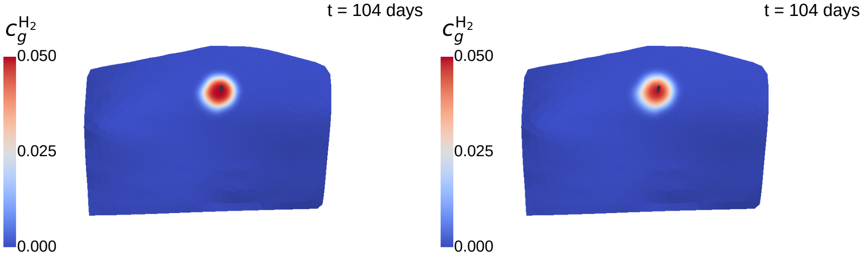

(A) Without dispersion

(B) With dispersion ($a_L = 1000\,\mathrm{m}$)

Figure 4.18: Spatial distribution of hydrogen (mole-fraction in the gaseous phase) recently before the withdrawal period

Figure 4.18 illustrates the hydrogen concentration in the formation. As expected, the highest concentration is observed within the vicinity of the well. However, only minor differences between the presented cases become visible. The divergence between the two cases becomes more obvious, illustrating the absolute difference between the cases (cf. Figure 4.19). The difference is low directly around the well, where the concentrations are close to the injection composition, and far away in the untouched region without hydrogen, where the fluid composition is not affected by the operation. Comparatively more

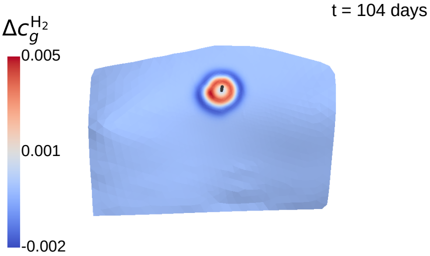

Figure 4.19: Difference of spatial distribution of hydrogen (mole-fraction in the gaseous phase) between the simulations without and with dispersion ($a_L = 1000\,\mathrm{m}$) recently before the withdrawal period

pronounced differences can be observed in the mixing zone. The positive delta around the wellbore indicates that the hydrogen remains closer to the wellbore without dispersion, while the negative implies that the hydrogen penetrates further into the formation with dispersion. This behavior is expected since mechanical dispersion promotes gas-gas mixing.

The varying strength of mixing is also visible in the withdrawal stream composition. Figure 4.20 and 4.21 presents the concentration of hydrogen and helium during the withdrawal phase. The production composition reflects the previous observations but not spatially; instead, it depends on time. In the beginning, fluid from the vicinity of the well is produced, which later originates

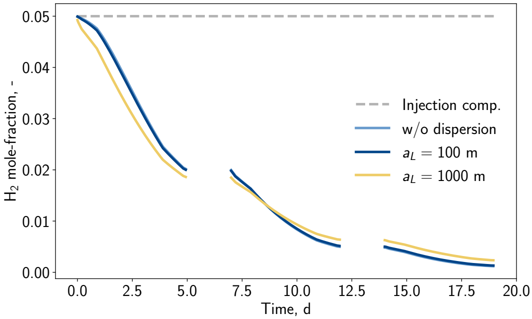

Figure 4.20: Hydrogen mole-fraction in the gas stream during the withdrawal phase

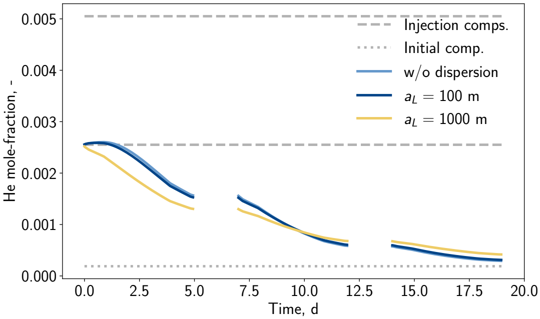

Figure 4.21: Helium mole-fraction in the gas stream during the withdrawal phase

further away from the well. Hence, the fluid composition progressively approaches the initial fluid composition in the formation. Increased dispersivity strengthens the mixing, characterized by lower concentrations in the beginning and higher ones later in comparison to lower dispersivities. However, the dispersivity of $a_L = 100\,\text{m}$ is similar to the base case, while a significant difference can be observed for the high dispersivity case. The short-term increase in helium fraction in the early withdrawal time is remarkable, caused by the higher helium concentration in the first week of injection. However, this effect is only visible for low dispersivities as the more substantial mixing smooths the concentrations.

The mixing strength caused by mechanical dispersion is mainly influenced by the dispersivity and the flow velocity. Figure 4.22 depicts the magnitude of the gas dispersion coefficient ($D_{\text{disp}} = a \cdot u$) versus distance from the well (radially averaged) during injection and production. Generally, it is logical that the flow velocity far away from the well reduces while the flow velocities increase approaching the well. However, the flow velocity seems surprisingly low directly at the well, although it should be at the maximum at this specific point. This artifact emerges from the diverging flow at the well node. In this node, the flow occurs radially so that the magnitude theoretically is zero. Due to geometrical and petrophysical differences in the actual domain, the gas flow dominates in one direction, yielding a velocity magnitude larger than unity. Consequently, in the current implementation, this mixing is not determined correctly and could be adjusted by correcting the flow velocity with an additional contribution or increasing the dispersivity to promote mixing

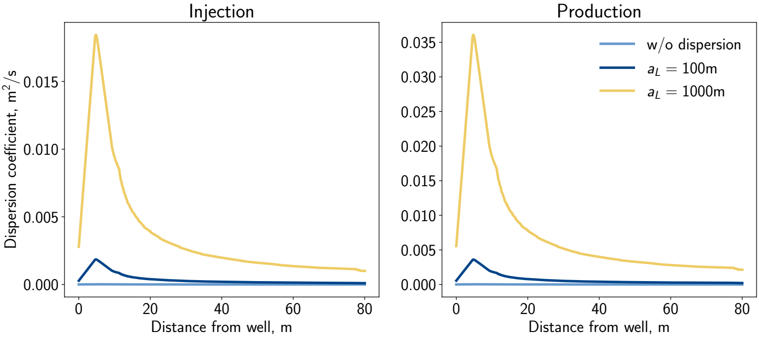

Figure 4.22: Dispersion coefficients versus distance from well during the injection and production phase

in the neighboring cells. Figure 4.22 also indicates the differences between typical values of molecular diffusion ($\approx 1 \cdot 10^{-7}$ m^2/s) and the dispersion coefficients with a magnitude of $\approx 1 \cdot 10^5$ higher, concluding that the gas mixing is dominated by mechanical dispersion near the well.

The varying strength of mixing with the initial gas also impacts hydrogen recovery. Figure 4.23 depicts the cumulative produced to injected hydrogen ratio, which can be considered recovery. Hence, recoveries of unity would imply that the injected hydrogen is entirely recovered, while lower values indicate partial reproduction. In this study, a relatively high hydrogen recovery with

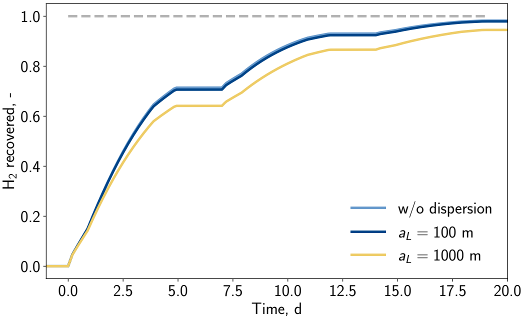

Figure 4.23: Ratio of hydrogen recovered (injected/produced) during the withdrawal phase

Table 4.3: Overview of hydrogen distributed in the system after the first field test phase

Case & Unit	Without disp.		$a_L = 100$		$a_L = 1000$	
	Sm^3	%	Sm^3	%	Sm^3	%
Produced H_2	7661.69	98.23	7637.16	97.91	7371.94	94.51
Stored H_2	138.31	1.77	162.16	2.09	428.06	5.49
Injected H_2	7800.00	100.00	7800.00	100.00	7800.00	100.00

more than 90 % is observed resulting from a higher cumulative production than injection volume ($Q_{\mathrm{inj}} = 156\,000\,\mathrm{Sm}^3$ and $Q_{\mathrm{prod}} = 468\,000\,\mathrm{Sm}^3$). Nevertheless, the impact of the gas mixing can also be observed in the recovery, where hydrogen recovery decreases with a larger mixing affinity. Table 4.3 gives an overview of the stored and produced hydrogen amounts at the end of the first phase. Once more, the negative impact of gas mixing on the hydrogen recovery becomes visible. While neglecting the process of mechanical dispersion, only approximately 1.72 % of the injected hydrogen remains in the reservoir. Cases including mechanical dispersion achieve up to 5.46 %. However, this mixing should not be considered as a permanent loss of hydrogen; moreover, with overall increasing hydrogen content in the storage, the effect of gas mixing decreases. Consequently, it can be expected that the gas-gas mixing with the initial gas is remarkable, particularly in the beginning, but will become less important with increasing storage cycles.

4.3. Conclusions and outlook

- The existing transport model in DuMu$^{\mathrm{x}}$ was successfully extended by mechanical dispersion for the multiphase n-component transport process to model the gas-gas mixing expected during UHS. Due to the required determination, this implementation was only achieved for the CVFE discretization scheme.

- Focusing on the CVFE method, a workflow for developing appropriate simulation grids based on actual geological models has been established. The workflow requires the geological horizons, and petrophysical properties can be transferred. The resulting grid comes as a .gmsh file, which can be imported into DuMu$^{\mathrm{x}}$ using the UGGrid manager. Additionally, the commonly applied Peaceman well model to determine the bottom-hole pressure was developed for the CVFE method in analogy to existing models for Voronoi grids. The subsequent implementation in DuMu$^\text{x}$ showed congruent results during the direct comparison between the cell-centered FV and CVFE methods.

- The developed workflow was used to investigate a UHS field test. The simulations show that the injected hydrogen mixes with the initial gas. The base case, where the process of mechanical dispersion is neglected, showed that after the withdrawal (three times the injected volume) 1.72 % of the injected hydrogen remained in the storage formation. As expected, the mixing is promoted with higher dispersivities and reduces the hydrogen recovery. For a dispersivity of 1000 m, only 94.54 % of the hydrogen was recovered in this study.
- Weaknesses of the implementation were observed for the flow velocities directly at the well, where the flow directions balance due to the radial flow. Consequently, an extension involving the high velocities at the well node is recommended.
- After the end of the first production phase of the field test, the simulated and observed hydrogen concentrations should be compared to investigate the effect of gas-gas mixing during UHS more accurately. The actual dispersivity can be estimated in a matching procedure based on the observed fluid concentrations in the withdrawal stream. If the field test implies biochemical reactions, the existing implementation can be used to reproduce the potential hydrogen loss.

Chapter 5

Coupling of microbial growth to the salt component for modeling of Underground Bio Methanation

While microbial reactions are generally unfavorable during UHS, Underground Bio Methanation aims to selectively utilize methanogenic microorganisms that consume carbon dioxide and hydrogen and produce methane and water. Consequently, the concept combines storage with a conversion process. It offers advantages such as existing infrastructures for natural gas and increased storage capacities due to better compressibilities and energy densities when compared to hydrogen [110]. However, the methanation process leads to reduced efficiency within a range of 49 % to 79 % [149] due to additional reactions.

The microbial activity of methanogenic archaea is considered one of the crucial factors for an Underground Bio Methanation Reactor (UMR), alongside good UGS properties. As described in Chapter 2.1.2, microbial growth is impacted by various factors, such as pH value, temperature, and salinity. This means that only a specific part of the storage formations can be used for this application since some do not have the optimal environmental conditions, and the microbial metabolism may be significantly or entirely inhibited. For instance, high salinities (>150 g/l) pose a challenge for UMR. However, an injection of freshwater could be suitable for initiating microbial activity by locally reducing salinity and creating a reactor volume. Furthermore, the water produced by metabolism could continuously increase the reactor volume over the years, increasing its throughput. Molecular diffusion of the salt component opposes this positive process, leading to increased salt concentration in the reactor due to the concentration difference. In this chapter, the behavior of this stimulation method and its efficiency through numerical simulations are studied. In the first step, the microbial growth was coupled to the salt component, followed by simulation runs, including a sensitivity analysis on a semi-artificial model.

The present simulations were part of the research project UMAS [101], funded by the German Federal Ministry of Economics and Technology. Excerpts from this research were published during the EAGE GET Conference 2022 [69].

5.1. Extension of microbial growth in dependency of the salinity

To model the impact of a freshwater injection initiating the process of UMR, the previously used simulation model of bio-reactive transport (see Section 3.1) was extended by the salt component on what the microbial growth depends on. This impact can be modeled differently: 1) Considering the inhibition within the Monod term [111] or 2) impacting the maximal growth rate. The latter showed better results in mimicking the behavior described in the literature for methanogenic microorganisms, as growth can be completely inhibited at high salt concentrations. Including the salt-dependent maximum growth, the double Monod model results as follows:

$$\psi^{\text{growth}}\left(c_w^{\text{salt}}\right) = \psi_{\text{max}}^{\text{growth}}\left(c_w^{\text{salt}}\right)\left(\frac{c_w^{\text{H}_2}}{\alpha_{\text{H}_2} + c_w^{\text{H}_2}}\right)\left(\frac{c_w^{\text{CO}_2}}{\alpha_{\text{CO}_2} + c_w^{\text{CO}_2}}\right) \tag{5.1}$$

where ψ^{growth} is the growth rate in 1/s, $\psi_{\text{max}}^{\text{growth}}$ is the maximal growth rate in 1/s, and c_w^{salt} is the mole fraction of salt in the liquid phase.

The characteristic growth parameters depend strongly on the species and can vary significantly. Due to simplicity and insufficient data, sodium chloride was assumed to be the sole salt component during the simulation and, therefore, represents the salinity parameter. In the present study, the halotolerant species "Methanocalculus halotolerans" was selected, and the growth rate as a function of salt was incorporated into the model based on the initial description [106]. Figure 5.1 depicts the corresponding data points. The highest maximum growth rate can be observed at salt concentrations of 50 g/l, while the growth is completely inhibited at concentrations above 140 g/l. To obtain a continuous characterization, these data points were matched by a best-fit of polynomial (second degree) and afterwards implemented into the source code of the simulator.

$$\psi_{\text{max}}^{\text{growth}}\left(c_w^{\text{NaCl}}\right) = -1.178 \cdot 10^{-2}\left(c_w^{\text{NaCl}}\right)^2 + 2.949 \cdot 10^{-4}\left(c_w^{\text{NaCl}}\right) + 1.204 \cdot 10^{-5} \tag{5.2}$$

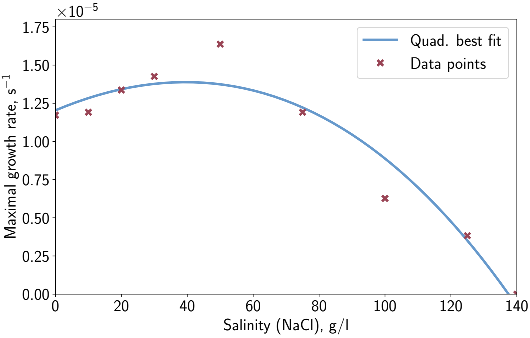

Figure 5.1: Maximum growth rate of "Methanocalculus halotolerans" in dependency of sodium chloride concentration according to Ollivier et al. [106]

To prevent a negative rate (e.g., at a salt concentration above 140 g/l), the following case distinction was defined:

$$\psi_{\max}^{\text{growth}} = \begin{cases} \psi & \text{if } \psi > 0 \\ 0 & \text{if } \psi \leq 0 \end{cases} \tag{5.3}$$

Overall, the best-fitted function posses the highest maximum growth rate at a salt concentration of 40 g/l ($\psi_{\max}^{\text{growth}} = 1.388 \cdot 10^{-5}/\text{s}$), from where it drops with increasing and decreasing salt content. Further parameters were taken from the literature and recent project results. The yield was calculated to achieve conversion rates from experimental results determining the hydrogen consumption. In batch experiments, conversion rates of $7.92\,\text{mol}/(\text{d} \cdot \text{Sm}^3)$ were observed [101]. This rate is expected at the highest growth found within the exponential phase where the substrate is present to its full extent. Assuming a constant salt concentration, the growth term can be reduced to the maximum growth:

$$\psi^{\text{growth}} = \psi_{\max}^{\text{growth}} \cdot \underbrace{\left(\frac{c_w^{H_2}}{\alpha_1 + c_w^{H_2}}\right)}_{=1} \underbrace{\left(\frac{c_w^{CO_2}}{\alpha_2 + c_w^{CO_2}}\right)}_{=1} = \psi_{\max}^{\text{growth}} \tag{5.4}$$

For the corresponding batch experiments, the porosity equals unity and the assumption that sufficient space for growth is available ($S_w \rightarrow 1$). So, the yield can be estimated by the following formulation:

$$Y = \gamma_\kappa \cdot \frac{\psi_{\max}^{\text{growth}}}{q^\kappa} \cdot n^{\max} \tag{5.5}$$

where γ_κ corresponds to the stoichiometric factor, q^κ is the conversion rate ($7.92\,\text{mol}/(\text{d} \cdot \text{Sm}^3)$), $n^{\max}$ is the maximum microbial density in $1/\text{m}^3$. The maximum microbial density depends on the equilibrium point between growth and decay (cf. Eq. 3.41). The input parameters, including their origin and the resulting yield, are listed in Table 5.1.

Table 5.1: Microbial growth parameters

Parameter	Symbol	Value	Unit	Reference
H_2-half velocity constant	α_{H_2}	$3.6 \cdot 10^{-7}$	-	[138]
CO_2-half velocity constant	α_{CO_2}	$1.98 \cdot 10^{-6}$	-	[138]
Initial number of microbes	n^*	$3 \cdot 10^8$	$1/\text{m}^3$	[101]
Decay factor	ψ^{decay}	0.1	1/d	[138]
Yield factor[1]	Y	$5.2 \cdot 10^8$	1/mol	[101]

5.2. Definition of simulation scenarios and sensitivity study

A simulation study was defined to assess the potential of a freshwater injection to stimulate microbial processes. Particular focus was placed on the sensitivities of microbial activity and injected water volume. In this study, the operation of the UMR was done along a single well configuration. For this investigation, a rotation-symmetric simulation grid consisting of conforming rectangular elements with the size of 2.5 m x 1 m and a dimension of 400 m x 20 m was used. The petrophysical properties were orientated on an actual storage formation. The spatial domain, including the well placement and perforated section, is depicted in Figure 5.2. The porosity was defined as 20 % and the permeability was defined in horizontal and vertical directions ($k_\text{h} = 100\,\text{mD}$ and $k_\text{v} = 1\,\text{mD}$) with a homogeneous distribution. As the discretization scheme, the CVFE method was used.

The initialization of the model was based on hydrostatic equilibrium with an initial reservoir pressure of 86 bar in the upper grid cells. In the beginning, the gas saturation was 50 %, which corresponds to the connate water saturation. The initial fluid is composed of H_2O, CH_4 and NaCl (290 g/l). Besides the extension of the simulation model by the salt component, an additional methane component (CH_4^{Bio}) was incorporated into the fluid system to track the recent biogenic gas.

In general, all boundaries except for the well were defined as a no-flow Neumann boundary, mimicking a closed system. The operation of the UMR was restricted by an upper and lower operation pressure. Typically, the upper pressure is limited by the cap rock's capillary threshold pressure and the formation's fracture pressure. In the present study, the upper-pressure limit of 100 bar should never be exceeded to maintain the integrity of the system. To ensure that these values are never surpassed, the injection and withdrawal were set to pressure-controlled. Additionally, the operation sequence covers injection, production, and idle times. Shut-in periods have the intention of improving the conversion process by giving the microorganisms time to consume the present substrates. In the beginning, the freshwater injection was

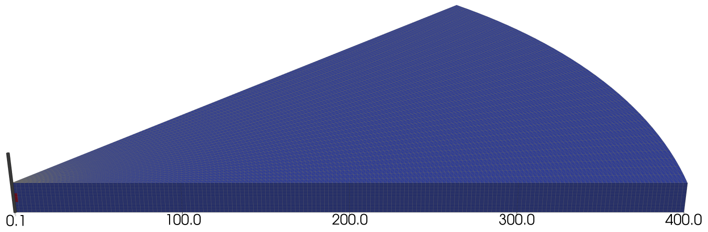

(A) Extruded part of the rotation-symmetric domain

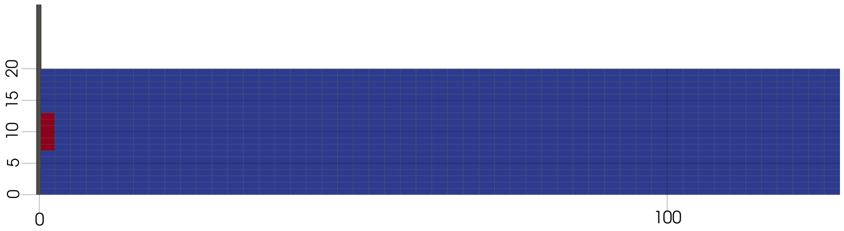

(B) Spatial discretization and operation well (🟥 perforated grid cells)

Figure 5.2: Overview of the rotation symmetric grid

performed to reduce the salinity locally. The duration is six months, followed by the regular storage cycles. One storage cycle is composed of five months of injection, two months idle, and five months of production. While the injection pressure was defined as 98 bar, the bottom-hole pressure during production was set to 93 bar. The injection gas contains 76% H_2, 19% CO_2, 2.5% CH_4 and 2.5% H_2O. The source/sink from the well was realized as a Neumann boundary condition, which is incorporated as follows:

- Pressure-controlled injection:

$$q^{\kappa}_{\text{inj}} = \int_{A^{\Gamma_N}} c^{\kappa}_{\text{inj}} \left(\frac{k_{rw}}{\mu_w} K_x \varrho_w \left(p_w - p_{\text{inj}}\right) + \frac{k_{rg}}{\mu_g} K_x \varrho_g \left(p_g - p_{\text{inj}}\right) \right) \mathrm{d}A \tag{5.6}$$

- Pressure-controlled production:

$$q^{\kappa}_{\text{prod}} = \int_{A^{\Gamma_N}} c^{\kappa}_{w} \frac{k_{rw}}{\mu_w} K_x \varrho_w \left(p_w - p_{\text{prod}}\right) + c^{\kappa}_{g} \frac{k_{rg}}{\mu_g} K_x \varrho_g \left(p_g - p_{\text{prod}}\right) \mathrm{d}A \tag{5.7}$$

where q^{κ} is the operation rate of component κ in mol/s, A^{Γ_N} is the well connection area (Neumann boundary) in m^3, c_{inj} is the injection concentration, ϱ is the molar phase density in $\mathrm{mol/m}^3$, and $p_{\text{inj/prod}}$ is the operation pressure (BHP) in Pa.

To identify the sensitivity of the volume of freshwater and the microbial activity on the conversion rate, four cases were defined (see Figure 5.3). In the present study, the amount of injected freshwater was controlled by the injection pressure within the first six months, with respect to not exceeding the fracture pressure in the near wellbore region. Generally, the injected water volume increases with higher injection pressures, leading to a higher reactive region. Furthermore, two microbial activity strengths were assessed due to its high uncertainty level. The higher activity was determined based on laboratory experiments, which should represent ideal growth conditions, while the lower activity was defined as ten times weaker than the measured one ($Y_{\text{Case II}} = 10 \cdot Y_{\text{Case I, III, IV}}$).

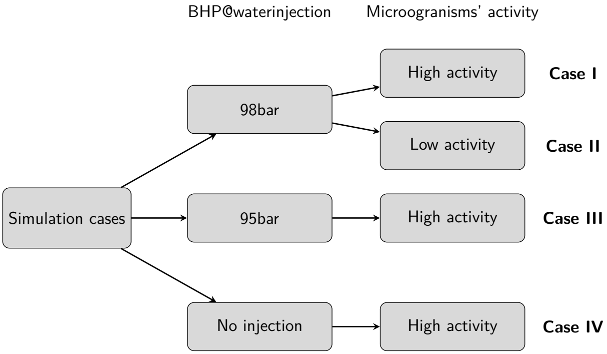

Figure 5.3: Definition of simulation cases with respect to the sensitivity of injected water volume and strength of microorganisms' activity

5.3. Results of sensitivity study

In total, four simulation cases varying in bottom-hole pressure during water injection and microbial activity were performed. In the following, the results of the simulations are presented and analyzed. Firstly, the freshwater injection period is investigated. Figure 5.4 presents the salt concentration after the freshwater injection period of six months.

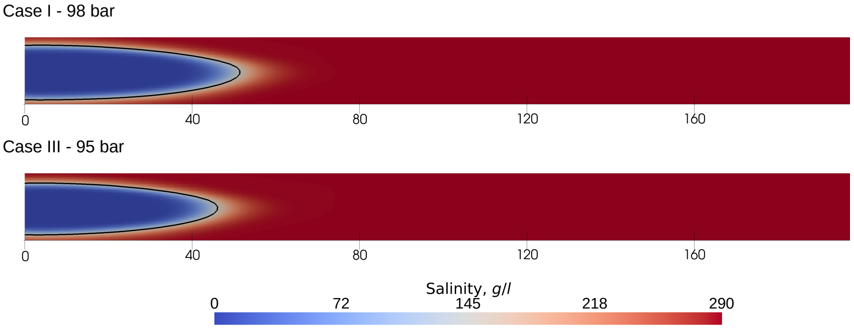

Figure 5.4: Salinity after the freshwater injection period of six months for both water injection pressures. The black contours represent an isoline at a salt concentration of $c_w^{NaCl} = 145\,g/l$.

It is evident that the injection of freshwater leads to a local decrease in salinity in the near-wellbore region. This low-saline region penetrates the formation approximately 50 m to 60 m and has a relatively sharp interface with the initial salt concentration. In general, the higher injection pressure leads to a larger affected region, which is expected due to varying injected water volumes. With an injection pressure of 95 bar (Case III) a volume of 16 500 Sm^3 is injected, while a 3 bar higher bottom-hole pressure (Cases I, II, and IV) increases the water volume by 33 % ($V_{\mathrm{inj}}^{\mathrm{w}} = 22\,000\,\mathrm{Sm}^3$). Remarkable is that the significant part of the formation remains at the initial salt concentration of 290 g/l.

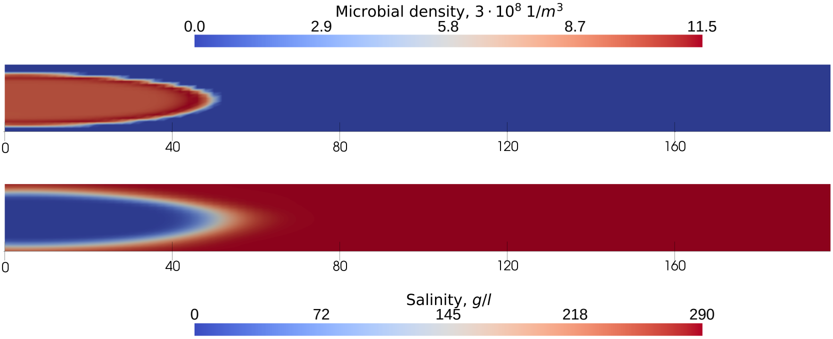

Figure 5.5: Spatial distribution of the microbes and its common trend with the salinity

In the next step, the impact of the salinity on microbial growth is evaluated. Figure 5.5 presents the salinity and the microbial density after the first gas injection cycle. It is visible that both parameters have the same spatial trend, which means that microbial activity is favored by the injection of freshwater. However, the most vital activity can be observed at the interface between the low-saline region and the initial reservoir brine. This can be explained by the salinity versus growth function (cf. Figure 5.1) where the maximum growth happens at a concentration of approximately 50 g/l. Consequently, the conversion rates are maximal at these salt concentrations, allowing a higher microbial density.

Regarding the average reservoir pressure (see Figure 5.6), different effects can be observed. As expected, a water injection leads to a pressure increase, while in the last case, with the absence of water injection, the pressure remains

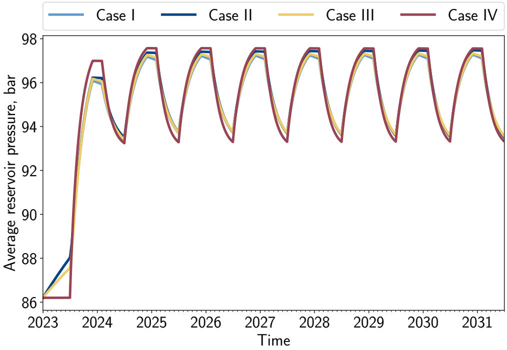

Figure 5.6: Average reservoir pressure versus time

constant at the beginning, which implies a stable initialization. Focusing on consecutive gas injections, a fast pressure increase is observed during the first injection cycle. For the last case with absent water injection, this increase behaves faster. Injecting more liquid components into the storage leads to decreased gas mobility, so the injection rate (pressure-controlled) decreases compared to the last case, also visible in Figure 5.7. Within one regular storage cycle, the pressure amplitude is approximately 4.5 bar, which almost represents the difference between production and injection pressures. A pressure drop, especially during idle times, is apparent with increasing microbial activity. This drop is caused by converting hydrogen and carbon dioxide to

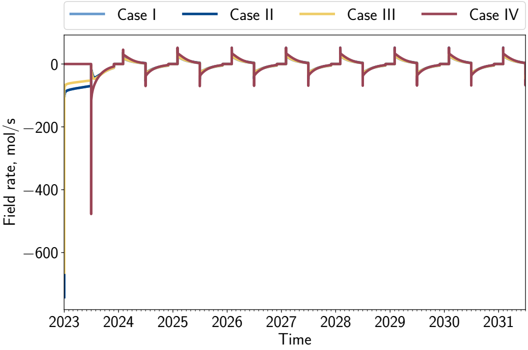

Figure 5.7: Field rate versus time

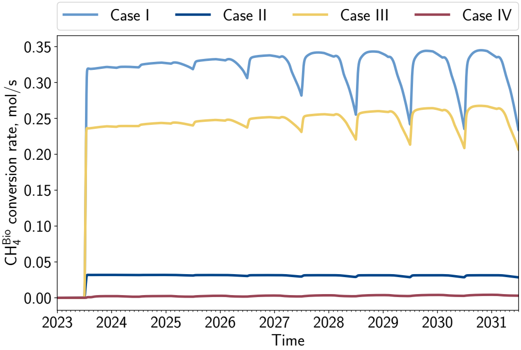

Figure 5.8: Conversion rate of CH_4^{Bio} versus time

methane and water. Regarding field rates, the trend corresponds to a pressure-controlled operation. Each injection/withdrawal episode begins with a high rate, which is reduced drastically until it achieves a constant value. Because all boundaries - except for the well - are defined as no-flow-Neumann boundaries, the rate tends to zero at the end of a cycle.

Regarding the UMR, maximizing the conversion from hydrogen and carbon dioxide into methane is favorable, meaning, ideally, that the injected fluid is entirely converted. The overall conversion rate becomes essential and is depicted in Figure 5.8 for the performed simulations. It is visible that in the best case, temporary up to 0.33 mol/s of methane are produced by the microorganisms. As aligned with previous observations, the conversion rate increases with higher microbial activity and larger freshwater volumes. Nevertheless, it is also evident that this conversion rate is influenced by the storage operation. In times of injection, the substrate supply is sufficient to maintain a higher rate. For the production, gas mixed with the initial gas flows progressively to the well, decreasing the overall reaction rate. For the simulation case with lower microbial activity, this phenomenon seems weaker as less hydrogen is consumed, leading to almost no limitation of substrate supply. A minor conversion can be observed for the last case (Case IV), where no freshwater injection occurred. This is caused by injecting a wet gas containing minor fractions of H_2O, reducing the salinity locally.

The production rate of CH_4^{Bio} and especially its development over time are a key of interest from an economic point of view. High methane, low hydrogen,

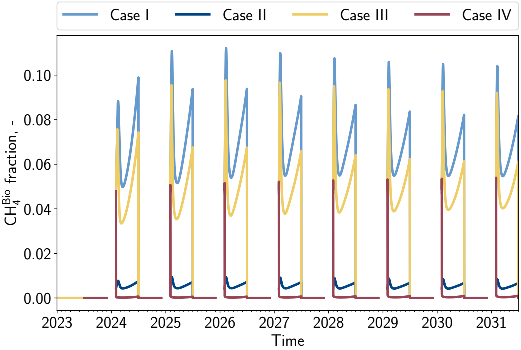

Figure 5.9: Molar fraction of CH_4^{Bio} in the production stream versus time

and low carbon dioxide concentrations indicate an effective reactor. In terms of CH_4^{Bio}-production (cf. Figure 5.9), a contrary behavior to the conversion rates can be observed. Except for the first cycle, the highest production concentrations are achieved at the beginning of the production period. During this time, the methane that was converted in the reactor during the idle phase is produced. However, due to the high pressure-controlled production rates, more hydrogen is increasingly produced. As the difference between bottom-hole and storage pressure decreases, the production rate decreases and at the same time, more substrates can again be converted on the flow pathway to the well. This leads to a higher methane concentration in the production stream where the fraction fluctuates between 5 % to 10 %. With increasing storage cycles, the proportion of recent methane decreases, which can be explained by an increasing proportion of cushion gas inflow into the reactor.

To assess the overall reactivity of the UMR and its behavior over time, the parameter of reactive volume is introduced:

$$V_{\text{reactive}} = \int_V S_w \phi \frac{\psi_{\text{max}}^{\text{growth}} \left(c_w^{\text{NaCl}}\right)}{\hat{\psi}_{\text{max}}^{\text{growth}}} \mathrm{d}V \tag{5.8}$$

where V_{reactive} is the reactive volume in m^3, V is the volume of the domain in m^3, S_w is the water saturation, ϕ is the porosity, $\psi_{\text{max}}^{\text{growth}}\left(c_w^{\text{NaCl}}\right)$ is local maximum growth rate in dependency of the salinity 1/s, and $\hat{\psi}_{\text{max}}^{\text{growth}}$ is the local maximum of the growth rate function in 1/s.

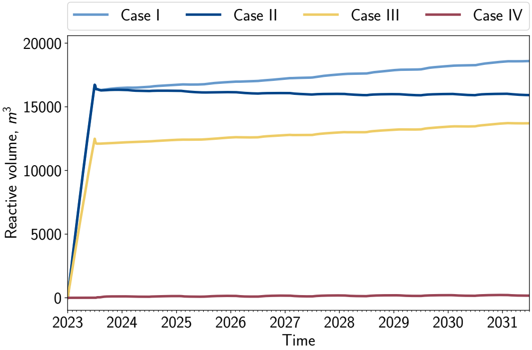

Figure 5.10: Reactive volume in dependency of time

Figure 5.10 represents the reactive volume during the water injection and the first eight consecutive storage cycles. In the beginning, no reactive volume can be observed due to the unfavorable conditions. The injection of freshwater leads to an increase in reactive volume, whereby the strength depends on the injected volume. Here, the highest and identical values are observed for Cases I and II, followed by Case III, which has medium levels. No significant reactive volume can be noted in the absence of freshwater injection. Because the microorganisms discharge molecular water during their metabolism, the reactive volume can be improved with stronger microbial growth and later storage cycles. Therefore, the reactive volume increases with good microbial activity, while the case with a high yield factor leads to decreased reactivity. This phenomenon is also visible in the trend of the simulation data. For Cases I and III, the additional water leads to better reactivity, while with a weak conversion rate, the effectiveness of the reactor decreases over time.

The microorganisms consume the injected hydrogen with time and thereby change the hydrogen content in the storage formation. Ideally, the hydrogen is converted entirely. Figure 5.11 represents the share of consumed hydrogen of the cumulative injected hydrogen. After eight storage cycles, the proportion of hydrogen consumed settles at around 35% in the best case. This result shows that the majority of the injected hydrogen is not converted as a result of the small reactor size, limited conversion rate, and the mixing with the cushion gas where no conversion can occur.

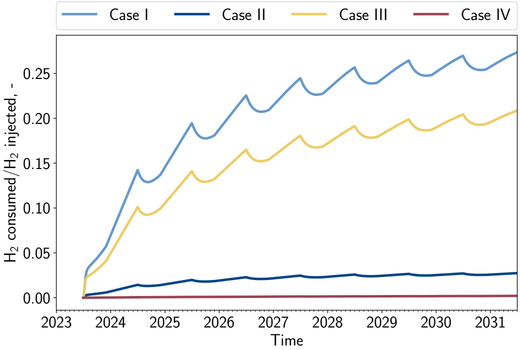

Figure 5.11: Share of consumed H_2 of the total injected H_2 in dependency of time

5.4. Conclusions and outlook

In conclusion, the simulations showed that, in principle, a significant part of hydrogen can be converted into methane. The freshwater injection initiated and stimulated microbial growth, establishing a reactor whose size is controlled by the volume of injected freshwater. Furthermore, only within this low-saline region the microorganisms' population grew, whereas the remaining part of the formation did not contribute - even with sufficient support of substrates - to the conversion process at all. The conversion rate was sensitively impacted by the microbial growth parameters (here: yield factor Y), where reactive volume increased in ideal cases due to the discharged molecular water. The progressive mixing with the initial cushion gas led to a temporary decrease in the production of recent methane. Although a remarkable fraction of the substrates has been consumed, this study did not observe a full conversion. Various methods can lead to an improved result where the UMR can achieve higher throughput:

- Instead of using a single well configuration for injection and production of the fluids, a combination of two wells [68] allows the continuous injection and production with the conversion along the flow path from one to the other well. In general, the system is less dynamic, leading to a more consistent production gas composition.

- To achieve a full conversion in a comparatively short period of time, reduction of the substrate concentrations and/or of overall rates can allow the reproduction of higher contents of converted methane, enabling a more stable withdrawal gas composition.
- Changes in the schedule regarding the pressure-controlled injection could also improve the single well configuration. Here, a step-wise increase/decrease within a period can maintain less dynamic rates, thereby improving conversion. If the conventional storage cycles (injection in summer and production in winter) are to be preserved, an extension of the idle phase is hard to incorporate.

The implementation of the bio-reactive transport process with dependency on the salt component in the open-source simulator shows good results where the expectations are fulfilled. The dependency of microbial growth mimics the observation in the literature. However, further investigations should be performed to cover this process more reliably. Here, the microbial growth parameters face the highest uncertainty, which have to be evaluated for every geological formation independently to obtain reliable input data. Further, the effects of the recently introduced gases, such as geochemical reactions and dissolution of minerals, may influence the process. The dissolution of evaporite minerals may increase the salinity over time due to its solubility in the aqueous phase and, consequently, harmfully impact the success of the potential UMR.

Chapter 6

Conclusions

The thesis is composed of three parts: The development, implementation, and calibration of the bio-geo-reactive transport model during UHS in porous media, the extension of the implementation for the modeling of mechanical dispersion to predict a field test operation, and the application of the developed model to assess the stimulation of a UMR by freshwater injection. An extensive conclusion can be found at the end of each chapter respectively. In the following, the main conclusions are summarized:

- The storage of hydrogen in the porous subsurface has some significant differences compared to the conventional storage of natural gas. Besides hydrodynamic phenomena such as viscous fingering and density override, the gas-gas mixing of injected and initial gas due to molecular diffusion and mechanical dispersion becomes crucial and significantly impacts the storage efficiency. Not only the well positions need to be selected more carefully, but the high injection rates lead to a strong mixing and temporarily reduce hydrogen recovery. Additionally, permanent hydrogen losses by bio- and geochemical reactions are expected. Hydrogenotrophic microorganisms potentially consume significant parts of the stored hydrogen and simultaneously lead to contamination of the stored gas. Similar outcomes can result from geochemical reactions producing harmful products like hydrogen sulfide. However, until today, only a few experiments have been conducted to investigate these reactions on a field scale, and the prediction of the processes was only covered partially by numerical simulations.

- Addressing these unique reactions, an existing mathematical model describing the bio-reactive transport process was extended by the potential geochemical reaction of pyrite-to-pyrrhotite reduction. The developed model was implemented in the open-source simulator DuMu^x and calibrated based on laboratory investigations. To improve the modeling of molecular diffusion, recent experiments for the binary system hydrogen-methane at typical gas storage conditions were used to build correlations in dependency of thermodynamic conditions and petrophysical properties. Subsequently, the developed correlations were implemented in DuMu$^{\text{x}}$ where the experimental observations could be reproduced. Focusing on the chemical reactions, the biochemical and geochemical reactions were calibrated based on reproducing reactor experiments. The microbial growth parameters in DuMu$^{\text{x}}$ were calibrated by matching results of a batch reactor experiment with methanogenic archaea and were thereafter transferred for field-scale purposes. The geochemical modeling comprised the development of a kinetic reaction model in DuMu$^{\text{x}}$. It allows the reproduction of the hydrogen sulfide generation during the reactor experiments of Truche et al. [150], where pyrite was exposed to a hydrogen atmosphere at high temperatures and pressure. Likewise, after calibration, the model was employed on a recently developed UHS benchmark scenario to assess the impact on the operation and the hydrogen recovery. For this specific scenario, up to 10 % of the injected hydrogen was permanently lost due to reactions. Additionally, indicators for the presence of the different reactions could be identified in the concentration trends during withdrawal.

- To improve the understanding of gas-gas mixing by mechanical dispersion, the implementation in DuMu$^{\text{x}}$ was modified by enlarging this process upon the multiphase systems. This extension required the CVFE scheme, coming with the global velocity field, instead of the previously used cell-centered FV method. This modification led to the development of a workflow from typical geological models to a simulation mesh suitable for FE methods. Additionally, the development and implementation of a corresponding well model and an interface for importing and processing actual field data were realized in DuMu$^{\text{x}}$. The developed model was employed to predict an ongoing UHS field test. To model this field test, a cropped geological structure, only partially containing the gas cap of the target formation, was applied for the developed workflow, and the behavior of the pressure during the recent operation was successfully matched by modeling the appending gas cap in a history match. Regarding the field test, a sensitivity study on the dispersivity was performed where, with increasing value, the mixing became stronger, leading to a reduced hydrogen recovery at the end of the withdrawal phase.

- The bio-reactive transport model in DuMu$^{\text{x}}$ showed furthermore its potential for the modeling of the concept of UMR. The implementation of microbial growth was extended on the dependency of salt. The extended model was afterwards used to assess the potential of a freshwater injection to stimulate microbial growth by reducing the salinity locally to enable metabolism. A sensitivity study on the injected water volume and the strength of metabolisms was conducted on an artificial simulation domain to investigate the potential of such a process. Although a significant amount of hydrogen was converted (up to 27 %), the striven for complete conversion was not observed.

- In conclusion, the developed implementation in DuMu$^{\text{x}}$ provides an open-source tool for modeling UHS-specific scenarios, including chemical reactions (code is available as Gitlab [67] and persistent repository [65]). Moreover, the extension allows to predict the operation of UHS, and also laboratory investigations such as reactor experiments can be reproduced in DuMu$^{\text{x}}$. The model possesses improved predictability compared to previous implementations due to its more applicable fluid system and the calibration of hydrogen-specific processes by experimental observations. Nevertheless, the empirical data from the laboratory and its transfer to the field scale still need to be validated by matching field test data.

Bibliography

[1] I. Aavatsmark. Equivalent well-cell radius for hexagonal K-orthogonal grids in numerical reservoir simulation. *Applied Mathematics Letters*, 61:122–128, Nov. 2016. ISSN 08939659. doi:10.1016/j.aml.2016.05.013.

[2] A.-C. Ahn, A. Hidalgo-Ulloa, Y. Pereva, B. Lomans, and D. Z. Sousa. Review of the window of viability of the different microbial metabolisms relevant for subsurface H2 storage applications. H2020 HyUSPRe Project Report D3.1, Wageningen University & Research, Oct. 2023. URL https://www.hyuspre.eu/wp-content/uploads/2022/10/HyUSPRe_D3.1_Viability-of-microbial-metabolisms-relevant-for-UHS_2022.10.01.pdf.

[3] G. Alefeld and J. Völkl. *Hydrogen in Metals. 1: Basic Properties*. Number 28 in Topics in Applied Physics. Springer, Berlin Heidelberg, 1978. ISBN 978-3-540-08705-2 978-0-387-08705-4 978-3-662-30846-2.

[4] Arbeitsgemeinschaft Energiebilanzen e.V. Bruttostromerzeugung in Deutschland nach Energieträgern, Feb. 2023. URL https://ag-energiebilanzen.de/wp-content/uploads/2022/09/STRERZ22_Abgabe-12-2022_inkl-Rev-EE.pdf. (accessed 05.02.2023).

[5] O. H. Ardakani, A. Chappaz, H. Sanei, and B. Mayer. Effect of thermal maturity on remobilization of molybdenum in black shales. *Earth and Planetary Science Letters*, 449:311–320, Sept. 2016. ISSN 0012821X. doi:10.1016/j.epsl.2016.06.004.

[6] F. Bardelli, C. Mondelli, M. Didier, J. G. Vitillo, D. R. Cavicchia, J.-C. Robinet, L. Leone, and L. Charlet. Hydrogen uptake and diffusion in Callovo-Oxfordian clay rock for nuclear waste disposal technology. *Applied Geochemistry*, 49:168–177, Oct. 2014. ISSN 08832927. doi:10.1016/j.apgeochem.2014.06.019.

[7] P. Bastian, M. Blatt, A. Dedner, N.-A. Dreier, C. Engwer, R. Fritze, C. Gräser, C. Grüninger, D. Kempf, R. Klöfkorn, M. Ohlberger, and

O. Sander. The Dune framework: Basic concepts and recent developments. *Computers & Mathematics with Applications*, 81:75–112, Jan. 2021. ISSN 08981221. doi:10.1016/j.camwa.2020.06.007.

[8] L. Baumgartner, R. Reid, C. Dupraz, A. Decho, D. Buckley, J. Spear, K. Przekop, and P. Visscher. Sulfate reducing bacteria in microbial mats: Changing paradigms, new discoveries. *Sedimentary Geology*, 185(3-4):131–145, Mar. 2006. ISSN 00370738. doi:10.1016/j.sedgeo.2005.12.008.

[9] J. Bear. *Hydraulics of Groundwater*. McGraw-Hill Series in Water Resources and Environmental Engineering. McGraw-Hill International Book Co, London; New York, 1979. ISBN 978-0-07-004170-7.

[10] J. Bear. *Modeling Phenomena of Flow and Transport in Porous Media*, volume 31 of *Theory and Applications of Transport in Porous Media*. Springer International Publishing, Cham, 2018. ISBN 978-3-319-72825-4 978-3-319-72826-1. doi:10.1007/978-3-319-72826-1.

[11] J. Bear and Y. Bachmat. Generalized theory on hydrodynamic dispersion in porous media. *Int. Union Geod. Geophys. Publ.*, 72, Jan. 1967. URL https://www.osti.gov/biblio/6035908.

[12] C. Bethke. *Geochemical Reaction Modeling: Concepts and Applications*. Oxford University Press, New York, 1996. ISBN 978-0-19-509475-6.

[13] C. M. Bethke. *Geochemical and Biogeochemical Reaction Modeling*. Cambridge University Press, 3rd edition, Dec. 2021. ISBN 978-1-108-80700-5 978-1-108-79086-4. doi:10.1017/9781108807005.

[14] Z. Bo, L. Zeng, Y. Chen, and Q. Xie. Geochemical reactions-induced hydrogen loss during underground hydrogen storage in sandstone reservoirs. *International Journal of Hydrogen Energy*, 46, 2021. doi:10.1016/j.ijhydene.2021.03.116.

[15] Z. Bo, M. Boon, H. Hajibeygi, and S. Hurter. Impact of experimentally measured relative permeability hysteresis on reservoir-scale performance of underground hydrogen storage (UHS). *International Journal of Hydrogen Energy*, 48(36):13527–13542, Apr. 2023. ISSN 03603199. doi:10.1016/j.ijhydene.2022.12.270.

[16] I. C. Bourg, L. E. Beckingham, and D. J. DePaolo. The Nanoscale Basis of CO_2 Trapping for Geologic Storage. *Environmental Science & Technology*, 49(17):10265–10284, Sept. 2015. ISSN 0013-936X, 1520-5851. doi:10.1021/acs.est.5b03003.

[17] J. P. Bourgeois, N. Aupaix, R. Bloise, and J. L. Millet. Proposition d'explication de la formation d'hydrogène sulfuré dans les stockages souterrains de gaz naturel par réduction des sulfures minéraux de la roche magasin. *Revue de l'Institut Français du Pétrole*, 34(3):371–386, May 1979. ISSN 0020-2274. doi:10.2516/ogst:1979013.

[18] R. H. Brooks and A. T. Corey. Hydraulic Properties of Porous Media and Their Relation to Drainage Design. *Transactions of the ASAE*, 7 (1):0026–0028, 1964. ISSN 2151-0059. doi:10.13031/2013.40684.

[19] R. Brown. XXVII. A brief account of microscopical observations made in the months of June, July and August 1827, On the particles contained in the pollen of plants; and on the general existence of active molecules in organic and inorganic bodies. *The Philosophical Magazine*, 4(21):161–173, Sept. 1828. ISSN 1941-5850, 1941-5869. doi:10.1080/14786442808674769.

[20] S. Buckley and M. Leverett. Mechanism of Fluid Displacement in Sands. *Transactions of the AIME*, 146(01):107–116, Dec. 1942. ISSN 0081-1696. doi:10.2118/942107-G.

[21] J. C. Butcher. *Numerical Methods for Ordinary Differential Equations.* Wiley, New York and Weinheim, 2003. ISBN 978-0-471-96758-3.

[22] F. Buzek, V. Onderka, P. Vančura, and I. Wolf. Carbon Isotope Study of Methane Production in a Town Gas Storage Reservoir. *Fuel*, 73(5): 747–752, 1994. ISSN 0016-2361. doi:10.1016/0016-2361(94)90019-1.

[23] P. C. Carman. Permeability of saturated sands, soils and clays. *The Journal of Agricultural Science*, 29(2):262–273, Apr. 1939. ISSN 0021-8596, 1469-5146. doi:10.1017/S0021859600051789.

[24] A. Cavanagh, H. Yousefi, M. Wilkinson, and R. Groenenberg. Hydrogen storage potential of existing European gas storage sites in depleted gas fields and aquifer. H2020 HyUSPRe Project Report D1.3, University of Edinburgh, June 2022. URL https://www.hyuspre.eu/wp-content/upl

oads/2022/06/HyUSPRe_D1.3_Hydrogen-storage-potential-of-existing-European-gas-storage-sites_2022.06.29.pdf.

[25] M. Chai, Z. Chen, H. Nourozieh, and M. Yang. Numerical simulation of large-scale seasonal hydrogen storage in an anticline aquifer: A case study capturing hydrogen interactions and cushion gas injection. *Applied Energy*, 334:120655, Mar. 2023. ISSN 03062619. doi:10.1016/j.apenergy.2023.120655.

[26] S. R. Charlton and D. L. Parkhurst. Modules based on the geochemical model PHREEQC for use in scripting and programming languages. *Computers & Geosciences*, 37(10):1653–1663, Oct. 2011. ISSN 00983004. doi:10.1016/j.cageo.2011.02.005.

[27] L. L.-y. Chen, D. L. Katz, and M. R. Tek. Binary gas diffusion of methane-nitrogen through porous solids. *AIChE Journal*, 23(3):336–341, May 1977. ISSN 0001-1541, 1547-5905. doi:10.1002/aic.690230317.

[28] M. S. Costanza-Robinson and M. L. Brusseau. Gas phase advection and dispersion in unsaturated porous media. *Water Resources Research*, 38(4), Apr. 2002. ISSN 0043-1397, 1944-7973. doi:10.1029/2001WR000895.

[29] H. Cypionka. *Grundlagen der Mikrobiologie.* Springer-Lehrbuch. Springer, Berlin Heidelberg, 4th edition, 2010. ISBN 978-3-642-05095-4. doi:10.1007/978-3-642-05096-1.

[30] N. Dopffel, S. Jansen, and J. Gerritse. Microbial side effects of underground hydrogen storage – Knowledge gaps, risks and opportunities for successful implementation. *International Journal of Hydrogen Energy*, 46(12):8594–8606, 2021. doi:10.1016/j.ijhydene.2020.12.058.

[31] N. Eddaoui, M. Panfilov, L. Ganzer, and B. Hagemann. Impact of Pore Clogging by Bacteria on Underground Hydrogen Storage. *Transport in Porous Media*, 139(1):89–108, Aug. 2021. ISSN 0169-3913, 1573-1634. doi:10.1007/s11242-021-01647-6.

[32] A. Einstein. Über die von der molekularkinetischen Theorie der Wärme geforderte Bewegung von in ruhenden Flüssigkeiten suspendierten Teilchen. *Annalen der Physik*, 322(8):549–560, 1905. ISSN 00033804, 15213889. doi:10.1002/andp.19053220806.

[33] A. M. Elgendy, A. Pizzolato, M. Maniglio, C. Geloni, P. Panfili, and C. Topini. Reactive Transport Modelling of H2 Storage in Depleted Gas Fields: An Approach to Implement Biogeochemical Reactions in a Compositional Reservoir Simulator. In *Day 1 Mon, June 05, 2023*, Vienna, Austria, June 2023. SPE. doi:10.2118/214434-MS.

[34] D. Enning and J. Garrelfs. Corrosion of Iron by Sulfate-Reducing Bacteria: New Views of an Old Problem. *Applied and Environmental Microbiology*, 80(4):1226–1236, Feb. 2014. ISSN 0099-2240, 1098-5336. doi:10.1128/AEM.02848-13.

[35] European Space Agency. Technology Readiness Levels Handbook for Space Applications. Technical report, European Space Agency, 2008. URL https://artes.esa.int/sites/default/files/TRL_Handbook.pdf.

[36] F. Feldmann, B. Hagemann, L. Ganzer, and M. B. Panfilov. Numerical Simulation of Hydrodynamic and Gas Mixing Processes in Underground Hydrogen Storages. *Environmental Earth Sciences*, 75(16):103, 2016. ISSN 1866-6280. doi:10.1007/s12665-016-5948-z.

[37] A. Fick. Ueber Diffusion. *Annalen der Physik und Chemie*, 170(1): 59–86, 1855. ISSN 00033804, 15213889. doi:10.1002/andp.18551700105.

[38] B. Flemisch, M. Darcis, K. Erbertseder, B. Faigle, A. Lauser, K. Mosthaf, S. Müthing, P. Nuske, A. Tatomir, M. Wolff, and R. Helmig. DuMu^x: DUNE for Multi-(Phase, Component, Scale, Physics,. . .) Flow and Transport in Porous Media. *Advances in Water Resources*, 34(9): 1102–1112, 2011. ISSN 03091708. doi:10.1016/j.advwatres.2011.03.007.

[39] S. Foh, M. Novil, E. Rockar, and P. Randolph. Underground hydrogen storage - Final report. *Energy Storage and Conversion Division Department of Energy and Environment*, 1979. doi:10.2172/6536941.

[40] E. N. Fuller and J. C. Giddings. A Comparison of Methods for Predicting Gaseous Diffusion Coefficients. *Journal of Chromatographic Science*, 3(7):222–227, July 1965. ISSN 0021-9665, 1945-239X. doi:10.1093/chromsci/3.7.222.

[41] E. N. Fuller, P. D. Schettler, and J. Calvin. Giddings. New method for prediction of binary gas-phase diffusion coefficients. *Industrial & Engineering Chemistry*, 58(5):18–27, May 1966. ISSN 0019-7866, 1541-5724. doi:10.1021/ie50677a007.

[42] E. N. Fuller, K. Ensley, and J. C. Giddings. Diffusion of halogenated hydrocarbons in helium. The effect of structure on collision cross sections. *The Journal of Physical Chemistry*, 73(11):3679–3685, Nov. 1969. ISSN 0022-3654, 1541-5740. doi:10.1021/j100845a020.

[43] L. Ganzer, V. Reitenbach, D. Albrecht, and B. Hagemann. TP1: Gekoppelte geohydraulische und mineralogisch-geochemische Prozesse in Reservoir- und Deckgesteinsformationen: TP2: Numerische Simulation von Gasvermischungsprozessen während der Wasserstoffspeicherung: Endbericht zum F&E Verbundvorhaben H2STORE: Berichtszeitraum: 01.08.2012 bis 31.12.2015. *TP1: Gekoppelte geohydraulische und mineralogisch-geochemische Prozesse in Reservoir- und Deckgesteinsformationen*, 2016. doi:10.2314/GBV:871964139.

[44] L. Ganzer, V. Reitenbach, B. Hagemann, G. Strobel, R. Peitz, C. Boersheim, and J. Oppelt. Verbundvorhaben HyINTEGER: Untersuchungen zur Integrität von Bohrungen und technischen Materialien in geologischen H2-Untergrundreservoiren; Teilprojekt: Experimentelle und numerische Untersuchungen der technischen Integrität von UGS-Bohrungen (TP2, TP4, TP6): Abschlussbericht HyINTEGER : Berichtszeitraum: 01.01.2016-30.09.2019. *Verbundvorhaben HyINTEGER: Untersuchungen zur Integrität von Bohrungen und technischen Materialien in geologischen H2-Untergrundreservoiren; Teilprojekt: Experimentelle und numerische Untersuchungen der technischen Integrität von UGS-Bohrungen (TP2, TP4, TP6)*, 2019. doi:10.2314/KXP:1736133926.

[45] Gas Infrastructure Europe. Aggregated Gas Storage Inventory, 2023. URL https://agsi.gie.eu/. (accessed 05.09.2023).

[46] E. Gaucher, C. Tournassat, F. Pearson, P. Blanc, C. Crouzet, C. Lerouge, and S. Altmann. A robust model for pore-water chemistry of clayrock. *Geochimica et Cosmochimica Acta*, 73(21):6470–6487, Nov. 2009. ISSN 00167037. doi:10.1016/j.gca.2009.07.021.

[47] Gecko Instruments GmbH. Die Erdgaszusammensetzungen in Deutschland, 2023. URL https://www.gecko-instruments.de/pages/produkte/precisive/erdgas-zusammensetzung.php. (accessed 26.04.2023).

[48] Geostock SAS, Ludwig-Boelko-Systemtechnik GmbH, Montanuniversität Leoben, CO2GEONET, MicroPro GmbH, Fundacion para el Desarrollo de las Nuevas Technologias del Hidrogeno en Aragon, and

Instytut Gospodarki Surowcami Mineralnymi i Energia Pan. Hydrogen Storage In European Subsurface - HyStorIES, 2023. URL https://doi.org/10.3030/101007176. (accessed 18.12.2023).

[49] C. Geuzaine and J.-F. Remacle. Gmsh: A three-dimensional finite element mesh generator with built-in pre- and post-processing facilities. *International Journal for Numerical Methods in Engineering*, 79(11): 1309–1331, Sept. 2009. ISSN 00295981. doi:10.1002/nme.2579.

[50] W. C. Ghiorse and J. T. Wilson. Microbial Ecology of the Terrestrial Subsurface. In *Advances in Applied Microbiology*, volume 33, pages 107–172. Elsevier, 1988. ISBN 978-0-12-002633-3. doi:10.1016/S0065-2164(08)70206-5.

[51] T. Groß, P. Dunkel, D. Franzmann, H. Heinrichs, J. Linßen, and D. Stolten. H2 supply from Renewable Energy Sources, H2 demand centers and H2 transport infrastructure. H2020 HyUSPRe Project Report D1.2, Forschungszentrum Jülich, July 2022. URL https://www.hyuspre.eu/wp-content/uploads/2022/04/HyUSPRe_D1.2_H2-supply-from-Renewable-Energy-Sources_2022.03.30.pdf.

[52] T. Groß, P. Dunkel, J. Linßen, and D. Stolten. Report on the EU-scale hydrogen system scenarios. H2020 HyUSPRe Project Report D7.2, Forschungszentrum Jülich, Dec. 2023.

[53] G. Guevara-Carrion, S. Ancherbak, A. Mialdun, J. Vrabec, and V. Shevtsova. Diffusion of methane in supercritical carbon dioxide across the Widom line. *Scientific Reports*, 9(1):8466, June 2019. ISSN 2045-2322. doi:10.1038/s41598-019-44687-1.

[54] B. Hagemann. *Numerical and Analytical Modeling of Gas Mixing and Bio-Reactive Transport During Underground Hydrogen Storage*, volume Band 50 of *Schriftenreihe Des Energie-Forschungszentrums Niedersachsen*. Cuvillier Verlag, Göttingen, 1st edition, 2018. ISBN 978-3-7369-9714-1. URL https://dokumente.ub.tu-clausthal.de/receive/clausthal_mods_00000546.

[55] B. Hagemann, L. Ganzer, and M. Panfilov. Field Scale Modeling Of Bio-Reactions During Underground Hydrogen Storage. In *ECMOR XVI - 16th European Conference on the Mathematics of Oil Recovery*, Proceedings, Barcelona, Spain, 2018. EAGE Publications BVNetherlands. doi:10.3997/2214-4609.201802116.

[56] A. J. Hall. Pyrite-pyrrhotine redox reactions in nature. *Mineralogical Magazine*, 50(356):223–229, June 1986. ISSN 0026-461X, 1471-8022. doi:10.1180/minmag.1986.050.356.05.

[57] S. Harati, S. Rezaei Gomari, F. Gasanzade, S. Bauer, T. Pak, and C. Orr. Underground hydrogen storage to balance seasonal variations in energy demand: Impact of well configuration on storage performance in deep saline aquifers. *International Journal of Hydrogen Energy*, 48(69):26894–26910, Aug. 2023. ISSN 03603199. doi:10.1016/j.ijhydene.2023.03.363.

[58] A. Hassanpouryouzband, K. Adie, T. Cowen, E. M. Thaysen, N. Heinemann, I. B. Butler, M. Wilkinson, and K. Edlmann. Geological Hydrogen Storage: Geochemical Reactivity of Hydrogen with Sandstone Reservoirs. *ACS Energy Letters*, 7(7):2203–2210, 2022. doi:10.1021/acsenergylett.2c01024.

[59] C. Hebling, M. Ragwitz, T. Fleiter, U. Groos, D. Härle, A. Held, M. Jahn, N. Müller, T. Pfeifer, P. Plötz, O. Ranzmeyer, A. Schaadt, F. Sensfuß, T. Smolinka, and M. Wietschel. Eine Wasserstoff-Roadmap für Deutschland. Position paper, Fraunhofer-Institut für System- und Innovationsforschung ISI, Karlsruhe Fraunhofer-Institut für Solare Energiesysteme ISE, Freiburg, Karlsruhe & Freiburg, Oct. 2019.

[60] N. Heinemann, J. Alcalde, J. M. Miocic, S. J. T. Hangx, J. Kallmeyer, C. Ostertag-Henning, A. Hassanpouryouzband, E. M. Thaysen, G. J. Strobel, C. Schmidt-Hattenberger, K. Edlmann, M. Wilkinson, M. Bentham, R. Stuart Haszeldine, R. Carbonell, and A. Rudloff. Enabling large-scale hydrogen storage in porous media – the scientific challenges. *Energy & Environmental Science*, 14(2):853–864, 2021. ISSN 1754-5692. doi:10.1039/D0EE03536J.

[61] R. Helmig. *Multiphase Flow and Transport Processes in the Subsurface.* Environmental Engineering. Springer, Berlin; New York, 1997. ISBN 978-3-642-64545-7.

[62] C. Hemme and W. van Berk. Hydrogeochemical Modeling to Identify Potential Risks of Underground Hydrogen Storage in Depleted Gas Fields. *Applied Sciences*, 8(11), 2018. ISSN 2076-3417. doi:10.3390/app8112282.

[63] W. Henry. III. Experiments on the quantity of gases absorbed by water, at different temperatures, and under different pressures. *Philosophical Transactions of the Royal Society of London*, 93:29–274, Dec. 1803. ISSN 0261-0523, 2053-9223. doi:10.1098/rstl.1803.0004.

[64] C. K. Ho and S. W. Webb. *Gas Transport in Porous Media*, volume 20. Springer Netherlands, 2006. ISBN 978-1-4020-3961-4. doi:10.1007/1-4020-3962-X.

[65] S. Hogeweg. Replication Data for: Numerical Investigations of Reactive Transport Processes during the Storage of Hydrogen in the Porous Subsurface, 2024. URL https://doi.org/10.25625/2D2WFO.

[66] S. Hogeweg and B. Hagemann. Integrated modeling approach for the overall performance, integrity, and durability assessment of hydrogen storage at the reservoir and near-wellbore scale. H2020 HyUSPRe Project Report D6.1, Clausthal University of Technology, Mar. 2022. URL https://www.hyuspre.eu/wp-content/uploads/2022/11/HyUSPRe_D6.1_Integrated-modelling-approach-for-the-performance-of-H2-storage_2022.11.03.pdf.

[67] S. Hogeweg and B. Hagemann. GitLab Repository - dumux-hyuspre, May 2024. URL https://gitlab.tu-clausthal.de/energy-storage-group/hyuspre/dumux-hyuspre. (accessed 25.05.2024).

[68] S. Hogeweg, G. Strobel, and B. Hagemann. Simulation of Underground Microbiological Methanation in a Conceptional Well Doublet System. In *DGMK/ÖGEW-Frühjahrstagung 2019*, Celle, 2019. ISBN 978-3-941721-96-8.

[69] S. Hogeweg, B. Hagemann, and L. Ganzer. Simulation of Freshwater Injection to Enable Underground Bio-Methanation in High-Saline Gas Storage Formations. In *EAGE GET 2022*, volume 2022, pages 1–5, Den Hague, 2022. European Association of Geoscientists & Engineers. doi:10.3997/2214-4609.202221055.

[70] S. Hogeweg, G. Strobel, and B. Hagemann. Benchmark study for the simulation of Underground Hydrogen Storage operations. *Computational Geosciences*, 26(6):1367–1378, Aug. 2022. ISSN 1420-0597, 1573-1499. doi:10.1007/s10596-022-10163-5.

[71] S. Hogeweg, B. Hagemann, and L. Ganzer. Validated open-source reservoir modeling software that can simulate coupled flow, geochemical and microbiological processes in a porous reservoir under operational hydrogen storage conditions. H2020 HyUSPRe Project Report D6.2, Clausthal University of Technology, June 2023. URL https://www.hyuspre.eu/wp-content/uploads/2023/09/HyUSPRe_D6.2_Extension-of-open-source-simulator-Dumux_v2023.06.30.pdf.

[72] S. Hogeweg, J. Michelsen, B. Hagemann, and L. Ganzer. Empirical and Numerical Modelling of Gas–Gas Diffusion for Binary Hydrogen–Methane Systems at Underground Gas Storage Conditions. *Transport in Porous Media*, Dec. 2023. ISSN 0169-3913, 1573-1634. doi:10.1007/s11242-023-02039-8.

[73] S. Hogeweg, J. Michelsen, B. Hagemann, and L. Ganzer. Replication Data for: Empirical and numerical modelling of gas-gas diffusion for binary hydrogen-methane systems at underground gas storage conditions, 2023. URL https://doi.org/10.25625/YVCV2Y.

[74] S. Hogeweg, B. Hagemann, and L. Ganzer. Numerical Simulation of Bio-Geo-Reactive Transport during UHS - A Modelling Approach. In *DGMK/ÖGEW Frühjahrstagung 2023*, 2023-05-31/2023-06-01.

[75] S. Hogeweg, B. Hagemann, V. Bobrov, and L. Ganzer. Development and calibration of a bio-geo-reactive transport model for UHS. *Frontiers in Energy Research*, 12:1385273, May 2024. ISSN 2296-598X. doi:10.3389/fenrg.2024.1385273.

[76] J. Hommel. *Modelling Biogeochemical and Mass Transport Processes in the Subsurface: Investigation of Microbially Induced Calcite Precipitation*. PhD thesis, Universität Stuttgart, 2016. URL http://elib.uni-stuttgart.de/handle/11682/8787.

[77] Isodetect GmbH, MicroPro GmbH, and DBI Gas- und Umwelttechnik GmbH. Bio-UGS – Biological conversion of carbon dioxide and hydrogen to methane, May 2020. URL https://co2-utilization.net/fileadmin/user_upload/PRO_CO2-Win_BioUGS_EN.pdf. (accessed 18.12.2023).

[78] D. L. Katz and R. L. Lee. *Natural Gas Engineering: Production and Storage*. McGraw-Hill, New York, 1990. ISBN 978-0-07-100777-1.

[79] N. Khoshnevis, S. Hogeweg, C. Goncalves Machado, and B. Hagemann. Numerical Modeling of Bio-Reactive Transport During Underground Hydrogen Storage – a Benchmark Study. In *The Fourth EAGE Global Energy Transition Conference and Exhibition*, pages 1–5, Paris, France, Nov. 2023. European Association of Geoscientists & Engineers. doi:10.3997/2214-4609.202321087.

[80] P. Knabner and L. Angermann. *Numerik partieller Differentialgleichungen.* Springer Berlin Heidelberg, Berlin, Heidelberg, 2000. ISBN 978-3-540-66231-0 978-3-642-57181-7. doi:10.1007/978-3-642-57181-7.

[81] H. Kobus and U. de Haar, editors. *Perspektiven der Wasserforschung: Ergebnisse aus der 50. Sitzung der Kommission am 10. und 11. März 1994.* Number 14 in Mitteilung ... der Senatskommission für Wasserforschung / Deutsche Forschungsgemeinschaft, DFG. VCH, Weinheim, 1996. ISBN 978-3-527-27573-1.

[82] T. Koch, D. Gläser, K. Weishaupt, S. Ackermann, M. Beck, B. Becker, S. Burbulla, H. Class, E. Coltman, S. Emmert, T. Fetzer, C. Grüninger, K. Heck, J. Hommel, T. Kurz, M. Lipp, F. Mohammadi, S. Scherrer, M. Schneider, G. Seitz, L. Stadler, M. Utz, F. Weinhardt, and B. Flemisch. DuMu^x 3 – An Open-Source Simulator for Solving Flow and Transport Problems in Porous Media with a Focus on Model Coupling. *Computers & Mathematics with Applications*, 2020. ISSN 08981221. doi:10.1016/j.camwa.2020.02.012.

[83] J. Kozeny. *Über kapillare Leitung des Wassers im Boden: (Aufstieg, Versickerung u. Anwendung auf die Bewässerung).* Hölder-Pichler-Tempsky, A.-G., Akad. d. Wiss., 1927.

[84] A. C. Lasaga, J. M. Soler, J. Ganor, T. E. Burch, and K. L. Nagy. Chemical weathering rate laws and global geochemical cycles. *Geochimica et Cosmochimica Acta*, 58(10):2361–2386, May 1994. ISSN 00167037. doi:10.1016/0016-7037(94)90016-7.

[85] LBEG. Untertage Gasspeicherung in Deutschland. *Erdöl Erdgas Kohle (EEK)*, 138(11), 2022.

[86] Lehrstuhl für Hydromechanik und Hydrosystemmodellierung, Universität Stuttgart. DuMu^x Handbook, Jan. 2023. URL https://dumux.org/docs/handbook/master/dumux-handbook.pdf.

[87] W. Leonhard, U. Buenger, F. Crotogino, Ch. Gatzen, W. Glaunsinger, S. Huebner, M. Kleimaier, M. Koenemund, H. Landinger, T. Lebioda, D. U. Sauer, H. Weber, A. Wenzel, E. Wolf, W. Woyke, and S. Zunft. Energiespeicher in Stromversorgungssystemen mit hohem Anteil erneuerbarer Energieträger - Bedeutung, Stand der Technik, Handlungsbedarf. Technical report, Verband der Elektrotechnik, Elektronik, Informationstechnik e.V., Frankfurt am Main, Dec. 2008.

[88] R. J. LeVeque. *Finite Volume Methods for Hyperbolic Problems*. Cambridge Texts in Applied Mathematics. Cambridge University Press, Cambridge, 2002. ISBN 978-0-521-81087-6 978-0-521-00924-9.

[89] Z. Li, X. Wang, A. Alberdi, J. Deng, Z. Zhong, H. Si, C. Zheng, H. Zhou, J. Wang, Y. Yang, A.-D. G. Wright, S. Mao, Z. Zhang, L. Guan, and G. Li. Comparative Microbiome Analysis Reveals the Ecological Relationships Between Rumen Methanogens, Acetogens, and Their Hosts. *Frontiers in Microbiology*, 11:1311, June 2020. ISSN 1664-302X. doi:10.3389/fmicb.2020.01311.

[90] Chas. B. Lipman. Living Microörganisms in Ancient Rocks. *Journal of Bacteriology*, 22(3):183–198, Sept. 1931. ISSN 0021-9193, 1098-5530. doi:10.1128/jb.22.3.183-198.1931.

[91] J. Lohrenz, B. G. Bray, and C. R. Clark. Calculating Viscosities of Reservoir Fluids From Their Compositions. *Journal of Petroleum Technology*, 16(10):1171–1176, Oct. 1964. ISSN 0149-2136, 1944-978X. doi:10.2118/915-PA.

[92] M. Lysyy, M. A. Fernø, and G. Ersland. Effect of relative permeability hysteresis on reservoir simulation of underground hydrogen storage in an offshore aquifer. *Journal of Energy Storage*, 64:107229, Aug. 2023. ISSN 2352152X. doi:10.1016/j.est.2023.107229.

[93] M. T. Madigan, K. S. Bender, D. H. Buckley, W. M. Sattley, D. A. Stahl, and T. D. Brock. *Brock Biology of Microorganisms*. Pearson, NY, NY, 15th edition, 2019. ISBN 978-1-292-23510-3.

[94] E. Mahdinia, S. Liu, A. Demirci, and V. M. Puri. Microbial Growth Models. In A. Demirci, H. Feng, and K. Krishnamurthy, editors, *Food Safety Engineering*, pages 357–398. Springer International Publishing, Cham, 2020. ISBN 978-3-030-42659-0 978-3-030-42660-6. doi:10.1007/978-3-030-42660-6_14.

[95] J. Michelsen, E. M. Thaysen, S. Hogeweg, B. Hagemann, A. Hassanpouryouzband, N. Langanke, K. Edlmann, and L. Ganzer. Data for: HyUSPRe - Work Package 4 - Hydrogen reservoir flow behaviour: Measurements of molecular diffusion, mechanical dispersion and relative permeability, 2023. URL https://doi.org/10.25625/7XCCL8.

[96] J. Michelsen, E. M. Thaysen, S. Hogeweg, B. Hagemann, A. Hassanpouryouzband, N. Langanke, K. Edlmann, and L. Ganzer. Hydrogen reservoir flow behaviour: Measurements of molecular diffusion, mechanical dispersion and relative permeability. H2020 HyUSPRe Project Report D4.4, Clausthal University of Technology, Apr. 2023. URL https://www.hyuspre.eu/wp-content/uploads/2023/04/HyUSPRe_D4.4_Methodology-and-results-of-H2-reservoir-flow-behavior-experiments_2023.03.31.pdf.

[97] J. Michelsen, S. Hogeweg, B. Hagemann, N. Langanke, and L. Ganzer. Experimental investigations and development of a correlation to characterize the diffusion process of hydrogen and methane during UHS. In *Experimental Investigations and Development of a Correlation to Characterize the Diffusion Process of Hydrogen and Methane during UHS*, Celle, Germany, 2023-05-31/2023-06-01.

[98] J. Michelsen, N. Langanke, B. Hagemann, S. Hogeweg, and L. Ganzer. Diffusion measurements with hydrogen and methane through reservoir rock samples. In *Advanced SCAL for Carbon Storage & CO2 Utilization*, Abu Dhabi, 2023-10-09/2023-10-13.

[99] R. J. Millington and J. P. Quirk. Permeability of porous solids. *Transactions of the Faraday Society*, 57:1200, 1961. ISSN 0014-7672. doi:10.1039/tf9615701200.

[100] J. Miocic, N. Heinemann, K. Edlmann, J. Scafidi, F. Molaei, and J. Alcalde. Underground hydrogen storage: A review. *Geological Society, London, Special Publications*, 528(1):SP528–2022–88, July 2023. ISSN 0305-8719, 2041-4927. doi:10.1144/SP528-2022-88.

[101] N. Moeininia, B. Kessler, H. Bültemeier, M. Henel, A. Bilsing, S. Schmidt, S. Hogeweg, B. Hagemann, L. Ganzer, M. Wagner, J. Launer, S. Haas, E. Dunkelberg, J. Bergmann, J. Katner, N. Ouanes, B. Hirschl, S. Salecki, H. Staisch, C. Berg, and U. Löwe. UMAS -

Untertägige Methanisierung im Aqiferspeicher; Teilprojekte (TP): TP1 Anlagenevaluierung und Simulation; TP2 Geologische Untersuchungen; TP3 Mikrobiologische Untersuchungen; TP4 Energiesystemmodellierung; TP5 Ökonomische und ökologische Bewertung; TP 6 Genehmigungsplanung: Abschlussbericht UMAS: Laufzeit: 01.05.2020-30.3.2022 BES, TUC; 01.05.2020-31.05.2022 DBI, IÖW, RLI, MP. Technical report, Berliner Erdgasspeicher GmbH, 2022. URL https://www.tib.eu/de/suchen/id/TIBKAT%3A1831042800.

[102] J. Monod. The growth of bacterial cultures. *Annual Review of Microbiology*, 3(1):371–394, 1949. doi:10.1146/annurev.mi.03.100149.002103.

[103] A. Moser. *Bioprocess Technology*. Springer New York, New York, NY, 1988. ISBN 978-1-4613-8750-3 978-1-4613-8748-0. doi:10.1007/978-1-4613-8748-0.

[104] Nederlandse Organisatie voor toegepast-natuurwetenschappelijk onderzoek (TNO), Technische Universität Clausthal, University of Edinburgh, Energieinstitut an der Johannes Kepler Universität Linz, Fondazione Bruno Kessler, Wageningen University, and Forschungszentrum Jülich GmbH. Hydrogen Underground storage in Porous Reservoirs - HyUSPRe, 2024. URL https://doi.org/10.3030/101006632. (accessed 18.12.2023).

[105] V. Nikolaevskii. Convective diffusion in porous media. *Journal of Applied Mathematics and Mechanics*, 23(6):1492–1503, Jan. 1959. ISSN 00218928. doi:10.1016/0021-8928(59)90006-1.

[106] B. Ollivier, M.-L. Fardeau, J.-L. Cayol, M. Magot, B. K. C. Patel, G. Prensier, and J.-L. Garcia. Methanocalculus halotolerans gen. nov., sp. nov., isolated from an oil-producing well. *International Journal of Systematic and Evolutionary Microbiology*, 48(3):821–828, 1998. ISSN 1466-5034. doi:10.1099/00207713-48-3-821.

[107] C. Ostertag-Henning. Geochemical reactions of iron oxides with hydrogen in the porespace of sandstones: Processes, kinetics & limitations of the extent of reaction. In *Interpore 2023 - Book of Abstracts*, Edinburgh, 2023.

[108] C. L. Palagi and K. Aziz. Modeling Vertical and Horizontal Wells With Voronoi Grid. *SPE Reservoir Engineering*, 9(01):15–21, Feb. 1994. ISSN 0885-9248, 2469-9683. doi:10.2118/24072-PA.

[109] G. Pandey, M. Tek, and L. Katz Donald. Diffusion of fluids through porous media with implications in petroleum geology. *American Association of Petroleum Geologists Bulletin*, 58(2):291–303, 1974. ISSN 0002-7464. doi:10.1306/83d913da-16c7-11d7-8645000102c1865d.

[110] M. Panfilov. Underground Storage of Hydrogen: In Situ Self-Organisation and Methane Generation. *Transport in Porous Media*, 85(3):841–865, 2010. ISSN 1573-1634. doi:10.1007/s11242-010-9595-7.

[111] C. Park and E. Marchand. Modelling salinity inhibition effects during biodegradation of perchlorate. *Journal of Applied Microbiology*, 101(1): 222–233, July 2006. ISSN 1364-5072, 1365-2672. doi:10.1111/j.1365-2672.2006.02950.x.

[112] N. Parker, M. Schneegurt, A.-H. Thi Tu, B. M. Forster, and P. Lister. *Microbiology*. Open Textbook Library. OpenStax, Houston, Texas, 2016. ISBN 978-1-938168-14-7.

[113] L. Paterson. The implications of fingering in underground hydrogen storage. *International Journal of Hydrogen Energy*, 8(1):53–59, 1983. ISSN 03603199. doi:10.1016/0360-3199(83)90035-6.

[114] D. W. Peaceman. Interpretation of Well-Block Pressures in Numerical Reservoir Simulation(includes associated paper 6988). *Society of Petroleum Engineers Journal*, 18(03):183–194, 1978. ISSN 0197-7520. doi:10.2118/6893-PA.

[115] D. W. Peaceman. Interpretation of Well-Block Pressures in Numerical Reservoir Simulation With Nonsquare Grid Blocks and Anisotropic Permeability. *Society of Petroleum Engineers Journal*, 23(03):531–543, June 1983. ISSN 0197-7520. doi:10.2118/10528-PA.

[116] D.-Y. Peng and D. B. Robinson. A New Two-Constant Equation of State. *Industrial & Engineering Chemistry Fundamentals*, 15(1):59–64, Feb. 1976. ISSN 0196-4313, 1541-4833. doi:10.1021/i160057a011.

[117] A. Perez, E. Pérez, S. Dupraz, and J. Bolcich. Patagonia wind - hydrogen project: Underground storage and methanation. In *21st World Hydrogen Energy Conference 2016*, Zaragoza, Spain, June 2016. URL https://brgm.hal.science/hal-01317467.

[118] T. Perkins and O. Johnston. A Review of Diffusion and Dispersion in Porous Media. *Society of Petroleum Engineers Journal*, 3(01):70–84, Mar. 1963. ISSN 0197-7520. doi:10.2118/480-PA.

[119] F. J. Pettijohn, P. E. Potter, and R. Siever. *Mineral and Chemical Composition*, pages 25–67. Springer US, New York, NY, 1972. ISBN 978-0-387-90071-1 978-1-4615-9974-6. doi:10.1007/978-1-4615-9974-6_2.

[120] B. E. Poling, J. M. Prausnitz, and J. P. O'Connell. *The Properties of Gases and Liquids*. McGraw-Hill, New York, 5th edition, 2001. ISBN 978-0-07-011682-5.

[121] D. K. Ponting. Corner Point Geometry in Reservoir Simulation. In *ECMOR I - 1st European Conference on the Mathematics of Oil Recovery*, Cambridge, UK, 1989. European Association of Geoscientists & Engineers. ISBN 978-94-6282-134-7. doi:10.3997/2214-4609.201411305.

[122] D. Pudlo, S. Henkel, and R. Gaupp. Verbundvorhaben H2STORE, Teilprojekt 3: Sedimentologisch-fazielle und mineralogisch-geochemische Untersuchungen an Reservoir- und Deckgesteinen: Abschlussbericht zum Verbundvorhaben H2STORE Teilprojekt 3: Berichtszeitraum: 01.08.2012-31.12.2015. Technical report, Friedrich-Schiller-Universität Jena, Institut für Geowissenschaften, Lehrstuhl für Allgemeine und Historische Geologie, 2016.

[123] S. A. Rackley. Geochemical and biogeochemical features, events, and processes. In *Carbon Capture and Storage*, pages 365–386. Elsevier, 2017. ISBN 978-0-12-812041-5. doi:10.1016/B978-0-12-812041-5.00014-3.

[124] RAG Austria AG. Endbericht: Underground Sun Conversion. Technical report, RAG Austria AG, 2021. URL https://www.underground-sun-conversion.at/presse/publikationen/publikationen-1.html.

[125] RAG Austria AG. Underground Sun Storage: World's first geological hydrogen storage facility goes into operation, Apr. 2023. URL https://www.uss-2030.at/en/public-relations-/-publications/press/details/article/underground-sun-storage-worlds-first-geological-hydrogen-storage-facility-goes-into-operation.html. (accessed 26.09.2023).

[126] RAG Austria AG, AXIOM angewandte Prozesstechnik GesmbH, Verbund AG, Montanuniversität Leoben, Universität für Bodenkultur Wien, and Energieinstitut an der Johannes Kepler Universität Linz. Underground Sun Storage: Publizierbarer Endbericht. Technical report, RAG Austria AG, Wien, 31.11.2017. URL https://www.underground-sun-storage.at/fileadmin/bilder/SUNSTORAGE/Publikationen/UndergroundSunStorage_Publizierbarer_Endbericht_3.1_web.pdf.

[127] B. E. Rittmann and P. L. McCarty. *Environmental Biotechnology: Principles and Applications*. McGraw-Hill, New York, 2nd edition, 2020. ISBN 978-1-260-44161-1.

[128] P. G. Saffman and G. I. Taylor. The penetration of a fluid into a porous medium or Hele-Shaw cell containing a more viscous liquid. *Proceedings of the Royal Society of London. Series A. Mathematical and Physical Sciences*, 245(1242):312–329, June 1958. ISSN 0080-4630, 2053-9169. doi:10.1098/rspa.1958.0085.

[129] O. Sander. *DUNE – the Distributed and Unified Numerics Environment*. Springer Nature, S.l., 2021. ISBN 978-3-030-59704-7. URL https://link.springer.com/book/10.1007/978-3-030-59702-3.

[130] A. E. Scheidegger. General Theory of Dispersion in Porous Media. *Journal of Geophysical Research*, 66(10):3273–3278, 1961. ISSN 01480227. doi:10.1029/JZ066i010p03273.

[131] K. Schwabe and J. Brand. Prediction of Reservoir Behavior Using Numerical Simulators. In *All Days*, pages SPE–1857–MS, New Orleans, Louisiana, Oct. 1967. SPE. doi:10.2118/1857-MS.

[132] M. Siegert, D. Cichocka, S. Herrmann, F. Gründger, S. Feisthauer, H.-H. Richnow, D. Springael, and M. Krüger. Accelerated methanogenesis from aliphatic and aromatic hydrocarbons under iron- and sulfate-reducing conditions: Methanogenic hydrocarbon degradation. *FEMS Microbiology Letters*, 315(1):6–16, Feb. 2011. ISSN 03781097. doi:10.1111/j.1574-6968.2010.02165.x.

[133] P. Šmigáň, J. Greksák, J. Kozánková, F. Buzek, V. Onderka, and I. Wolf. Methanogenic bacteria as a key factor involved in changes of town gas stored in an underground reservoir. *FEMS Microbiology Letters*, 73(3):221–224, 1990. ISSN 03781097. doi:10.1016/0378-1097(90)90733-7.

[134] L. I. Stiel and G. Thodos. The viscosity of nonpolar gases at normal pressures. *AIChE Journal*, 7(4):611–615, Dec. 1961. ISSN 0001-1541, 1547-5905. doi:10.1002/aic.690070416.

[135] G. Stotzky and A. G. Norman. Factors limiting microbial activities in soil: I. The level of substrate, nitrogen, and phosphorus. *Archiv für Mikrobiologie*, 40(4):341–369, 1961. ISSN 0302-8933, 1432-072X. doi:10.1007/BF00422050.

[136] G. Strobel, B. Hagemann, and L. Ganzer. History Matching of Bioreactive Transport in an Underground Hydrogen Storage Field Case. In *EAGE/DGMK Joint Workshop on Underground Storage of Hydrogen*, pages 1–3, Celle, Germany, 2019. European Association of Geoscientists & Engineers. doi:10.3997/2214-4609.201900258.

[137] G. Strobel, B. Hagemann, T. M. Huppertz, and L. Ganzer. Underground bio-methanation: Concept and potential. *Renewable and Sustainable Energy Reviews*, 123:109747, May 2020. ISSN 13640321. doi:10.1016/j.rser.2020.109747.

[138] G. Strobel, B. Hagemann, M. Wirth, and L. Ganzer. Pore-Scale Modeling of Microbial Growth in A Two-Phase Saturated Porous Medium. In *ECMOR XVII - 17th European Conference on the Mathematics of Oil Recovery*, volume 2020, pages 1–14. European Association of Geoscientists & Engineers, 2020. ISBN 2214-4609. doi:10.3997/2214-4609.202035171.

[139] G. Strobel, M. Wirth, and B. Hagemann. Microorganism Database, 2022. URL https://www.ite.tu-clausthal.de/en/research/subsurface-energy-and-gas-storage/mikroorganism-database.

[140] G. Strobel, B. Hagemann, C. T. Lüddeke, and L. Ganzer. Coupled model for microbial growth and phase mass transfer in pressurized batch reactors in the context of underground hydrogen storage. *Frontiers in Microbiology*, 14:1150102, Apr. 2023. ISSN 1664-302X. doi:10.3389/fmicb.2023.1150102.

[141] G. Strobel, C. Kosack, P. Bombach, A. Fischer, B. Hagemann, and S. Hogeweg. HySTORAGE: Preliminary investigations of possible hydrogen losses with focus on a planned hydrogen storage field test in

Bierwang. In *DGMK/ÖGEW Frühjahrstagung 2023*, Celle, Germany, May 2023.

[142] G. Strobel, J. Zawallich, B. Hagemann, L. Ganzer, and O. Ippisch. Experimental and numerical investigation of microbial growth in two-phase saturated porous media at the pore-scale. *Sustainable Energy & Fuels*, 7(16):3939–3948, 2023. ISSN 2398-4902. doi:10.1039/D3SE00037K.

[143] R. Tarkowski. Underground hydrogen storage: Characteristics and prospects. *Renewable and Sustainable Energy Reviews*, 105:86–94, 2019. ISSN 13640321. doi:10.1016/j.rser.2019.01.051.

[144] M. Tek. *Natural Gas Underground Storage: Inventory and Deliverability*. PennWell Books. PennWell Pub., 1996. ISBN 978-0-87814-614-7.

[145] M. R. Tek. *Underground Storage of Natural Gas*, volume 171 of *NATO ASI Series, Series E: Applied Sciences, 0168-132X*. Springer Netherlands, Dordrecht, 1989. ISBN 978-94-010-6936-6. doi:10.1007/978-94-009-0993-9.

[146] E. M. Thaysen and G. Strobel. Dataset on the environmental growth conditions of methanogens, homoacetogens and sulfate reducers, May 2021.

[147] E. M. Thaysen, S. McMahon, G. Strobel, I. B. Butler, B. T. Ngwenya, N. Heinemann, M. Wilkinson, A. Hassanpouryouzband, C. I. McDermott, and K. Edlmann. Estimating microbial growth and hydrogen consumption in hydrogen storage in porous media. *Renewable and Sustainable Energy Reviews*, 151:111481, 2021. ISSN 13640321. doi:10.1016/j.rser.2021.111481.

[148] E. M. Thaysen, T. Armitage, L. Slabon, A. Hassanpouryouzband, and K. Edlmann. Microbial risk assessment for underground hydrogen storage in porous rocks. *Fuel*, 352:128852, Nov. 2023. ISSN 00162361. doi:10.1016/j.fuel.2023.128852.

[149] M. Thema, F. Bauer, and M. Sterner. Power-to-Gas: Electrolysis and methanation status review. *Renewable and Sustainable Energy Reviews*, 112:775–787, Sept. 2019. ISSN 1364-0321. doi:10.1016/j.rser.2019.06.030.

[150] L. Truche, G. Berger, C. Destrigneville, D. Guillaume, and E. Giffaut. Kinetics of pyrite to pyrrhotite reduction by hydrogen in calcite buffered solutions between 90 and 180°C: Implications for nuclear waste disposal. *Geochimica et Cosmochimica Acta*, 74(10):2894–2914, 2010. ISSN 0016-7037. doi:10.1016/j.gca.2010.02.027.

[151] L. Truche, M.-C. Jodin-Caumon, C. Lerouge, G. Berger, R. Mosser-Ruck, E. Giffaut, and N. Michau. Sulphide mineral reactions in clay-rich rock induced by high hydrogen pressure. Application to disturbed or natural settings up to 250°C and 30bar. *Chemical Geology*, 351: 217–228, 2013. doi:10.1016/j.chemgeo.2013.05.025.

[152] M. Th. Van Genuchten. A Closed-form Equation for Predicting the Hydraulic Conductivity of Unsaturated Soils. *Soil Science Society of America Journal*, 44(5):892–898, Sept. 1980. ISSN 0361-5995, 1435-0661. doi:10.2136/sssaj1980.03615995004400050002x.

[153] S. van Gessel and H. Hajibeygi. Underground Hydrogen Storage: Technology Monitor Report. Technical report, Hydrogen TCP-Task 42, 2023.

[154] R. van Rossum, J. Jens, G. La Guardia, A. Wang, L. Kühnen, and M. Overgaag. European Hydrogen Backbone - A European hydrogen infrastructure vision covering 28 countries. Technical report, ehb, Apr. 2022. URL https://ehb.eu/files/downloads/ehb-report-220428-17h00-interactive-1.pdf.

[155] L. Vermeersch, G. Perez-Samper, B. Cerulus, A. Jariani, B. Gallone, K. Voordeckers, J. Steensels, and K. J. Verstrepen. On the duration of the microbial lag phase. *Current Genetics*, 65(3):721–727, June 2019. ISSN 0172-8083, 1432-0983. doi:10.1007/s00294-019-00938-2.

[156] M. Von Smoluchowski. Zur kinetischen Theorie der Brownschen Molekularbewegung und der Suspensionen. *Annalen der Physik*, 326(14):756–780, 1906. ISSN 00033804, 15213889. doi:10.1002/andp.19063261405.

[157] G. Wang, G. Pickup, K. Sorbie, J. De Rezende, F. Zarei, and E. Mackay. Bioreaction coupled flow simulations: Impacts of methanogenesis on seasonal underground hydrogen storage. *International Journal of Hydrogen Energy*, page S036031992305718X, Nov. 2023. ISSN 03603199. doi:10.1016/j.ijhydene.2023.11.035.

[158] E. Wicke and R. Kallenbach. Die Oberflächendiffusion von Kohlendioxyd in aktiven Kohlen. *Kolloid-Zeitschrift*, 97(2):135–151, 1941. ISSN 1435-1536. doi:10.1007/BF01502640.

[159] C. R. Wilke and C. Y. Lee. Estimation of Diffusion Coefficients for Gases and Vapors. *Industrial & Engineering Chemistry*, 47(6):1253–1257, June 1955. ISSN 0019-7866, 1541-5724. doi:10.1021/ie50546a056.

[160] O. C. Zienkiewicz, R. L. Taylor, and J. Z. Zhu. *The Finite Element Method: Its Basis and Fundamentals*. Elsevier/Butterworth-Heinemann, Burlington (Mass.), 6th edition, 2005. ISBN 978-0-7506-6320-5.